Low Mach Number Simulations of Convective Boundary Mixing in Classical Novae

Dissertation zur Erlangung
des naturwissenschaftlichen Doktorgrades
der Julius-Maximilians-Universität Würzburg

vorgelegt von

Alejandro Bolaños-Rosales
aus Puebla, México

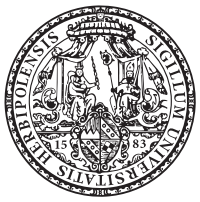

Würzburg
2016

Eingereicht am Donnerstag, den 28. April 2016
bei der Fakultät für Physik und Astronomie

1. Gutachter:	Prof. Dr. Friedrich Röpke
2. Gutachter:	Prof. Dr. Matthias Kadler
der Dissertation.	
Vorsitzende(r):	Prof. Dr. Ansgar Denner
1. Prüfer:	Prof. Dr. Friedrich Röpke
2. Prüfer:	Prof. Dr. Matthias Kadler
3. Prüfer:	Prof. Dr. Raimund Ströhmer
Tag des Promotionskolloquiums:	Freitag, den 29. Juli 2016
Doktorurkunde ausgehändigt am:	Donnerstag, den 11. August 2016

Low Mach Number Simulations of Convective Boundary Mixing in Classical Novae

Dissertation zur Erlangung
des naturwissenschaftlichen Doktorgrades
der Julius-Maximilians-Universität Würzburg

vorgelegt von

Alejandro Bolaños-Rosales
aus Puebla, México

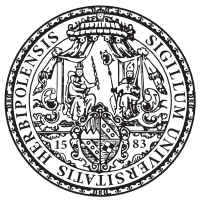

Würzburg
2016

The page format is $P = 1 : \sqrt{2}$ (DIN A4). The textblock proportions $T = 1 : 1.62$ (golden ratio). The text is set in *Latin Modern*, with a size of 11pt, and leading of 15pt.
I drew inspiration from *The Elements of Typographic Style* by Robert Bringhurst,
Printed in acid-free paper in Würzburg, Germany, August 2016.

Para mi familia.

Acknowledgments

Thanks to Prof. Friedrich Röpke and Prof. Christian Klingenberg for inviting me to do a PhD and teaching me the tools to do so, and for all the interesting evenings they organized in their homes with the group.

Special thanks to Philipp Edelmann for his continuous help and supervision, in matters both astrophysical and computational, for his proofreading and his seemingly never-ending patience, without which this work would have been impossible. Thanks also to his lovely wife Christina, who once inadvertently gave a me huge morale boost.

A big thanks also to all friends and colleagues from the Astronomy department and the Röpke and Klingenberg groups in particular. Thanks also to Rosamunde Pare, Verena Rückert and Aron Michel for proofreading some passages.

Grazie mille ai miei carissimi amici Juan Pablo Gallego "Quinto", Gabrielle "Oracolo" Ciaramella, Gero "Bello" Schnücke e Stephanie Perlia con cui ho condiviso tante risate in mensa, e nelle pause caffè e gelato, e senza i quali non sarei soppravissuto a questo periodo.

Por último – no por importancia, sino puramente por norma – agradezco a mi familia, a quien este trabajo está dedicado. A mi abuelito José Luis, quien siempre me apoyó y me educó para la vida. A mi Abuelita Seve, quien me llama por teléfono cuando yo no llamo y me recuerda del cariño que nos tiene a todos. A mi Tío Güicho por el apoyo moral y su curiosidad sobre astronomía. Gracias a mi Papá Humberto y mi Mamá Mare, quienes me apoyaron siempre. Gracias a mi Andreas por las llamadas llenas de carcajadas. Y por supuesto a mi hermano Aramis, quien también me acompañó en las fases laboriosas de la Diplomarbeit y de esta tesis, y con quien he pasado momentos muy divertidos en esta fase de mi vida, tan lejos del resto de mi familia. A todos, muchísimas gracias por confiar en mí.

Zusammenfassung

Klassische Novae sind thermonukleare Explosionen an der Oberfläche von Weißen Zwergen. Wenn ein solcher sich in einem Doppelsternsystem zusammen mit einem Hauptreihenstern oder einem späteren Stern befindet, kann Akkretion vom Begleiter zum Weißen Zwerg stattfinden, falls der Begleitstern seine Roche-Grenze überschreitet. Die wasserstoffreiche Hülle, die sich auf der Oberfläche des Sterns bildet, zündet aufgrund des enormen Gravitationsdrucks in einer Deflagration. Aufgrund der Entartung des Gases führt das nukleare Brennen zu einem thermonuklearen Durchgehen (engl. *runaway*) und schließlich zu einer Explosion mit Energien in der Größenordnung von 10^{46} erg. Der Weiße Zwerg bleibt dabei unberührt. Spektralanalysen der ausgestoßenen Gase deuten auf Isotope hin, die am heißen CNO-Zyklus beteiligt sind. Dies legt nahe, dass vor oder während der Brennphase eine Durchmischung von Materie zwischen der akkretierten Hülle und dem Weißen Zwerg stattfinden muss.

Die Konvektion und nukleares Brennen entwickeln sich im Strömungsbereich kleiner Machzahlen. Wir benutzten den Seven League Hydro code (*SLH*), welcher über numerische Verfahren verfügt, die auf einen weiten Bereich von Machzahlen anwendbar sind. Daraus errechneten wir Simulationen von Klassischen Novae in zwei und drei Dimensionen. Basierend auf einem sphärisch-symmetrischen Modell, das wir mit einem Sternentwicklungscode erstellten, entwickelten wir ein eigenes Nova-Modell. Wir testeten dies in Kombination mit eienr Reihe von Gittern und Randbedingungen. Anschließend analysierten wir im Detail das Verhalten von Temperatur, Dichte und nuklearer Energieerzeugungsrate in den Schichten zwischen Weißem Zwerg und Wasserstoffhülle, wo die Kernfusion hauptsächlich stattfindet, um die Struktur der Brennzone und deren Einfluss auf die Nukleosynthese zu verstehen. Wir analysierten die Effizienz der Konvektion, welche Elemente aus dem Weißen Zwerg nach oben in die Hülle transportiert. Die Ergebnisse entsprechen denen der Literatur, dennoch hängen sie stark von der numerischen Auflösung ab. Wir untersuchten die Isotopenhäufigkeit der im CNO-Zyklus beteiligten Elemente, und schloßen hieraus, dass das Brennen durch den weniger energetischen "kalten" CNO-Zyklus verläuft. Dies kann darauf zurückgeführt werden, dass unter den Bedingungen, die die Mehrzahl der multidimensionalen Modelle aus der Fachliteratur mit sich bringen, die Wasserstoffhülle tatsächlich nicht entartet ist. Abschließend simulierten wir testweise 3D-Modelle, aber neue Randbedingungen sind nötig, um mit den Berechnungen fortfahren zu können.

Abstract

Classical novae are thermonuclear explosions occurring on the surface of white dwarfs. When co-existing in a binary system with a main sequence or more evolved star, mass accretion from the companion star to the white dwarf can take place if the companion overflows its Roche lobe. The envelope of hydrogen-rich matter which builds on top of the white dwarf eventually ignites under degenerate conditions, leading to a thermonuclear runaway and an explosion in the order of 10^{46} erg, while leaving the white dwarf intact. Spectral analyses from the debris indicate an abundance of isotopes that are tracers of nuclear burning via the hot CNO cycle, which in turn reveal some sort of mixing between the envelope and the white dwarf underneath. The exact mechanism is still a matter of debate.

The convection and nuclear burning in novae develop in the low Mach number regime. We used the Seven League Hydro code (*SLH*), which employs numerical schemes designed to correctly simulate low Mach number flows, to perform two and three-dimensional simulations of classical novae. Based on a spherically-symmetric model created with aid of a stellar evolution code, we developed our own nova model and tested it on a variety of numerical grids and boundary conditions for validation. We focused on the evolution of temperature, density and nuclear energy generation rate at the layers between white dwarf and envelope, where most of the energy is generated, to understand the structure of the transition region, and its effect on the nuclear burning. We analyzed the resulting dredge-up efficiency stemming from the convective motions in the envelope. Our models yield similar results to the literature, but seem to depend very strongly on the numerical resolution. We followed the evolution of the nuclear species involved in the CNO cycle and concluded that the thermonuclear reactions primarily taking place are those of the cold and not the hot CNO cycle. The reason behind this could be that under the conditions generally assumed for multi-dimensional simulations, the envelope is in fact not degenerate. We performed initial tests for 3D simulations and realized that alternative boundary conditions are needed.

Contents

1 Old and New Stars **1**
- 1.1 Classical novae: the basic picture 4
  - 1.1.1 Astronomical properties 4
  - 1.1.2 The thermonuclear runaway model 6
- 1.2 Numerical simulations of classical novae 7
  - 1.2.1 Defining timescales 8
  - 1.2.2 Previous work 9
  - 1.2.3 Three-dimensional stellar evolution 15
- 1.3 Outline & goal of this work 17

2 Astrophysical Background **19**
- 2.1 Stellar structure and evolution 19
  - 2.1.1 Basic equations 19
  - 2.1.2 Convection and dynamical stability 21
  - 2.1.3 Mixing-length theory 23
- 2.2 Thermonuclear astrophysics 25
  - 2.2.1 Nuclear physics 26
  - 2.2.2 The *pp* and *pep* chains 28
  - 2.2.3 The cold and hot CNO cycles 29
- 2.3 Nuclear reaction networks 32

3 Description of the code **35**
- 3.1 Multidimensional hydrodynamic simulations 35
  - 3.1.1 Euler equations 35
  - 3.1.2 Finite-volume schemes 39
  - 3.1.3 Time-stepping 41
  - 3.1.4 Boundary conditions 45
  - 3.1.5 Coordinate systems and frames of reference 46
- 3.2 Low Mach number hydrodynamics 47
  - 3.2.1 Scaling of the fluid equations with low Mach numbers 47
  - 3.2.2 Flux preconditioning 49
  - 3.2.3 AUSM$^+$-up 51
- 3.3 Well-balancing 52
  - 3.3.1 Checkerboard instability 52
  - 3.3.2 The Cargo–Le Roux method 53

4 Engineering a nova model **57**
4.1 The Kercek Model 58
4.2 The Würzburg Model 59
4.2.1 Treatment of the isotopic mass fractions 59
4.2.2 Hydrostatic equilibrium 59
4.3 The spatial grid 63
4.3.1 Improved integration of hydrostatic equilibrium 70
4.4 The core-envelope transition 71
4.5 A model from a stellar evolution code 78
4.6 Validation tests 79
4.6.1 `alpha`: proof of concept 79
4.6.2 `bravo`: test of perturbations 80
4.6.3 Box width 82

5 Results **87**
5.1 Morphology of the convective flow 87
5.2 Nuclear reactions 92

6 Conclusions & Outlook **101**

A Additional figures **105**

1. Old and New Stars

The oldest known historical literal reference to a "new star" dates back to 75 AD, by Pliny the Elder[1]. In his *Naturae Historia* [Plinius 1855] he wrote about the Greek astronomer, mathematician and geographer Hipparchus discovering a *stella nova* in the sky. Novae reveal themselves as bright light sources that shine where there was apparently no star before, and fade over the course of weeks. One can assume from Hipparchus's account that he was describing a comet and not a star. However, the origins of novae in general (those called *super*novae, *classical* novae and those that reappear, *recurrent* novae) are still debated, and the debate is certainly not a recent one. Already in the 17th century, in the *Almagestum Novum*, thirteen different theories are quoted in Riccioli [1652], which appear quite outlandish to the modern reader. Newton proposed a mechanism that resembles noticeably our modern explanation (Newton [1726], English translation Newton [1729]):

> *So fixed stars, that have been gradually wasted by the light and vapors emitted from them for a long time, may be recruited by comets that fall upon them; and from this fresh supply of new fuel those old stars, acquiring new splendor, may pass for new stars.*

Later theories tried to explain these bursts of light as collisions of comets or friction with clouds. But Newton had already deciphered two key aspects. First, that the "new" stars could be instead aging dim stars; and second, that the sudden rise in brightness could come from supply of new fuel.

We now know that comets are not the source of energy for novae. Instead, they arise from the complex interactions of pairs of stars that orbit each other in a close orbit of about the size of the Earth-Moon system. These close binary systems are composed of a white dwarf (an evolved, old, compact and dim star) and a lower mass companion star that is either on the main sequence or more evolved, commonly a red giant. When mass transfer through the inner Lagrangian point ensues, the white dwarf primary accretes an enveloping mass of hydrogen-rich material and accumulates it on its surface. The densities and temperatures that follow enable powerful nuclear reactions. The fate of the white dwarf depends on many factors, e.g. the orbital period of the binary system, the mass of the white dwarf and the rate at which it accretes mass from its companion. Two main different classes of events may occur[2]: either the massive white dwarf undergoes a thermonuclear carbon explosion that fatally disrupts and unbinds the whole star, or an explosive hydrogen ignition takes place at the envelope on the star's surface, expelling the previously accreted envelope. The former are called *supernovae* of type Ia (SNIa) and the latter *classical novae*[3], which

[1] There are Chinese catalogs of stars as old as 220 BC, referring as variable stars as "guest stars", [Xu et al. 2000].

[2] These are sub-classes of the so-called cataclysmic variables.

[3] Often in the literature the abbreviation CN for classical nova, or CNe for its plural, is used. We avoid this convention due to the homonymous abbreviation for the carbon-nitrogen cycle as CN cycle.

are the subject of this work.

Supernovae are commonly known from novels, science fiction series and video games. They are the most violent stellar events. In science, their interest stems in great part from the use of Type Ia supernovae as "cosmic distance rulers", or standardizable candles. During explosion, their intrinsic luminosity and the shape of their lightcurve (the light output as a function of time) are related. Measuring it, one can derive their distance from the observer. This characteristic makes Type Ias invaluable tools for cosmology, allowing us to measure the size and expansion of the visible universe. The distinction from classical novae only became clear in the late 19th century, when novae such as T Aurigae were observed to have different characteristics than *super*novae such as S And. The argument about the existence of (at least) two different kinds of objects was settled in the 1920s during the "Great Debate".

The interest in and study of Classical Novae is multifaceted. Due to relations between their peak brightness and their decay rate, they can be used as distance indicators [della Valle & Livio 1995]. They are also prominent producers of cosmic dust: in the expulsion of the envelope, great quantities of small condensed particles are released into the interstellar medium [Gehrz et al. 1998]. These dust grains have isotopic ratios that are not reflected in the interstellar medium, probably hinting at the composition of their source material at the time of their condensation from gas into grains, revealing many aspects of the nucleosynthesis of their host star and making them identifiers of star classes. Novae are also of interest for galactic chemical evolution, as they are the principal source of elements such as ^{13}C, ^{15}O and ^{17}O [José & Hernanz 1998]. The nature of the progenitors of Type Ia supernovae is a heated research topic, to which the study of Classical Novae may yet yield fruitful answers: Because the explosion in classical novae happens only at its outskirts, in the bottom layers of its accreted hydrogen shell, only these enveloping layers are expulsed, leaving the white dwarf itself intact. In principle, this process can repeat itself in long periods of $10^4 - 10^5$ years, depending on the orbital parameters of the binary system. For very massive white dwarfs, this period can be much shorter, in the range of $10 - 100$ years [José & Iliadis 2011]. Indeed several outbursts have been observed in the same nova. The first was T Pyxidis, observed for the first time in 1890 but glimpsed again in 1902 (its latest outburst was as recent as April 14, 2011, see Figure 1.1). It has been conjectured that massive white dwarfs, near the critical Chandrasekhar mass, could expel less mass in the outburst than they accrete in the period between explosions, so that they gradually gain mass, nearing the conditions that ignite a runaway of carbon fusion in its core, and leading to a SNIa. These conditions have been found for the recurrent novae U Scorpii [Kahabka et al. 1999] and RS Ophiuci [Osborne et al. 2011].

Thus, Classical Novae are at the intersection of astronomy, astrophysics, nuclear physics and cosmochemistry. Furthermore, a branch of study of classical novae focuses on the theoretical modeling of the ignition process: the thermal state of the white dwarf and its accumulated envelope, the fusion of elements and its associated energy release, and ultimately the ejection of matter into the interstellar medium. As mentioned above, elements such as C, N, O and up to Al are observed in their ejecta [Gehrz et al. 1998; José & Hernanz 1998; Starrfield et al. 2009], some of them in amounts up to 1000 times higher than in the Sun. The presence of these isotopes in such

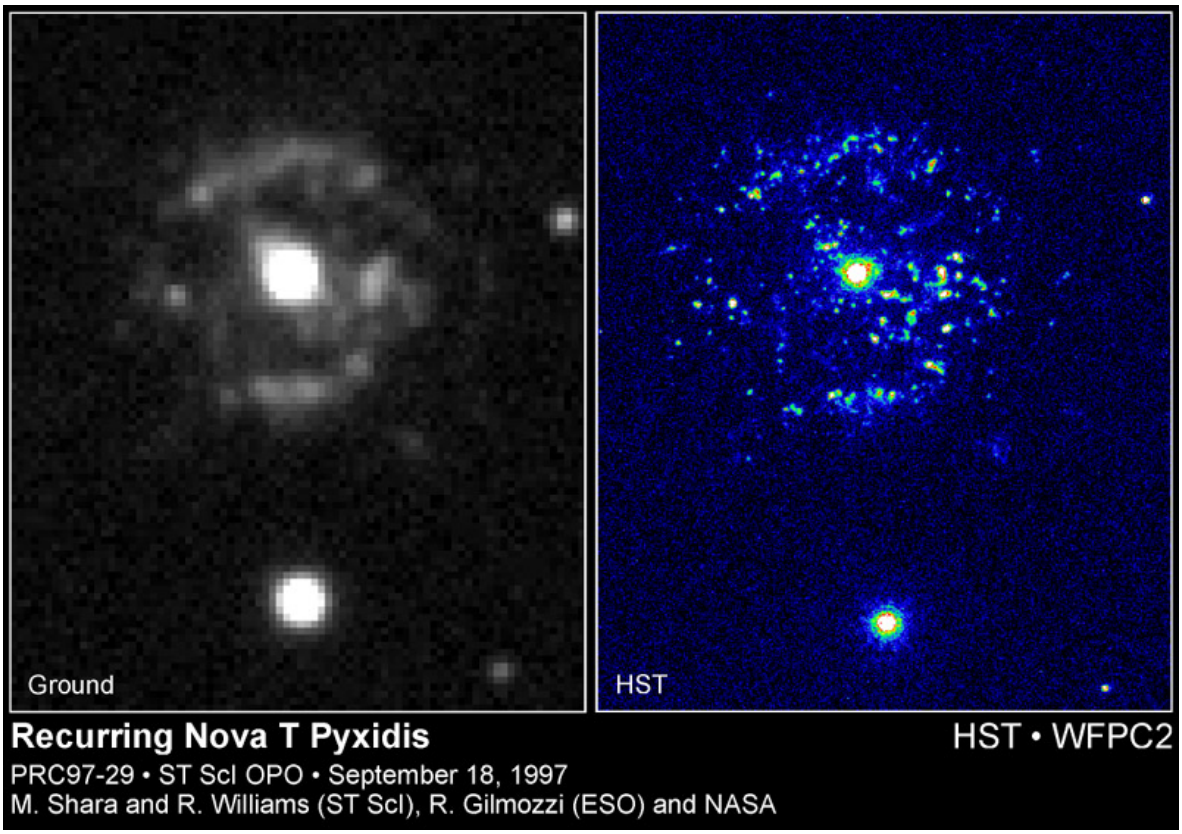

Figure 1.1.
Two images of the recurrent nova T Pyxidis. The left image shows the explosion as seen with ground based telescopes. A ring or spherical shell is seen ejected from the system. The right panel shows the same nova observed with the Hubble Space Telescope. The shell is revealed to be composed of many thousands elements [Shara et al. 1997].

extreme abundance is enigmatic, because the timescales expected for the TNR to occur (in the order of minutes) are too short to allow a heavy nuclear processing of the hydrogen-rich envelope to higher mass elements. This has lead to the conclusion that there must be some sort of mixing of matter between the hydrogen envelope and the outermost layers of the white dwarf —composed of C and O, and where traces of Ne, Mg and other elements can reside— at some point before or during the TNR. In this work we focus on the last moments leading up to the explosive outburst. Computer programs that solve the equations of stellar evolution in one spatial dimension provide a theoretical model of the white dwarf primary and its envelope just minutes prior to explosion. At this point, the envelope is fully convective and many details and open questions regarding the mixing of matter are sensitive to a correct description of convection, which can only be approximated in one dimension. This is one of the motivations for this work, to study the explosion in two and three dimensions in a novel computer code.

This introduction presents an overview of classical novae needed for a solid foundation to understand them from the theoretical modeling point of view. In Section 1.1 we briefly present the binary system and its characteristic astronomical features, the

nova lightcurve properties and interesting isotopes found in their spectra. These are explained in the framework of the *thermonuclear runaway model*, our current understanding of the explosion's origin. In Section 1.2.2, we review the work of the last decades regarding 1D and multi-D simulations of the reactive flow. We conclude in Section 1.3 by pointing out the gaps in our knowledge of novae, and stating the aims and goals of this dissertation. For more details on observations and classifications, the reader is referred to Bode [2011]. For a review of theoretical modeling, the author wholeheartedly recommends José & Shore [2008], José et al. [2006] and José & Iliadis [2011].

1.1. Classical novae: the basic picture

1.1.1. Astronomical properties

Nova outbursts arise in binary systems of a white dwarf (primary) and a companion that is either a main sequence or more evolved star (secondary). They are in a close orbit, with periods of 1 h – 12 h [José & Iliadis 2011][4]. The companion must be a low mass star. After the companion star has filled its Roche lobe, mass flows through the Lagrangian point and creates an envelope around the WD (white dwarf). The accretion rate is typically $\dot{M}_{\rm acc} \sim 10^{-9}\,M_{\odot}{\rm yr}^{-1}$ [Warner 2008]. A nova's defining characteristic is a light curve with a rapid rise in optical emission in a few days, that declines steadily after achieving its maximum brightness. While in the quiescent state, the binary system has a luminosity of $\sim 1 L_{\odot}$ and at outburst rises to a few $\times 10^4\,L_{\odot}$, which is approximately equal to or above the Eddington luminosity for a $1\,M_{\odot}$ WD [Bode 2011]. The rate at which brightness declines after maximum—specifically, the time taken for the optical luminosity to decline by two magnitudes—is used to sort them into 'speed classes'. A fast nova will take $t < 25$ d to decay by this amount, while a slow nova can take $t > 80$ d [Glasner & Truran 2012]. The speed class is not only an empirical classification method, the luminosity decay rate is in fact closely linked to the ejecta velocity and the peak absolute magnitude: a faster nova will have faster ejecta and higher luminosity. These relations depend on the fundamental physical properties of the system: the mass of the accreting white dwarf, the temperature at the core and the accretion rate. In our Galaxy, outburst rates of $(31 \pm 11)\,{\rm yr}^{-1}$ have been estimated, although this is probably a lower limit [Starrfield et al. 2009; José et al. 2006; Shafter 1997].

The total radiant energy released during classical novae outbursts ranges between 10^{45} erg and 10^{46} erg [Warner 2008]. The nuclear energy release rates have values of up to $10^{18}\,{\rm erg\,g^{-1}\,s^{-1}}$. Because the white dwarfs survive their classical nova outbursts, they are suspected to recur. It is estimated that around 10^4 to 10^5 flashes could occur in a single system [José & Iliadis 2011, and references therein]. The inter-outburst period of recurrent systems can range from hundreds of thousands of years to just decades [José & Iliadis 2011]. In our Galaxy, only ten recurrent novae have been sighted [Schaefer 2010]. The most prominent example is RS Ophiuci, which is known to have experienced eight outbursts since 1898 (either through direct observation or

[4] For a comprehensive list of orbital properties of classical and recurrent novae refer to Bode [2011] and Anupama [2008].

retroactively through archival data), the last instance being in 2006 [Bode 2011]. RS Oph is one of the best studied recurrent novae, and a favorite candidate for a SNIa progenitor [Osborne et al. 2011].

The atomic make up of the white dwarf and of the accreted matter is of critical importance for the nuclear processes that ultimately give rise to the thermonuclear flash on its surface [Shen & Bildsten 2009]. The composition and mass of the star are a result of its evolutionary history. White dwarfs are the final states of low mass stars, those that start their lives in the main sequence[5] with a mass of less than $M_{\rm ZAMS} \sim 10 M_\odot$. During this long period, their main energy source is hydrogen fusion into helium. After they expand into red giants, helium is burnt into carbon and oxygen by means of the triple-alpha process and their outer layers are expelled in a so-called planetary nebula[6]. For this reason, most white dwarfs are composed of carbon and oxygen (CO type). The more massive cores ($M_{\rm ZAMS}$ between $8\,M_\odot$ and $10.5\,M_\odot$) can reach temperatures sufficient for carbon fusion, in which case the remaining degenerate core will be made up of oxygen and neon (ONe type). When the white dwarf goes nova, it expels its envelope with velocities from a few 10^2 km s^{-1} to a few 10^3 km s^{-1}. Masses of about $10^{-5}\,M_\odot$ to a few $10^{-4}\,M_\odot$ are released into the interstellar medium [Bode 2011; Moore & Bildsten 2012]. Spectroscopic analyses indicate that the ejecta have highly enhanced abundances of isotopes of the carbon-nitrogen-oxygen (CNO), aluminum-magnesium (AlMg) and neon-sodium (NeNa) range compared to solar values [José & Hernanz 1998; José et al. 2006; Gil-Pons et al. 2003; Livio & Truran 1994; Gehrz 2008].

Classical novae are also interesting as gamma ray sources. The most intense emission predicted is a 511 keV line [Hernanz et al. 1999; Coc et al. 2000; Wiescher et al. 2010] and a continuum at lower energies around 10 keV – 30 keV [Clayton & Hoyle 1974; José et al. 2006, and references therein]. The fast emission of gamma rays shortly after peak temperature is thought to be due to positrons from the β^+decays of ^{13}N and ^{18}F annihilating with the electrons of the surrounding plasma [José et al. 2006, and references therein]. Novae were also long speculated to be producers of ^{7}Li [Starrfield et al. 1978]. The theory of *big bang nucleosynthesis* (BBN) has been very successful at predicting the abundances of light elements ^{1}H, ^{2}H, ^{3}He, ^{4}He formed after the universe became transparent to photons. However the observed abundance of lithium in old stars in galactic halos is at odds with the predicted values, being significantly lower than expected (for a review on the primordial lithium problem see Fields [2011]). Possibly, the primordial abundance of lithium is depleted in stellar interiors. On the other hand, its presence in young metal-rich stars point towards production on a galactic scale. The production of lithium in classical novae would help solve this discrepancy and further cement the validity of BBN. Early theoretical calculations proposing significant synthesis of ^{7}Li during nova outbursts and the first claims of its detection were controversial. However, as recently as July 2015, the first clear detection of lithium has been published [Izzo et al. 2015]. A team working with telescopes at La Silla Observatory identified an absorption line at $\lambda = 6708$ Å

[5] The *main sequence* is the phase of stars where stable hydrogen burning in the core takes place, and the longest, most stable phase. The abbreviation ZAMS stands for Zero Age Main Sequence, see Kippenhahn et al. [2013, Chapter 22]

[6] A term that has nothing to do with planets and has a historical reason.

stemming from $^{7}\mathrm{Li_I}$ in the ejecta of Nova V1369 Centauri. The authors put an estimate to the amount of lithium that a single nova can introduce into the galaxy as $M_{\mathrm{Li}} = 0.3 \times 10^{-10} - 4.8 \times 10^{-10}\ M_{\odot}$.

Our present understanding of the underlying physical processes responsible for the astronomical observations of novae are encapsulated in the so-called thermonuclear runaway model, which we illustrate in the next section.

1.1.2. The thermonuclear runaway model

Classical novae originate from stellar binary systems, in which a CO or ONe white dwarf of initially low luminosity ($L \sim 10^{-3} - 10^{-2}\ L_{\odot}$) accretes hydrogen-rich material from its companion star. The accretion rate must be in a specific range to permit the accumulation of an envelope on top of the white dwarf, typically $\dot{M}_{\mathrm{acc}} \sim 10^{-10} - 10^{-9} M_{\odot}\mathrm{yr}^{-1}$ [Wolf et al. 2013, and references therein]. At higher accretion rates lies the *stable hydrogen burning regime*, where the accreted mass is burnt at the same rate as it is consumed. If mass is accreted even faster, the nuclear burning cannot process all matter and it piles on top of the white dwarf, creating a red giant-like object. As matter is piled up on the WD's surface, the envelope is compressed and heated due to the strong gravitational potential. The material becomes both hot and electron degenerate. When temperatures reach $T \sim 10^{7}\,\mathrm{K}$, nuclear hydrogen burning starts at the bottom layers of the envelope through the proton-proton-chains. The ongoing nuclear reactions release energy into the envelope and heat it, but due to the degenerate conditions, the envelope cannot readjust the hydrostatic equilibrium by expansion, so that temperatures continue to rise. As radiation cannot transport all the heat fast enough away from the burning zone, convection in the envelope ensues, transporting the newly synthesized elements to higher layers of the envelope and enriching it with heavier elements. At temperatures above $T \sim 2 \times 10^{4}\,\mathrm{K}$, the nuclear time scale becomes shorter than the accretion time scale, such that the effects of accretion become negligible [José & Hernanz 1998]. The convective motions at the bottom of the envelope stir the material at the boundary between the envelope and the WD's surface, thereby *mixing* the matter across the boundary. When carbon and oxygen are dredged up from the white dwarf to the envelope, nuclear energy generation proceeds through the more efficient carbon-nitrogen-oxygen cycle, a process that converts four protons into a helium nucleus by a succession of proton captures unto CNO isotopes and radioactive decays. Its primary reaction is $^{12}\mathrm{C}(p,\gamma)^{13}\mathrm{N}$, which then decays by $^{13}\mathrm{N}(\beta^{+},\nu)^{13}\mathrm{C}$ (for details on thermonuclear physics discussed in this section, refer to Section 2.2.3 or Wiescher et al. [2010]). The rate of energy generation ϵ from the so-called 'cold' CNO cycles is limited by the cross sections of the proton capture reactions, which are temperature dependent. But while the rates in the *pp* chains grow moderately as $\epsilon_{pp} \propto T^{4}$, the CNO cycle has a much steeper temperature dependence of $\epsilon_{\mathrm{CNO}} \propto T^{18}$. As temperatures reach values above $T \sim 10^{8}\,\mathrm{K}$, reaction paths previously inaccessible at lower temperatures, such as $^{13}\mathrm{N}(p,\gamma)^{14}\mathrm{O}$, are unlocked. These extended cycles are dubbed 'hot' CNO cycles or HCNO. At such temperatures, the time scales of proton captures become shorter than the β^{+}decay half lives of the radioactive nuclei, which range from 1 min – 10 min and are insensitive to temperature, so that the abundances of CNO isotopes cluster around the β^{+}unstable nuclei. The slowest reactions and those which determine the

energy generation rate are the β^+decays. Therefore, the HCNO cycles are also known as the 'β^+–limited' CNO cycles. When the radioactive isotopes finally decay in the upper, cooler strata of the envelope, the sudden rise of entropy lifts the degeneracy and allows for the expansion and ejection of the envelope, now enriched with CNO elements [Starrfield et al. 1972, 2008].

Material burning stably via the (H)CNO cycle slowly converts hydrogen, over many full cycles, into heavier elements of the mass range $A < 40$. The time scales ($\sim$ min) and temperatures ($\sim 10^8$ K) expected to develop during the thermonuclear runaway in novae are much shorter/lower to be able to synthesize solar-like material to significantly higher values. Temperatures are not expected to surpass the critical temperature $T_{\mathrm{crit}} = 4 \times 10^8$ K at which breakout from the HCNO occurs [Wiescher et al. 1986]. However, the isotopic abundances detected in nova ejecta can be as large as $f \gtrsim 1000$, with $f = X_i/X_{i,\odot}$, where X_i is the mass of matter made up of the isotope i with respect to the whole mass [José & Hernanz 1998]. Therefore, the presence of large amounts of CNO isotopes in the ejecta is understood to be an indication of mixing between the white dwarf's uppermost layers and the envelope [Livio & Truran 1994]. The specific mixing mechanism is as yet a matter of debate [see e.g. Starrfield et al. 2008; Starrfield 2001; Gehrz et al. 1998, and references therein].

The cause of the final ejection of matter from the system is also as yet unclear. A supersonic wind driven by the super-Eddington luminosity [Kato & Hachisu 1994] and expansion of the ejecta as a result of its common-envelope interaction with the companion star have been suggested [e.g. Livio et al. 1990].

1.2. Numerical simulations of classical novae

Astronomical observations of classical nova light curves and spectra provide clues about the mechanism behind their powerful explosions. But the scales in which the thermonuclear runaway presumably operates are just a few hundred to thousand kilometers on the surface of white dwarfs. These are distances that cannot be resolved with telescopes, and the timescales of mass accretion are many orders of magnitude longer than human life spans, so the details of the explosions cannot as yet be studied directly. The thermonuclear runaway is a theoretical model to explain the observations. First proposed by Starrfield et al. [1972], it is based on numerical solutions of the equations of stellar evolution, which describe the structure of stars and its change in time. These are coupled with nuclear reaction networks, which are systems of equations that represent the nuclear reactions involved.

We define the relevant timescales of the different processes that rule the evolution of the classical nova outburst in Section 1.2.1. With these we can more easily understand the TNR and discuss the practicability of numerical simulations. In Section 1.2.2 we review previous work in the field.

1.2.1. Defining timescales

The *accretion timescale* is the time in which mass infalling from the white dwarf's companion star increases the envelope's mass,

$$\tau_{\mathrm{acc}} = \frac{M_{\mathrm{acc}}}{\dot{M}_{\mathrm{acc}}}. \tag{1.1}$$

With typical accretion rates of $10^{-10}\,M_{\odot}\mathrm{yr}^{-1} - 10^{-8}\,M_{\odot}\mathrm{yr}^{-1}$, and masses of $M_{\mathrm{acc}} \sim 10^{-5}\,M_{\odot} - 10^{-6}\,M_{\odot}$, the timescales range from $\tau_{\mathrm{acc}} \sim 10^{4}\,\mathrm{yr} - 10^{5}\,\mathrm{yr}$.

The *nuclear burning timescale* is usually expressed as $\tau_{\mathrm{nuc}} = E_{\mathrm{nuc}}/l$, with the luminosity l, when estimating the energy budget of stars. In our context it is expressed as

$$\tau_{\mathrm{nuc}} \sim \frac{c_P T}{\epsilon_{\mathrm{nuc}}}. \tag{1.2}$$

Here, c_P is the specific heat. Because of the very steep dependence of the nuclear energy generation rate ϵ_{nuc} on temperature T, τ_{nuc} drops fast as temperature increases. It is not only related to the rate of energy release, but consequently also on the change in composition of the burning. For this reason, it is also commonly expressed in terms of the mass fractions, e.g. X_i:

$$\tau_{\mathrm{burn}} = \frac{X_{\mathrm{i}}}{\dot{X}_{\mathrm{i}}}. \tag{1.3}$$

The *dynamical timescale* is the ratio between a characteristic length and velocity of a system. At the base of the envelope, the determining length scale is H_P, the *pressure scale height*. It is the distance in which pressure P decreases by $1/e$. Pressure gradients are equalized by sound waves with the local sound speed c_s. Therefore:

$$\tau_{\mathrm{dyn}} \sim \frac{H_P}{c_s} \sim \frac{1}{g}\sqrt{\frac{P}{\rho}}, \tag{1.4}$$

At very high densities ρ, τ_{dyn} can drop to the order of seconds.

Finally, the convective eddies circulate with a typical *convective turnover timescale* [Montesinos et al. 2001]

$$\tau_{\mathrm{conv}} = \frac{H_P}{v_{\mathrm{conv}}} \tag{1.5}$$

where v_{conv} is the convective velocity.

Multidimensional simulations of stars are challenging, even with today's massively parallel computing's capability of splitting the work between thousands of computer cores. The size of the spatial discretization, that is, how finely the studied region is divided into discrete *grid cells*, increases the computational cost. But also the temporal discretization – how many *time steps* are needed for the duration of the simulations – determines the total amount of work. The length of the numerical time step is usually limited by the sound speed of the fluid and the spatial resolution. For our case, during the build-up phase of the envelope, as mass spirals onto the white dwarf and nuclear activity is scarce, $\tau_{\mathrm{acc}} \leq \tau_{\mathrm{nuc}}$, so accretion is the determining

timescale, which is of the order of $\tau_{\rm acc} \sim 10^4\,{\rm yr} - 10^5\,{\rm yr}$. This phase elapses in *low Mach numbers*, that is, in conditions where the velocity of fluid motions is much slower than the sound speed: the ratio ${\rm Ma} = u/c_s$ is of the order of ${\rm Ma} \sim 10^{-6} - 10^{-2}$. Therefore, many steps are required to resolve sound waves which, in fact, do not have an effect on the dynamics of the system. Fortunately, the picture changes as temperatures at the bottom of the envelope rise, and the envelope nears the TNR. Nuclear reactions proceed at much faster pace, and nuclear burning time reduces from years to seconds when temperatures are higher than $10^8\,{\rm K}$, so that accretion becomes negligible. The convective turnover time is $\tau_{\rm conv} \sim 10^1\,{\rm s}$ and the pressure scale height is a few hundred km. All these scales converge to make it feasible to simulate a region around the interface between white dwarf and envelope, having a dimension of a few pressure scale heights, for many dynamical times.

1.2.2. Previous work

In this section we present an overview of the advances in the theoretical understanding of novae. For a detailed account of the history of the theory since Newton and before, we refer the reader to Duerbeck [2008]. In the present work we are interested in the developments since the 1970's. The results from numerical simulations with 1D evolutionary codes and analytical calculations with physical assumptions paved the ground for our contemporary multidimensional simulations.

The picture of the thermonuclear runaway as exposed in Section 1.1.2 was laid out by Starrfield et al. [1972]. In this seminal work, a Lagrangian code was coupled to a nuclear reaction network to study thermonuclear runaways on white dwarfs. The envelope, with solar abundances, was placed in situ without taking accretion into account. The authors found that during the TNR, temperatures reach values of $3 \times 10^8\,{\rm K}$. At such temperatures the nuclear burning time is around a thousand of a second, and the CNO cycle proceeds far form equilibrium, as convection and mixing from the convective boundary constantly change the abundances in the envelope. During peak temperatures, the β^+-unstable nuclei become the most abundant elements, except for ^{1}H and ^{4}He.

There is general consensus that the origin of novae are thermonuclear runaways in white dwarf envelopes. The numerical calculations yielded similar results as those from observations. However, the inherent assumption of spherical symmetry in the stellar evolution equations meant that no conclusion could be drawn regarding the initial ignition of the TNR, whether it started from a single local eruption or simultaneously throughout the white dwarf's surface. Shara [1982] studied localized TNRs on the basis of semi-analytic models. In this picture, if a TNR initiates as a point-source ignition, and a 'lava-like' burning front spreads across the surface. A flame propagating laterally solely by heat transport would take tens of years to cover the entire stellar surface. However, this deduction was based on radiative and conductive transport considerations alone, and did not consider the effect that convection could have in the propagation of the flame. In contrast, Fryxell & Woosley [1982], similarly analyzing TNRs in thin stellar shells and surface layers, suggested that the burning wave in nova outbursts could be propagated by small scale turbulence. Making use of flame theory and dimensional analysis, the authors derived an expression for the velocity

of the deflagration front spreading across the stellar surface:

$$v_{\rm def} \sim \left(\frac{H_P \; v_{\rm conv}}{\tau_{\rm burn}} \right)^{1/2} . \tag{1.6}$$

With values typical of the bottom of the convective zone in classical novae, this formula yields $v_{\rm def} \sim 10^4\,{\rm cm\ s^{-1}}$ and therefore a time for the flame to traverse the whole surface in only $\sim 1.3\,{\rm d}$.

Fujimoto [1982], also using a semi-analytical description of the envelope, calculated its evolution from the ignition to the final stage. He found that the decisive parameter governing the fate of the TNR is the pressure at the base of the envelope:

$$P_{\rm b} = \frac{GM_{\rm WD}}{r_{\rm b}^2} \frac{M_{\rm env}}{4\pi r_{\rm b}^2}, \tag{1.7}$$

where G is the gravitational constant, $M_{\rm WD}$ is the white dwarf mass, $M_{\rm env}$ the envelope mass and $r_{\rm b}$ the radius of the burning shell (the base of the envelope), from the center of the star. Typical values range between $10^{18}\,{\rm dyne\,cm^{-2}}$ and $10^{20}\,{\rm dyne\,cm^{-2}}$ (these are not absolute values, as the critical pressure depends on the mass of the white dwarf; see also the discussion in Section 5.4 of Shen & Bildsten [2009]). For low P_b the electrons are not degenerate at the onset, the nuclear heating time scale is long even during peak ($\gtrsim 10^6\,{\rm s}$) and the flash proceeds slowly. However, for sufficiently large P_b the envelope develops under highly degenerate conditions, which lead to even higher pressures and temperatures of $\gtrsim$ a few $\times\, 10^8\,{\rm K}$.

The first multidimensional and fully hydrodynamic studies were performed by Shankar et al. [1992]; Shankar & Arnett [1994]. A 1.25 $M_\odot$WD was evolved in 1D and then mapped to 2D in the explicit and Eulerian code *PROMETHEUS* in polar coordinates. The area considered was a small wedge of $25\,{\rm km} \times 60\,{\rm km}$ at the burning region. Due to the subsonic velocities of the convective motions and the time-step constraint of explicit time-integration, only fractions of seconds could be simulated. This work found that strong temperature fluctuations arise due to the turbulent convective motions. These fluctuations make the fluid Rayleigh-Taylor unstable. Because the unstable blobs rose, expanded and cooled fast, the authors deduced that these fluctuations did not initiate the runaway. However, the limited time and length scales that they probed meant that a more advanced simulations were needed to determine the nature of the flame propagation in novae.

In their first of several papers on this subject, Glasner & Livne [1995] focused on the first eruptions of the TNR. These were the first multi-D calculations to study the TNR for several dynamical timescales. All previous simulations had been restricted to only a few seconds due to the limited hardware capabilities of the time. Glasner & Livne [1995] proceeded thus: the initial model was first computed from a one-dimensional Lagrangian evolution code and then sampled at a given time step onto a 2D code. The 1D simulations followed the evolution of a 1 $M_\odot$ carbon-oxygen WD with a prescription for mass accretion on the upper boundary. The composition of the accumulating mass is solar. When the temperature at the bottom of the envelope had reached $1 \times 10^8\,{\rm K}$, the simulation was stopped. At that point, only a few 10^2 seconds were left until outburst. Afterward, the envelope and the top layers of the WD, just below the envelope, were mapped to two dimensions to the *VULCAN* code [Livne

1993]. The lateral extension of the simulation box spans 0.1 π radians of the stellar sphere. The code is coupled to a nuclear reaction network of 12 isotopes in the CNO range [Starrfield et al. 1985], in order to simulate the CNO cycle. This procedure would become commonplace for all subsequent multi-dimensional nova simulations. The accreted envelope in their simulation was unstable against convection. A few seconds after the start of the run the first convective plumes arose from the numerical noise alone, at the white dwarf-envelope interface. The TNR evolved in two stages of burning. During the first 70 s of the run there is was quiet phase, with convection cells of velocities of (2 to 3) $\times 10^7\,\mathrm{cm\,s^{-1}}$ reaching up to 2/3 of the envelope's height and nuclear energy rates of $q = 2 \times 10^{14}\,\mathrm{erg\,g^{-1}\,s^{-1}}$. During this period, the peak temperature barely rises from $T = 1 \times 10^8\,\mathrm{K}$ to $1.1 \times 10^8\,\mathrm{K}$. In the second stage there are localized eruptions of fast burning with $q = 3 \times 10^{15}\,\mathrm{erg\,g^{-1}\,s^{-1}}$, each one surviving a couple of seconds. Due to the convective motions, streams of envelope matter penetrate into the cold CO layers underneath and dredge up fresh carbon and oxygen to the burning region. At $t = 100\,\mathrm{s}$ the envelope expands upwards at velocities of a few times $10^5\,\mathrm{cm\,s^{-1}}$, typical of nova models. Because the flow velocities are subsonic at all times, pressure waves travel faster and equalize the pressure along radial cells, making the expansion almost spherically symmetric. The authors concluded that the TNR in novae is regulated not by convection but by the expansion of the envelope.

In a second paper, Glasner et al. [1997] again considered a hydrogen-rich convectively unstable envelope on a $\sim 1\ M_\odot$ white dwarf, which they evolved first from a stellar evolution code. In the 1D simulation, no prescription for diffusion or mixing was included. During the quiet burning stage, the energy rate slowly increased from $8 \times 10^{41}\,\mathrm{erg\,s^{-1}}$ to $8 \times 10^{42}\,\mathrm{erg\,s^{-1}}$, and the abundance of ^{12}C went from its original solar value of 3.03×10^{-3} to around 0.15. Despite this enrichment, the temperature stayed nearly constant. The thermal energy is initially spent on heating the cold CO matter dredged up from the white dwarf. After a period of $\approx 150\,\mathrm{s}$ the energy generation rate was high enough for a runaway of the temperature to take place. The temperature at the source shell rose sharply from $1 \times 10^8\,\mathrm{K}$ to $2 \times 10^8\,\mathrm{K}$ within 90 s. Violent burning ensued, and mushroom-like structures spread over the envelope, carrying β^+-unstable isotopes to higher layers away from the base. From $t = 200\,\mathrm{s}$ to 240 s, the CO content in the hydrogen-rich strata increased from 15% to 30%. This enrichment was attributed to Kelvin-Helmholtz (KH) instabilities at the base of the envelope. These are excited by the shear flow at the core-envelope interface induced by the convective motions. With linear theory [Chandrasekhar 1961], the authors found that minimal unstable wavelength of the KH instability in their white dwarf-envelope transition is $\lambda_{\mathrm{inf}} = 5 \times 10^5\,\mathrm{cm}$. The smallest scales resolved in their grid were $7 \times 10^5\,\mathrm{cm}$. Glasner et al. [2007] were interested in the role that temperature fluctuations played at the interface, and the spread of the flame front. Two timescales regulate the development of temperature fluctuations. A positive temperature fluctuation will increase the burning rate in a bubble of size l, which will expand in order to equalize its pressure with the background on a timescale

$$\tau_p = l/c_s. \tag{1.8}$$

After the equalization of pressure, the buoyant bubble will travel a distance ΔR in

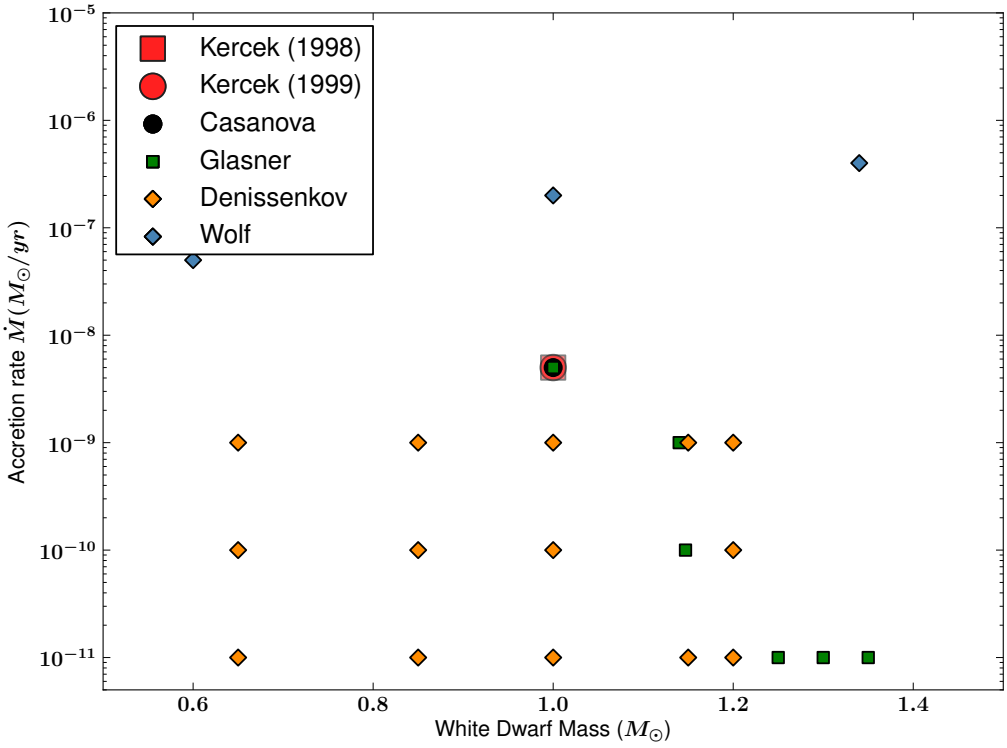

Figure 1.2.
The initial configurations of the novae studied in the literature listed in Table 1.1. Wolf et al. [2013]'s models lie along the line of stable hydrogen burning. Below it, unstable burning leads to a thermonuclear runaway.

the time

$$\tau_{\rm buo} = \left(\Delta R / \left(\frac{g\Delta\rho}{\rho}\right)\right)^{1/2}, \tag{1.9}$$

until it cools down to the background temperature. Calculating ΔR for several perturbation amplitudes, they found values for velocities and length scales that agreed with the general aspects of the flow in their 2D simulations Glasner et al. [1997, Table 2]. Furthermore, if the two timescales regulating the perturbations, and consequently the burning rate, are much shorter than the burning time $\tau_{\rm burn}$ (Equation (1.3)), then the regulation is a local process. They found this is the case, with τ_p and $\tau_{\rm buo}$ in the order of 10^{-1} s, and $\tau_{\rm burn} \leq 100$ s. The authors speculate that the lateral dissipation of energy should proceed by convection and convection-induced turbulence, supporting the conclusion of Fryxell & Woosley [1982].

Simultaneously, studies were performed by Kercek et al. [1998], henceforth referred to in the text as KHT1[7]. They used a modified version of the Eulerian code *PROMETHEUS* [Fryxell et al. 1989] and the same stellar initial conditions as Glasner et al. [1997]. However, their calculations were carried out in plane–parallel geometry,

[7] We discuss their work in Section 4.1 in more detail.

because they observed what seemed to be unphysical symmetries in the Glasner et al. runs when using polar coordinates. They chose a similarly dimensioned domain of about 1800 km × 1100 km and performed two simulations in a 'coarse' and a 'fine' resolution, where the grid cells are not equidistant in the radial direction. The areas of the smallest cells at the WD-envelope transition were $\sim 5\,\mathrm{km} \times 5\,\mathrm{km}$ and $\sim 1\,\mathrm{km} \times 1\,\mathrm{km}$ respectively. The results were very distinct from those of Glasner et al. [1997]. Their TNR developed more slowly, reached lower peak temperatures and slower velocities. Indeed, they found that their peak velocities were two orders of magnitude smaller than the escape velocity of the white dwarf, meaning the TNR would lead to no mass ejection. Comparing snapshots of the velocity fields in both studies, large differences in the convective flow patterns became evident. In Glasner et al. [1997] large turbulent eddies dominate the envelope, while in KHT1 small stable eddies are present. These were interpreted as stable solutions of the time-independent Euler equations. They achieve convective velocities of near sound speed, yet they do not penetrate into the CO core. Therefore, a great fraction of the kinetic energy is trapped in the eddies, inhibiting faster enrichment of the envelope, ultimately leading to a less violent TNR.

Next, Kercek et al. [1999] (henceforth KHT2) performed what would be the only 3D simulations of a classical nova for almost 12 years. They applied the same initial conditions as in their previous paper in a domain of $1800 \times 1800 \times 1000\,\mathrm{km}^3$ in the coarse resolution, due to limited computational resources. They also ignited a larger area at the interface than in the 2D case, to save computation time. They ran the calculation for 400 s. Motivated by the slow TNR they previously obtained due to insufficient C and O in the envelope, they increased its metallicity from $Z = 0.02$ to $Z = 0.1$ in a second simulation, hoping to be able to compare the results with similarly set up 1D simulations, in which the metallicity is increased to several factors higher than solar in order to achieve a fast nova. In the solar metallicity 3D run they found no stable eddies, but a very irregular velocity field, with sudden eruptions and recurrent quiet burning phases. The velocities near the bottom of the envelope remain subsonic. The peak temperature and velocities are achieved faster than in the 2D case, but this is merely because they chose a larger ignition area. After 200 s the whole envelope is stirred and in a steady burning state. The authors found that the total energy generation rate due to nuclear reaction yields $Q_{3\mathrm{D}} = 5.8 \times 10^{44}\,\mathrm{erg}$, compared to $Q_{2\mathrm{D}} = 2.1 \times 10^{45}\,\mathrm{erg}$. Moreover, typical temperatures are 10 % – 20 % lower, velocities a factor of two below those in the 2D case and the metallicity was merely doubled to $Z \sim 0.04$ (compare to the much higher value in Glasner et al. [1997]: $Z = 0.3$). They concluded that the envelope cannot be self-enriched through convection alone and that other processes such as shear-induced instabilities at the interface or diffusive mixing during the quiescent phase must be responsible for the enrichment. Having concluded this, they ran a simulation with an envelope containing five times solar metallicity. Peak velocities of $2.0 \times 10^7\,\mathrm{cm\,s^{-1}}$ (twice as much as the low-Z run) were reached after only 80 s, but after 160 s a state of steady burning almost identical to the previous case is reached. They concluded that the temperature rising time is too long (~ 100 s) compared to the mixing efficiency, allowing the envelope to expand and cool. In the end, the simulations performed in 3D mixed even less material than the ones in 2D.

Glasner et al. [2005] investigated the effects of different boundary conditions on the

evolution of the TNR. Four different schemes were investigated: an Eulerian scheme with free outflow at the upper boundary, an Eulerian scheme with inflow+outflow at the upper boundary, an Eulerian scheme with no mass flux and finally a so-called *arbitrary Lagrangian-Eulerian* (ALE) scheme. In the latter, two stages are performed in a single time step. First, a Lagrangian explicit time step is performed. In the second stage, the grid and its flow are re-mapped with a a high-order explicit scheme into any desired grid. this the envelope to expand into a co-expanding mesh. The criterion for goodness of the method was the evolution of the critical pressure P_b (see Equation (1.7)). Ideally, P_b should remain constant during the slow phase of the TNR. The study showed that in the simulations with outflow and inflow+outflow pressure at the base of the envelope is lost very quickly and the runaway is quenched. With a close boundary, the streams that cannot flow outwards fall back in, artificially enhancing the convective velocities and the mixing and hence extending the TNR. They assert that only their ALE scheme is able to maintain the correct behavior of the pressure: constant during the slow phase of the TNR with a decline towards the envelope expansion phase.

Casanova et al. [2011] performed the most recently published 3D-simulation of the WD-envelope mixing process. They used the initial conditions of Glasner & Livne [1995] and mapped them onto a 3D mesh in the code *FLASH* with up to five levels of refinement. They argue that the highly inhomogeneous distribution of elements found in the individual convective blobs reflect the observed patterns in observed spectra of nova shells. As such, they interpret the observed inhomogeneities as the signature of turbulence developed during the thermonuclear runaway.

We now take a brief step backwards to mention some of the results of *one-dimensional stellar evolution* calculations, from which the initial conditions of the multi-D simulations are commonly obtained. Many global parameters of the white dwarf system, such as of the mass of the WD, its central temperature, luminosity, the accretion rate and composition of the accreted material, have an effect on the final outcome of the outburst, and span a very large parameter space, which can be explored only in 1D. We refer the reader to the according literature [e.g. José & Hernanz 1998; Denissenkov et al. 2013b; Wolf et al. 2013, and references therein], here we merely highlight the following important results.

- Larger white dwarf masses M_WD lead to faster accretion rates, due to the stronger gravitational force.
- For a given M_WD, lower accretion rates yield more powerful explosions. Higher envelope masses mean higher densities at the bottom layers and therefore more violent explosions. For this reason, processes that either lengthen the accretion phase or otherwise increase the final envelope mass up to the TNR, lead to more fierce outbursts. With fast accretion rates, the temperature at the bottom of the envelope rises faster. Then the time between the onset of accretion and the TNR is shortened.
- Lower initial luminosities and cooler WDs result in longer accretion times, and therefore stronger outbursts, for the same reasons as above.
- Some small part of the energy generated is transported inward via degenerate

electron conduction, but most of the energy is radiated to the surface [Townsley & Bildsten 2004]. If mixing between the envelope and WD material takes place during the accretion phase, the opacity in the burning region will increase. A higher opacity will trap the heat from nuclear reactions and gravitational compression, which in turn will raise the temperature in the burning region more quickly than in an envelope with lower opacity. This will shorten the time to the TNR, and hereby the total amount of matter accreted (and ejected) will be smaller [Starrfield et al. 1998].

– The kind of white dwarf primary, CO or ONe, does not only play a role because of the larger masses of the ONe type, but because of the elements contained in them, which determine the nuclear chains that will dominate during the TNR. The much lower abundance of ^{12}C in ONe white dwarfs reduces the energy generation through the CNO cycle prior to the TNR. This enables the growth of a more massive envelope.

These results should inform and guide the choice of an appropriate 1D initial model for further study in multi-D.

1.2.3. Three-dimensional stellar evolution

We have summarized the current state of the theoretical modeling of classical novae. The critical aspect leading to the TNR and being ultimately responsible for the ejection of matter is understood to be some sort of mixing across the white dwarf and envelope transition. This is a process that must be treated with approximative prescriptions when evolving the equations of stellar evolution (Sections 2.1 and 2.1.3). The full effect of mixing can only be clarified by means of three-dimensional simulations. At the writing of this thesis, only a few such simulations have been performed [Kercek et al. 1999; Casanova et al. 2011]. Kercek et al. [1999] point out that small scale dissipation and mixing are still dominated by numerical discretization effects. We will show in Section 3.2 that common numerical schemes develop excessive dissipation in the low Mach number regime. Other groups, working with the code *MAESTRO*, which is designed to cope with low Mach number flows, have also employed it for convective boundary mixing [Krueger 2012]. However, its application is limited exclusively to low Mach number flows, and as we will see in Chapter 4, the convective eddies in the nova envelope can develop high speeds and Mach numbers in the transonic regime.

Miczek [2013] developed a hydrodynamical code that solves the Euler equations in one, two and three dimensions. It is written in a modular fashion, separating time and space discretization by the method of lines; the geometry, the equation of state, and so on. One of the key virtues of the code is its implementation of *low Mach number preconditioning*, a method of modifying the flux functions such that the numerical viscosity which affects the schemes at low Mach numbers is neutralized [Miczek et al. 2015]. The hydrodynamics is coupled to a nuclear reaction network [Edelmann 2014]. The result is called the *Seven League Hydro code* or *SLH*. The ability to use (large) implicit time steps in low Mach number flows makes this code suitable for exploring phases of stellar evolution in three dimensions which were previously only possible in spherically symmetric simulations.

Publication	White dwarf composition	$M_{\rm wd}$ ($M_\odot$)	lg $\dot{M}_{\rm acc}$ ($M_\odot {\rm yr}^{-1}$)	Dimension
Casanova et al. [2011]	CO	1.00	-9	3D
Denissenkov et al. [2013b]	CO	0.65	$-9, -10, -11$	1D
	CO	0.85	$-9, -10, -11$	1D
	CO	1.00	$-9, -10, -11$	1D
	CO	1.15	$-10, -11$	1D
Denissenkov et al. [2013a]	CO	1.15		1D
	ONe	1.30		1D
Glasner & Livne [1995]	CO	1.00	—	2D
Glasner et al. [1997]	CO	1.00	-9	2D
Glasner et al. [2005]	CO	1.14	—	2D
Glasner et al. [2007]	CO	1.14	-1	2D
Glasner & Truran [2009]	CO	1.25	-11	2D
	CO	1.30	-11	2D
	CO	1.35	-11	2D
Glasner et al. [2012]	CO	1.147	-10	2D
	ONe(Mg)*	1.147	-10	2D
	He*	1.147	-10	2D
Kercek et al. [1998]	CO	1.00	-9	2D
Kercek et al. [1999]	CO	1.00	-9	3D
Wolf et al. [2013]†	CO	0.51 – 1.00	~ -7	1D
idem.	ONe	1.10 – 1.34	~ -7	1D

Table 1.1.
A selection of relevant literature for our work. Also listed are the masses of the white dwarfs and their accretion rates. Some of these pairs are plotted in Figure 1.2. A more extensive table can be found in José et al. [2006]. *Notes*: $*$ A layer of ONe(Mg) and He was added to the CO core. † Wolf et al. [2013] studied a large grid of nova masses and accretion rates to find the stable hydrogen burning regime.

1.3. Outline & goal of this work

In this work we continue on the path described in last section, the study of convective boundary mixing in nova outbursts. We employ *SLH* to perform multidimensional simulations from initial conditions based on the work of Kercek et al. [1999] and the stellar evolution code *MESA* [Paxton et al. 2011, 2013].

This thesis is structured as follows. Chapter 2 expands on the concepts of stellar evolution (Section 2.1), convection (Section 2.1.2) and thermonuclear reactions (Section 2.2.1). Chapter 3 explains the numerical methods employed, the low Mach number preconditioning (Section 3.2), and well-balancing (Section 3.3). The core of this work are Chapter 4, where we explain in detail the construction of our nova models, and Chapter 5, where the result of mixing and nucleosynthesis studies are presented. Finally, in Chapter 6 we conclude with a summary and an outlook of future work.

2. Astrophysical Background

Despite their tranquil appearance in the night sky, stars have long been known to be dynamic. While the flickering of stars in the night's sky is in fact due to Earth's atmosphere, and shooting stars are not stars at all, the detection of different colors, sizes, masses, and population numbers in clusters of stars, all point to stars participating in an universal cycle of birth, shine, and death. The rich star zoo we observe over our human life spans are actually different stages of the stars' cycles, mere snapshots in the millions and billions of years of star's life time. In this context, the classical nova outburst belongs to one possible final chapter in the life of white dwarf stars. The mathematical framework that connects all the pieces from observations and physical reasoning is the theory of stellar evolution, pioneered by Rudolf Kippenhahn, Alfred Weigert and Eva Meyer-Hofmeister [Kippenhahn et al. 1967]. This chapter is devoted to a brief exposition of it, as it plays a central role in any kind of stellar simulations. In the following sections, we follow mainly Kippenhahn et al. [2013] for the section on stellar evolution, and Wiescher et al. [2010] for the presentation of thermonuclear reactions.

2.1. Stellar structure and evolution

2.1.1. Basic equations

Stars are conventionally described by the equations of stellar structure. These equations, in their most simple from, assume that stars are perfectly spherical objects, both on the surface and in their internal structure. That is to say, that a star's structure is composed of concentric, spherical shells, along which physical values are constant and vary only radially. They are a set of partial differential equations expressed commonly in Lagrangian coordinates with the mass variable m [Kippenhahn et al. 2013]:

$$\frac{\partial r}{\partial m} = \frac{1}{4\pi r^2 \rho} \tag{2.1}$$

$$\frac{\partial P}{\partial m} = -\frac{Gm}{4\pi r^2 \rho} \tag{2.2}$$

$$\frac{\partial l}{\partial m} = \epsilon_n - \epsilon_\nu - c_P \frac{\partial T}{\partial t} + \frac{\delta}{t}\frac{\partial P}{\partial t} \tag{2.3}$$

$$\frac{\partial T}{\partial m} = -\frac{GmT}{4\pi r^4 P}\nabla \tag{2.4}$$

$$\frac{\partial X_i}{\partial t} = \frac{m_i}{\rho}\left(\sum_j r_{ji} - \sum_k r_{ik}\right). \tag{2.5}$$

This set of equations ignores mass loss at the surface (e.g. through stellar winds), the star's differential rotation, and magnetic fields. The first equations do not describe the evolution but the structure of the star (they do not contain any time derivatives). Here and in the following pages, a denotes the radiation constant, c the speed of

light, c_s the speed of sound, G the gravitational constant and g the gravitational acceleration.

The first of these equations describes the radial stratification of mass of a sphere with density $\rho(r)$. The second equation represents hydrostatic equilibrium: the gradient of pressure P acts outwards against the self-gravitational pull towards the center of the star and balances it out. The third equation describes the luminosity l, defined as the total energy emitted per unit time through a mass shell dm. Nuclear fusion, as one of the star's primary sources of energy (the other being the gravitational binding energy), enters the equation with the term ϵ_n, the nuclear energy generation rate. Neutrinos are also created in nuclear processes and since they escape the boundaries of the star unhindered, ϵ_ν is a negative contribution to the energy equation. The last two terms describe energy gain/loss through adiabatic contraction/expansion. They include the specific heat c_P, the temperature T and $\delta = -\partial \ln \rho / \partial \ln T$, a derivative of the equation of state. The fourth equation regards energy transport, which can proceed via radiation or convection. In a specific layer of a star, one type of energy transport will dominate over the other, and the quantity ∇ must be chosen according to the present manner of transport. In the case of radiation-dominated transport,

$$\nabla_{\text{rad}} = \frac{3}{16\pi a c_\gamma G} \frac{\kappa l p}{m T^4}. \tag{2.6}$$

This expression is a function of the stellar opacity κ (the transparency to photons), which in turn depends on the thermodynamic state and nuclear composition. In regions where the opacity becomes too large, radiation is not efficient enough to transport all the energy outwards. Then, buoyant motions can transport energy more efficiently and convection ensues (Section 2.1.2). In this case, ∇ is given by

$$\nabla_{\text{ad}} = \left(\frac{\partial \ln T}{\partial \ln P} \right)_s. \tag{2.7}$$

Convection, by nature, does not occur in spherical symmetry. Its inclusion in the stellar evolution equations can only be realized as an approximation, commonly some form of *mixing length theory* (see Section 2.1.3). Finally, the nuclear composition of the stellar matter changes dynamically, either through the fluid motions advecting nuclei, or their creation and destruction via nuclear reactions. The last equation describes these changes in terms of the mass fractions X_i, namely the fraction of the total mass inside the shell dm that is composed of the isotope i. The terms r_{ji}, r_{ik} in Equation (2.5) represent the reactions that create the isotope ($j \to i$) and destroy it ($i \to k$), respectively (see Section 2.3).

The theory of stellar evolution has been been hugely successful in explaining the observed stellar populations. Globular clusters are conglomerations of millions of stars in the halos of galaxies. Their age can be determined by looking at their state in the *Hertzsprung-Russell diagram*, which plots the state of the individual stars in a luminosity-temperature space. From the position of the stars in this space, the nuclear burning phases they have sustained can be derived, and with it their age. The oldest globular clusters have been found to have an age between 11 Gyr and 16 Gyr [e.g. Krauss & Chaboyer 2003] (the large error is due to the uncertainties in astronomical measurements.) This way, stellar evolution provides an independent measurement of

the age of the universe. Unfortunately the basic assumption of spherical symmetry cannot possibly hold in the more dynamic phases of the stars: pulsation, rotation, mass loss through stellar winds, or interaction with stellar companions. Also, the star is not necessarily on hydrostatic equilibrium during all stages of stellar evolution, therefore these equations are not valid at all points in stellar evolution. The basic equations must be complemented by additional expressions to account for these effects. We will elaborate on some of these limitations later on, limitations which are partly the motivation for our study in multiple dimensions.

2.1.2. Convection and dynamical stability

The equations presented in the last section assume stars are spherically symmetric, both in their shape and internal stratification. One can expect that in real stars, which are dynamical objects, fluctuations from the mean values averaged over a shell are always present, even in the more quiescent phases of the star. The question then emerges, whether these fluctuations remain small, or whether they will continue to grow. It is a question of *stability*.

Let us consider the fluctuation of a mass element (e) in relation to its surroundings (s) [Kippenhahn et al. 2013, Sec. 6.1]. To this end, the operator

$$DA = A_\mathrm{e} - A_\mathrm{s} \tag{2.8}$$

is introduced. Then, to a slightly hotter element corresponds a $DT > 0$. As pressure gradients are balanced by sound waves, which are in general faster than the motions of the fluid elements, its is reasonable to assume that the element is always in pressure balance with its background, and so it holds:

$$DP = 0. \tag{2.9}$$

For a gas with an equation of state as $\rho \sim P/T$, a fluctuation $DT > 0$ means $D\rho < 0$. The element is lighter than its surrounding medium and will be accelerated upwards by the buoyancy force $K_r = -gD\rho$ (per unit area). After the element has traveled a distance Δr from its original position, its density will contrast from the new surroundings by

$$D\rho = \left[\left(\frac{d\rho}{dr}\right)_\mathrm{e} - \left(\frac{d\rho}{dr}\right)_\mathrm{s}\right] \Delta r. \tag{2.10}$$

In this expression, $(d\rho/dr)_\mathrm{e}$ is the element's change of density while it rises, the term with subscript (s) is the background density gradient.

For a negative $D\rho$, the buoyancy force $K_r > 0$ lifts the element upwards, increasing the initial fluctuation, the stratification is unstable. If, however, $D\rho > 0$, then $K_r < 0$ and the element is accelerated back towards its original position. Thus, the condition for stability becomes:

$$\left(\frac{d\rho}{dr}\right)_\mathrm{e} - \left(\frac{d\rho}{dr}\right)_\mathrm{s} > 0. \tag{2.11}$$

Density gradients $(d\rho/dr)$ do not appear in the basic equations Equation (2.1) to Equation (2.5), but they can be related to the corresponding temperature gradients

via the equation of state. For simplicity, it is assumed that no exchange of energy takes place between the element and its surroundings, the process is *adiabatic*. Deep in the interior of the star, this is a valid assumption.

Consider the total differential of the equation of state $\rho = \rho(P, T, \mu)$:

$$\frac{d\rho}{\rho} = \alpha \frac{dP}{P} - \delta \frac{dT}{T} + \varphi \frac{d\mu}{\mu}, \tag{2.12}$$

where the partial derivatives are defined as

$$\alpha := \left(\frac{\partial \ln \rho}{\partial \ln P}\right), \quad \delta := -\left(\frac{\partial \ln \rho}{\partial \ln T}\right), \quad \varphi := \left(\frac{\partial \ln \rho}{\partial \ln \mu}\right). \tag{2.13}$$

The sign in the definition of δ is a convention, chosen so that for an ideal gas $\alpha = \delta = \varphi = 1$.

Inserting the differential in Equation (2.12) in Equation (2.11) we can rewrite the condition for stability in terms of temperature gradients:

$$\cancel{\left(\frac{\alpha}{P}\frac{dP}{dr}\right)_{\mathrm{e}}} - \cancel{\left(\frac{\alpha}{P}\frac{dP}{dr}\right)_{\mathrm{s}}} + \cancel{\left(\frac{\varphi}{\mu}\frac{d\mu}{dr}\right)_{\mathrm{e}}} - \left(\frac{\delta}{T}\frac{dT}{dr}\right)_{\mathrm{e}} + \left(\frac{\delta}{T}\frac{dT}{dr}\right)_{\mathrm{s}} - \left(\frac{\varphi}{\mu}\frac{d\mu}{dr}\right)_{\mathrm{s}} > 0. \tag{2.14}$$

The pressure dP derivatives vanish due to the assumption $DP = 0$. The composition gradient $d\mu/dr$ also vanishes for the element, when its original composition does not change as it is advected.

The *pressure scale height* is

$$H_P = -\frac{dr}{d\ln P} = -P\frac{dr}{dP}. \tag{2.15}$$

Multiplying the remaining terms of Equation (2.14) by this expression leads to the relation

$$\left(\frac{d\ln T}{d\ln P}\right)_{\mathrm{s}} < \left(\frac{d\ln T}{d\ln P}\right)_{\mathrm{e}} + \frac{\varphi}{\delta}\left(\frac{d\ln \mu}{d\ln P}\right)_{\mathrm{s}}.$$

In addition to the gradients ∇_{rad} and ∇_{ad} defined in Equations (2.6) and (2.7), the above quantities are defined as:

$$\nabla := \left(\frac{d\ln T}{d\ln P}\right)_{\mathrm{s}}, \quad \nabla_{\mathrm{e}} := \left(\frac{d\ln T}{d\ln P}\right)_{\mathrm{e}}, \quad \nabla_{\mu} := \left(\frac{d\ln \mu}{d\ln P}\right)_{\mathrm{s}}. \tag{2.16}$$

When P is considered as a measure of depth, then the derivatives can be interpreted as *spatial* derivatives of the quantities T and μ.Using the above definitions, the condition for stability becomes

$$\nabla < \nabla_{\mathrm{e}} + \varphi/\delta \nabla_{\mu}. \tag{2.17}$$

The gradient ∇_{rad} was defined for the case in which energy is transported by radiation only. If that is the case in the *actual* gradient ∇, then $\nabla_{\mathrm{rad}} = \nabla$. Applying again the assumption of adiabatic change, $\nabla_{\mathrm{e}} = \nabla_{\mathrm{ad}}$. Finally we finally arrive at the condition

$$\nabla < \nabla_{\mathrm{ad}} + \frac{\varphi}{\delta}\nabla_{\mu}. \tag{2.18}$$

This is known as the *Ledoux criterion* for dynamical stability. In case that the nuclear composition in a region is homogeneous, $\nabla_\mu = 0$ and the last equation becomes simply

$$\nabla < \nabla_{\mathrm{ad}}, \tag{2.19}$$

the so-called *Schwarzschild criterion*.

If the criteria are fulfilled, then the layers are dynamically stable, and the energy flux is carried by radiation. If the opposite is true, the region is unstable: small perturbations will grow and convective motions will ensue, carrying some part of the flux.

2.1.3. Mixing-length theory

Ludwig Prandtl developed a simple model of convection analogous to molecular heat transfer [Prandtl 1925]. In this model, the fluid 'bubbles' correspond to the molecules and the *mixing length* is equivalent to the mean free path. That is to say, the mixing length l_m is the distance a fluid element can flow before it is absorbed into its surroundings. These bubbles or "elements" have different temperatures DT/T and densities $D\rho/\rho$ than their surroundings, yet the assumption is made that they are in pressure equilibrium with them ($DP = 0$). This assumption is valid, provided that the element's speed is small compared to the sound speed c_s. We follow the derivation of Böhm-Vitense [1958] found in Kippenhahn et al. [2013, Sec. 7.1].

The total flux through a concentric sphere is the sum of radiative and convective fluxes $F_{\mathrm{rad}} + F_{\mathrm{con}}$. Equation (2.6) gives the stratification necessary for the energy to be transported solely by radiation,

$$F_{\mathrm{rad}} + F_{\mathrm{con}} = \frac{4acG}{3}\frac{T^4 m}{\kappa P r^2}\nabla_{\mathrm{rad}}. \tag{2.20}$$

Some flux is carried by convection, so the radiative flux depends on the actual gradient ∇:

$$F_{\mathrm{rad}} = \frac{4acG}{3}\frac{T^4 m}{\kappa P r^2}\nabla. \tag{2.21}$$

On the other hand, the convective flux is given by the mass flux ρv and the change in internal energy $c_P DT$ of the bubbles

$$F_{\mathrm{con}} = \rho v c_P DT = \frac{4acG}{3}\frac{T^4 m}{\kappa p r^2}\left(\nabla_{\mathrm{rad}} - \nabla\right). \tag{2.22}$$

Consider a convective stellar region with rising and sinking bubbles, and a given radial shell at radius r. The convective elements started their motion some distance away from r. The difference in temperature from its surroundings DT increases with the traveled distance, but the bubbles eventually merge with the surrounding fluid after having traveled the distance l_m. On average, they will have moved $l_m/2$ when crossing the shell r. Then the temperature difference is

$$\frac{DT}{T} = \frac{1}{T}\frac{\partial DT}{\partial r}\frac{l_m}{2} = (\nabla - \nabla_{\mathrm{e}})\frac{l_m}{2}\frac{1}{H_p}. \tag{2.23}$$

In the second step the temperature gradient $\nabla = \partial \ln T / \partial \ln P$ and the definition of the pressure scale height $H_p = \partial r / \partial \ln P$ were inserted. ∇_e is the gradient of the convective element. Using $\delta = -\partial \ln \rho / \partial \ln T$, the density contrast from the background reads:

$$\frac{D\rho}{\rho} = -\delta \frac{DT}{T}. \tag{2.24}$$

Then, the radial buoyancy force is

$$k_r = -g \frac{D\rho}{\rho}. \tag{2.25}$$

Using the same argument as above, one assumes that while crossing r, averaging over all bubbles, half of the work $k_r l_m/2$ has been done:

$$\frac{1}{2} k_r \frac{l_m}{2} = g\delta(\nabla - \nabla_\mathrm{e}) \frac{l_m^2}{8H_p}. \tag{2.26}$$

Further, if half of it used in the kinetic energy of the element $v^2/2$ (by mass) while the rest is lost to the surroundings, one obtains for the velocity

$$v^2 = g\delta(\nabla - \nabla_\mathrm{e}) \frac{l_m^2}{8H_p}. \tag{2.27}$$

Inserting Equation (2.27) and Equation (2.23) into the expression for the convective flux, Equation (2.22), gives:

$$F_\mathrm{con} = \rho c_P T \sqrt{g\delta} \frac{l_m^2}{4\sqrt{2}} H_p^{-3/2} (\nabla - \nabla_\mathrm{e})^{3/2}. \tag{2.28}$$

The final step is to consider convective element e and its change of temperature as it moves through the background. This can occur through adiabatic expansion or contraction and through radiative exchange with the surroundings. Approximating the convective bubbles as spherical, with volume V, surface S, and diameter l_m, one can derive the temperature gradient in the normal direction $\partial T / \partial n$ and find an expression for the radiative loss λ per unit time through the surface. Together with Equation (2.23) and assuming a form factor for the bubble $l_m S/Vd$, this leads to:

$$\frac{\nabla_\mathrm{e} - \nabla_\mathrm{ad}}{\nabla - \nabla_\mathrm{e}} = \frac{6acT^3}{\kappa \rho^2 c_P l_m v}. \tag{2.29}$$

The five equations Equations (2.20) to (2.29) constitute the mixing-length model. They provide expressions for the five quantities F_rad, F_conv, v, ∇_e and ∇. The task of this theory is to calculate ∇. However, the quantity missing is still the mixing length l_m itself. In its framework there is no equation to actually derive it. It remains a free parameter and the strongest caveat of the model. It is usually calibrated from observations, especially of the Sun, but it is assumed to be universal.

MLT in classical novae

An area where the limitations of MLT can critically affect the results is *convective boundary mixing* or CBM. The Ledoux criterion, Equation (2.18), dictates how the actual gradient ∇ ought to be behave radially, if a region can transport the energy flux solely by radiation or convection. It is a local description, and as such it defines a sharp division between stable and unstable layers. However, the boundaries between adjacent regions are more or less smooth transitions. Convective bubbles may cross the formal boundary into dynamically stable layers because of their inherent momenta. As such, there will generally be some degree of mass transfer across the boundaries of convective and radiative shells. This mixing is commonly treated in one dimension as a diffusive process, with a diffusion coefficient that decays exponentially away from the formal convective boundary r_0 [e.g. Freytag et al. 1996; Herwig et al. 1997; Herwig 2000; Paxton et al. 2013]:

$$D = D_0 \exp\left(-\frac{2|r - r_0|}{f H_p}\right). \tag{2.30}$$

D_0 is a diffusion coefficient calculated using MLT and f is a free parameter, which depends on the specific conditions at the boundaries. It also must be calibrated either by observations or multidimensional simulations. In 1D simulations of He-shell flash convection in post-AGB stars, for example, a value of $f \sim 0.008$ is routinely used [Werner & Herwig 2006; Herwig et al. 2006]. The boundary between the convective H-rich envelope and the stable CO core in classical nova progenitors is much stiffer. A value of

$$f_{\text{nova}} \sim 0.004 \tag{2.31}$$

is commonly found in the literature of one-dimensional classical nova simulations [e.g. Denissenkov et al. 2013b].

2.2. Thermonuclear astrophysics

It is widely accepted that the single parameter that most strongly determines the evolution of a star is its mass. Larger masses imply higher temperatures and pressures in the core. Therefore, energy must be generated in the core at a higher rate to balance gravity and stabilize the star. This means that a massive star must have a higher luminosity, consume its material faster, and consequently have a shorter lifespan than a less massive star. [e.g. Iliadis 2010]. The mechanism of energy generation, and the one ultimately responsible for the star's evolution, is nuclear reactions.

Nuclear fusion is the process by which two atomic nuclei coalesce to form another. Such union is inhibited by the strong repulsive force between nuclei. Extremely high energies are required to breach the barrier, yet the densities and temperatures found in stellar cores – in conjunction with a quantum-mechanical effect – allow for such a breaching to take place. Indeed, nuclear fusion was long theorized to be the origin of the Sun's light. Its hydrogen make-up was indicated by the observation of absorption lines in the spectrum of the sun – the Fraunhofer lines – that closely matched the lines of hydrogen [Kirchhoff 1860]. This assumption gained a foothold after Bethe

& Critchfield [1938] proposed a nuclear reaction chain (nowadays referred to as PPI chain) by which two hydrogen atoms are fused into deuterium, which then forms helium. Bethe [1939] and Von Weizsäcker [1938] found an alternative, cyclic, reaction sequence involving C, N and O isotopes, that equally results in He.

Heavier nuclei than hydrogen experience even stronger repulsion, and so even higher temperatures are required to force their fusion – temperatures that primarily depend on the star's mass. Higher temperatures unlock nuclear pathways that were previously unachievable, generating new elements and modifying the atomic composition of the star in the process. The escape from a given nuclear cycle to a higher region of more massive nuclei is often called *break-out*. The active nuclear cycles define the phase that a star is undergoing. The core temperature essentially defines which burning stages are accessible to the star. Therefore, the life of the stars is intimately entangled with the nuclear physics of their composing nuclei and as such, nuclear energy generation enters the theory of stellar evolution in Equation (2.3).

In the case of classical novae, it is the ignition of the hydrogen-rich mantle that has been accreted on its surface which is responsible for all the interesting nucleosynthesis and energetics that arise in these stellar systems. Therefore, we are mainly concerned with *explosive hydrogen burning* in this work. In this section, we will delve into the mechanisms that power the nova outburst. First, in Section 2.2.1 we will present some general aspects of nuclear physics, starting with a brief explanation of the quantum-mechanical basis of the reactions and expanding on the energy generation of thermonuclear reactions. In Section 2.2.2 and Section 2.2.3 we deal with specific reaction chains, the proton-proton chains and the CNO cycles.

2.2.1. Nuclear physics

The basis of charged particle fusion is the quantum tunnel effect. For this discussion we follow Iliadis [2010]. A simple model for the potential for nuclear reactions consists of an attractive square potential well of depth V_0 that represents the atomic nucleus ($0 < r < R_0$, region I) and a repulsive square barrier of height V_1 ($R_0 \leq r < R_1$, region II). In classical mechanics, if the energy E of an incident particle ($r \geq R_1$, region III) is smaller than V_1, it is not allowed to bypass the barrier. In quantum mechanics, the Schrödinger equation must be solved for each of the regions. In regions I and III, the solutions Ψ are sine functions, while in region II they are exponential functions. The derivatives of these functions at the interfaces R_0 and R_1 must be continuous. This continuity condition yields four equations that can be solved for the intensity of the transmitted wave in region I. The ratio of this intensity $|\Psi_\mathrm{I}|^2$ compared to the intensity of the impinging wave $|\Psi_\mathrm{III}|^2$ is called the transmission coefficient and is positive. That is, some part of the wave function tunneled through the barrier. In real nuclei, the potential is not a square barrier but the Coulomb potential (ignoring the centripetal barrier). The same formalism can be applied to this potential, treating it as n infinitesimal square barriers and going to the limit $n \to \infty$. The resulting transmission coefficient, for very low energies, becomes [Iliadis 2010]

$$\hat{T} \approx \exp\left(-\frac{2\pi}{\hbar}\sqrt{\frac{\mu}{2E}}Z_0 Z_1 e^2\right) \equiv e^{-2\pi\eta}, \tag{2.32}$$

where $\hbar$ is the reduced Planck constant, μ the reduced mass of the particles, Z_0 and Z_1 the charges of the nuclei and e the elementary charge. This tunnel probability has an energy dependance that goes as $\exp\left(1/\sqrt{E}\right)$, called the *Gamow factor*.

Nuclear reactions change the composition of stars and are the sources and sinks of energy that critically determine their evolution. Therefore, the rate at which they occur are a central component of their evolution. How often a projectile particle k will interact with a target j is quantified by the *nuclear cross section*. It is defined by the number of reactions per target per second rn_j, with the *reaction rate* r, and the flux of particles $n_k v$, where v is the relative velocity between the two species [Hix & Meyer 2006]:

$$\sigma = \frac{r/n_j}{n_k v} \tag{2.33}$$

In stellar plasmas the velocity of particles derives from their thermal energy, their distribution can be described by Maxwell-Boltzmann statistics. Therefore, the mean cross section between particles j and k is calculated from the integration of Maxwell-Boltzmann velocities. One writes

$$\langle \sigma v \rangle_{j,k} = \left(\frac{8}{\mu\pi}\right)^{1/2} (k_\mathrm{B}T)^{-3/2} \int_0^\infty E\sigma(E) \exp\left(-E/k_\mathrm{B}T\right) dE \tag{2.34}$$

where μ is the reduced mass of the target and projectile, E the center of mass energy, T the temperature and k_B is Boltzmann's constant. In a very general form, a nuclear reaction between two particles I and J is written as

$$\mathrm{I{+}J} \rightarrow \mathrm{K{+}L} \qquad \text{or} \qquad \mathrm{I(J,K)L}\ . \tag{2.35}$$

The particles on the left side of the arrow form the *entry channel*, those on the right the *exit channel*. Each type of reaction between two or more particles has its own unique cross section $\langle \sigma v \rangle_{I,J}$. The experimental determination of the reaction rates forms the basis of theoretical reaction network calculations (see Section 2.3).

The reaction cross sections determine the rate of reaction. How much energy is released depends on the nuclei components. The total mass of a nucleus M_N is less than the sum of the masses of the individual protons M_p and neutrons M_n, because a fraction of the mass-energy is contained in the bond. Thus, the *binding energy* is:

$$E_\mathrm{B} = \Delta E = (M_N - ZM_p - NM_n)c^2. \tag{2.36}$$

Conversely, E_B is the energy necessary to unbind the nucleus. Another useful quantity is the *binding energy per nucleon* E_b/A. For example, the nucleus ^{12}C has the binding energy $E_\mathrm{B} = 92.16\,\mathrm{MeV}$ and $E_\mathrm{B}/A = 7.68$

The difference of the total energy after and before a nuclear reaction is referred to as the Q-value. If Q is positive, the energy balance is positive, and energy was released. In this case, the reaction is called exothermic. On the other hand, if the Q-value is negative, energy was consumed and the reaction is called endothermic. In general, reactions between two nuclei I and J with mass numbers $\mathrm{A_I}$ and $\mathrm{A_J}$, and $\mathrm{A_I + A_J} < 56$, will be exothermic. When one of the resulting particles after an interaction is a photon, the reaction is called *radiative capture*. The intermediate state, after fusion, but before

evaporation, is called *compound nucleus*. For example, the radiative capture on ^{12}C is described by:

$$^{12}\mathrm{C} + p \rightarrow ^{13}\mathrm{N}^{*} \rightarrow ^{13}\mathrm{N} + \gamma, \tag{2.37}$$

which has $Q = 1.95\,\mathrm{MeV}$. These kind of reactions have in general positive Q-values and are therefore sources of energy for the star.

Non-explosive stellar hydrogen burning proceeds principally by two reaction sequences: the proton-proton (*pp*) chains and the carbon-nitrogen-oxygen (CNO) cycles. Both convert four protons into a ^{4}He nucleus, and release an energy that corresponds to the ^{4}He binding energy of $E_\mathrm{B} = 26.7\,\mathrm{MeV}$. However, the reaction paths they tread are quite distinct. The *pp* chains proceed by a sequence of hydrogen nuclei fusions, while in the CNO cycles, the C, N and O isotopes serve as catalysts to capture protons, decay, and in the last step eject a ^{4}He nucleus. The next two sections explain these processes.

2.2.2. The *pp* and *pep* chains

Here and in the following sections on nuclear processes, Wiescher et al. [2010] is our principal source.

Hydrogen is the most abundant element in the universe. It makes out the bulk of the chemical composition of star forming regions, therefore the composition of young stars is primarily hydrogen. The transmission coefficient depends on the charge of interacting nuclei as $\propto \exp\left(-Z_0 Z 1\right)$ (Equation (2.32)), hence the tunnel probability drops fast for heavy nuclei. Due to this fact and the predominance of light nuclei, primary fuel for nuclear reactions in hydrogen-rich matter at low temperatures (the core temperature of gravitationally contracting protostars is $T \approx 6 \times 10^6\,\mathrm{K}$) is the fusion of the light isotopes ^{1}He, ^{2}H and ^{3}He. The *pp* chain starts with proton-proton fusion, which creates deuterium ^{2}H under emission of a positron and an electron-neutrino ν. The first chain, PPI, is given by the following reactions:

$$^1\mathrm{H}(p,\beta^+\nu)^2\mathrm{H}(p,\gamma)^3\mathrm{He}(^3\mathrm{He},2p)^4\mathrm{He}. \tag{2.38}$$

There are alternative nuclear pathways that start with proton fusion and result in ^{4}He. After the proton capture on deuterium, a subsequent radiative capture with an α particle to form ^{7}Be leads to the PPII chain:

$$^1\mathrm{H}(p,\beta^+\nu)^2\mathrm{H}(p,\gamma)^3\mathrm{He}(\alpha,\gamma)^7\mathrm{Be}(\beta^-,\nu)^7\mathrm{Li}(p,\alpha)^4\mathrm{He}. \tag{2.39}$$

Alternatively, ^{7}Be can be destroyed by radiative capture, instead of beta decay, forming the PPIII chain:

$$^1\mathrm{H}(p,\beta^+\nu)^2\mathrm{H}(p,\gamma)^3\mathrm{He}(\alpha,\gamma)^7\mathrm{Be}(p,\gamma)^8\mathrm{B}(\beta^+\nu,\alpha)^4\mathrm{He}. \tag{2.40}$$

respectively. Independent of the reaction path, the total energy release is $Q = 26.73\,\mathrm{MeV}$, but the effective energy differs slightly in each case, due to different energy loss by neutrinos. Both PPII and PPIII chains require ^{4}He as a catalyst. This is provided either by the PPI chain of from the primordial abundance.

The total rate of energy generation of a sequence of different nuclear reactions, each with characteristic cross sections and reaction rates, is determined by the rate of the slowest reaction. Consider a species i, with mass fraction X_i, mass number A_i at density ρ. Let the reaction rate of the proton capture reaction be $\langle \sigma \upsilon \rangle_i$, and for radioactive species, the β-decay rate λ_β. Then the lifetime of the nucleus i is:

$$\tau_i = \frac{1}{\lambda_\beta + \rho \times X_i/A_i \times N_A \langle \sigma \upsilon \rangle_i}. \tag{2.41}$$

The total cycle time is the sum of the lifetimes of all involved nuclei, $\tau = \sum_i \tau_i$. Therefore, it will be determined the largest τ_i, owing to very long decay times (small λ_β) or very small reaction rates. In this case, it is the very first *pp* fusion, $^1\mathrm{H}(p, \beta^+\nu)^2\mathrm{H}$, because it involves the proton decay

$$p \rightarrow n + \beta^+ + \nu, \tag{2.42}$$

which is mediated by the weak interaction. Its much weaker strength with respect to the strong nuclear force means that the processes due to the weak interaction operate in much longer timescales. This is the reason behind the long periods that intermediate-mass stars can sustain hydrogen burning in the main sequence, for stars with $M = 1\,M_\odot$ this time can be $t \approx 10^{10}\,\mathrm{yr}$.

The so-called *pep* reaction supplements the first step of the *pp* chains:

$$p + e^- + p \rightarrow^2 \mathrm{H} + \nu. \tag{2.43}$$

In the Sun, the branching ratio for the *pep* reaction is only 0.4 % [Carroll & Ostlie 2007] and its contribution is negligible, except for the neutrino losses. However, in classical novae it can play an important role . The envelope densities can reach $\rho \sim 10^4\,\mathrm{g\,cm^{-3}}$, a value two orders of magnitude larger than that of the Sun's core. The increase in energy generation, compared to calculations that do not include the *pep* reaction is $\sim 40\,\%$ [Starrfield et al. 2007]. This has an effect on the envelope's evolution prior to the outburst, when most of the energy is produced by the *pp* chains. The increased energy release reduces the amount of accreted material, because the temperature rises faster per unit mass. As the envelope approaches the conditions for TNR, less mass has been accreted, the degree of degeneracy is lower, as well as the peak temperature at outburst [Starrfield et al. 2007, 2009].

2.2.3. The cold and hot CNO cycles

The *pp* are the primary sequences of hydrogen burning at ignition temperatures of hydrogen-rich matter. They have a relatively low Coulomb barrier and the energy release rates have a temperature dependence that goes as $\epsilon_{pp} \propto T^4$. Reactions with nuclei in the CNO range involve higher Coulomb barriers, so they need significantly higher temperatures to ignite, but the total rate of energy generation of the CNO cycles has a much steeper dependence on temperature $\epsilon_{\mathrm{CNO}} \propto T^{18}$ [Wiescher et al. 2010]. Therefore, in the initial stages of envelope mass accretion, the *pp* chains dominate the energy generation, but at runaway temperatures the CNO cycles process hydrogen much more efficiently. They are called *cycles*, because the last reaction in the sequence produces the nucleus for the entry channel of the first reaction, making a loop. Also,

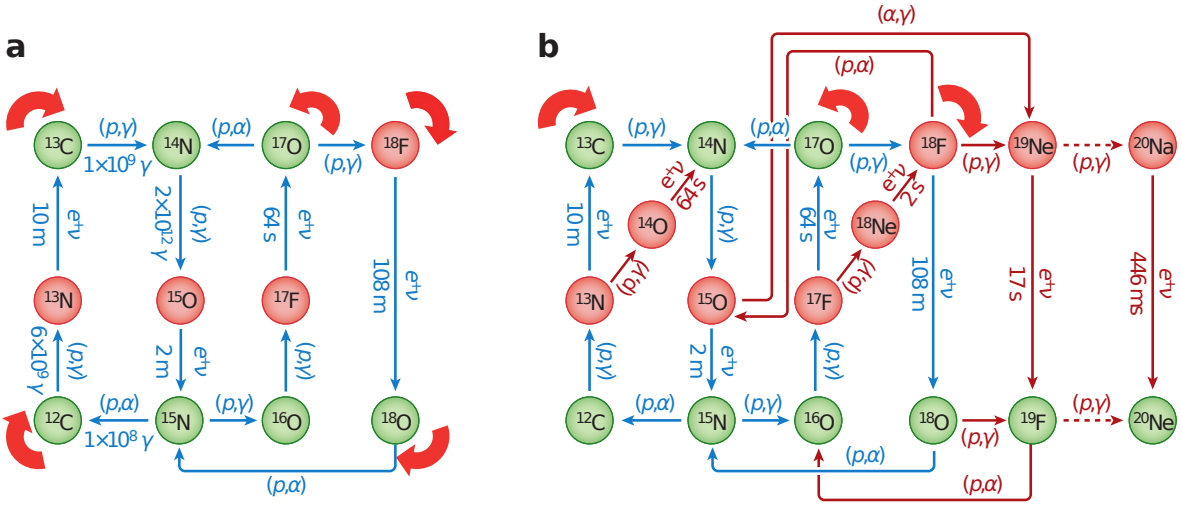

Figure 2.1.
Diagram of the cold (*a, blue arrows*) and hot (*b, red arrows*) CNO cycles. Figure adopted from Wiescher et al. [2010]

because under conditions below a critical temperature[1] the nuclear structure of the involved CNO isotopes prevents the reactions from breaking out into other reaction channels. Sometimes they are referred to in singular - cycle - or plural form - cycles. This is for two reasons. First, because the cycle is a set of four distinct "intertwined tetra-cycles"[2], and to distinguish from the *cold* and *hot* CNO cycles which, as the name suggests, operate on different temperatures.

Cold CN and NO cycles

Figure 2.1 shows a diagram of the reactions taking place in the CNO cycles. In Fig. (a), starting from the reaction $^{12}\mathrm{C}(p,\gamma)$ and following the arrows clockwise one identifies the CN cycle:

$$^{12}\mathrm{C}(p,\gamma)^{13}\mathrm{N}(\beta^{+}\nu)^{13}\mathrm{C}(p,\gamma)^{14}\mathrm{N}(p,\gamma)^{15}\mathrm{O}(\beta^{+}\nu)^{15}\mathrm{N}(p,\alpha)^{12}\mathrm{C}. \tag{2.44}$$

The chain starts with a radiative proton capture on ^{12}C, followed by a series of β^{+} decays and more radiative captures. The last reaction, $^{15}\mathrm{N}(p,\alpha)^{12}\mathrm{C}$ is the step where helium-4 is synthesized (the α particle). This reaction also be diverted to another nuclear path. Instead of ejecting an alpha particle to form ^{12}C and close the cycle, it can undergo radiative capture, $^{15}\mathrm{N} + p \rightarrow^{16}$ O$^{*} \rightarrow^{12}$ C $+ \alpha$. The excited compound nucleus decays to the ground state of ^{16}O via gamma-ray emission, allowing for a *breakout* into another channel, the NO cycle:

$$^{15}\mathrm{N}(p,\gamma)^{16}\mathrm{O}(p,\gamma)^{17}\mathrm{F}(\beta^{+}\nu)^{17}\mathrm{O}(p,\alpha)^{14}\mathrm{N}(p,\gamma)^{15}\mathrm{O}(\beta^{+}\nu)^{15}\mathrm{N} \tag{2.45}$$

However, the radiative capture happens in a ratio of (1 : 1000) compared to the α reaction. Due to the low branching ratio of the radiative capture, this cycle is powered mainly by the already present abundance of ^{16}O in the burning material.

[1] Breakout into the NeNa range occurs at $T \geq 0.4\,\mathrm{GK}$ [Wiescher et al. 2010].
[2] An expression borrowed also from Wiescher et al. [2010].

The NO cycle has also a branching point, occurring with the ^{17}O isotope: α-decay leads the chain back to ^{14}N and into the NO cycle, alternatively radiative capture opens a third branch:

$$^{17}\mathrm{O}(p,\gamma)^{18}\mathrm{F}(\beta^+\nu)^{18}\mathrm{O}(p,\alpha)^{15}\mathrm{N}(p,\gamma)^{16}\mathrm{O}(p,\gamma)^{17}\mathrm{F}(\beta^+\nu)^{17}\mathrm{O} \tag{2.46}$$

The strong interaction (p,α) reactions are generally stronger than the electromagnetic branch (p,γ). Also for the radiative capture on ^{17}O the cross section is three orders of magnitude weaker. For this reason, energy is mostly generated through the CN cycle. In any case, the total energy rate of a cycle is dependent on the slowest of the partaking reactions. In the CN cycle, it is the reaction $^{14}\mathrm{N}(p,\gamma)^{15}\mathrm{O}$. In the NO cycle, the cross section of the reaction $^{16}\mathrm{O}(p,\gamma)^{17}\mathrm{F}$ is very low and makes this the slowest process in the cycle.

The sum of these reaction chains can be written in compact form as

$$\begin{aligned} 4p + 2e^- &\rightarrow \alpha + 2e^+ + 2e^- + 2\nu_e + 3\gamma + 24.7\,\mathrm{MeV} \\ &\rightarrow \alpha + 2\nu_e + 3\gamma + 26.7\,\mathrm{MeV}. \end{aligned}$$

In the second step, the additional 2.04 MeV are the result of electron-positron annihilation, a process that releases gamma rays. Thus the energy released is the same as in the *pp* chain. However, the CN cycle has a much higher burning rate than the *pp* chain, which is slowed down by the $p + p \rightarrow d + e^+ + \nu$ reaction. We emphasize that these reaction cycles are a *hydrogen burning* process. Carbon, oxygen and nitrogen nuclei act as catalysts that capture four protons and result in a helium nucleus. Under the conditions found in stellar interiors and the early stages of novae, the cycles do not break out beyond the branching points already discussed, therefore the total initial mass fraction of CNO elements does not change through the nuclear reactions, it is merely divided among the participating species. A system in which many full cycles would run for timescales much longer than the cycle's total time would reach a state of equilibrium in which the abundances of the CNO elements and the energy generation would be constant.

Hot CNO cycles

We have seen that proton capture reaction rates rise drastically with temperature, hereby shortening the total time of one cycle. In the cold CN and NO cycles, the time is limited by the slowest reactions: the radiative captures on ^{14}N and ^{16}O. Radioactive beta decays, e.g. $^{13}\mathrm{N}(\beta^+,\nu)^{13}\mathrm{C}$, however, are not affected by temperature. Therefore, at temperatures nearing $T \sim 10^8\,\mathrm{K}$ (0.1 GK), beta decays become the slowest processes,

$$\lambda_\beta \leq \rho \frac{X}{A} N_A \langle \sigma v \rangle, \tag{2.47}$$

and those that determine the cycle time. The time scales of alternative proton capture reactions, such as $^{13}\mathrm{N}(p,\gamma)^{14}\mathrm{O}$ become shorter than the beta decay half-lives, listed in table Table 2.1. Of the competing branches

$$^{13}\mathrm{N}(\beta^+\nu)^{13}\mathrm{C} \qquad \text{vs.} \qquad ^{13}\mathrm{N}(p,\gamma)^{14}\mathrm{O}$$

Species	Half life $\tau_{1/2}$ (s)
^{13}N	598
^{14}O	71
^{15}O	122
^{17}F	65

Table 2.1.
Half lives of the radioactive nuclei in the CNO cycles.

the latter becomes the shortest option, and energy generation ensues along the hot CNO (HCNO) cycle. This is shown in Panel (*b*) of Figure 2.1. This cycle is also referred to as 'beta-limited', due to the fact that in the 'hot' case the half-lives of the β^+-unstable nuclei delay the succession of nuclear events and characterize the nucleosynthesis. The hot CN cycle becomes:

$$^{12}\mathrm{C}(p,\gamma)^{13}\mathrm{N}(p,\gamma)^{14}\mathrm{O}(\beta^+\nu)^{14}\mathrm{N}(p,\gamma)^{15}\mathrm{O}(\beta^+\nu)^{15}\mathrm{N}(p,\alpha)^{12}\mathrm{C}. \tag{2.48}$$

The cycle time of $\tau \approx 200\,\mathrm{s}$ is determined by the decay of ^{14}O and ^{15}O, which are called *waiting points*. Due to their independence from temperature, the energy generation rate is constant

$$\epsilon_{\mathrm{CNO}} \approx 4.6 \times 10^{15} \times Z_{\mathrm{CNO}}\,\mathrm{erg\ g^{-1}s^{-1}}. \tag{2.49}$$

Precisely the isotopes of the waiting points, ^{14}O and ^{15}O, will be substantially enriched.

The cold NO cycle also has its hot counterpart, $^{16}\mathrm{O}(p,\gamma)\ ^{17}\mathrm{F}(p,\gamma)\ ^{18}\mathrm{Ne}(\beta^+\nu)\ ^{18}\mathrm{F}(p,\alpha)\ ^{15}\mathrm{O}(\beta^+\nu)\ ^{15}\mathrm{N}(p,\gamma)\ ^{16}\mathrm{O}$ with waiting points at ^{15}O and ^{18}Ne. $^{18}\mathrm{F}(p,\gamma)\ ^{19}\mathrm{Ne}(\beta^+\nu)\ ^{19}\mathrm{F}(p,\alpha)\ ^{16}\mathrm{O}(p,\gamma)\ ^{17}\mathrm{F}(p,\gamma)\ ^{18}\mathrm{Ne}(\beta^+\nu)\ ^{18}\mathrm{F}$. However, we will see that at the temperatures achieved in our simulations, only the hot CN cycle is available.

2.3. Nuclear reaction networks

Nuclear reactions create and destroy particles, changing the elemental abundances in the plasma. Their rates depend on the (number) density of the corresponding species in the gas. Reaction rates depend also on temperature, and are themselves sinks are sources of energy, which alter the pressure and temperature of the gas, causing hydrodynamic motions. Therefore, nuclear reactions must be coupled in some manner to the hydrodynamic equations.

In stellar applications, interactions between up to three particles are relevant. Single-particle reactions, including beta-decays, depend only on the number density of one species. Two particle reactions, like proton- and alpha-captures, depend on the number density of both species. The triple-alpha process, ^{4}He $+^4$ He $+^4$ He $\rightarrow^{12}$ C, is an example of a three-particle reaction, but its rate depends on the number density of only one species: ^{4}He. The change in number density n_i of species i, due to all reactions involving i, can be written by grouping the reactions rates r into those three

categories, namely:

$$\left.\frac{\partial n_i}{\partial t}\right|_{\rho=\text{const}} = \sum_j \mathcal{N}^i_j r_j + \sum_{j,k} \mathcal{N}^i_{j,k} r_{j,k} + \sum_{j,k,l} \mathcal{N}^i_{j,k,l} r_{j,k,l}. \tag{2.50}$$

Because the species i appears also in the rate equations of other species j, the rates should not be counted doubly. The numbers $\mathcal{N}$ account for the correct counting. The expressions read:

$$\begin{aligned} \mathcal{N}^i_j &= N_i \\ \mathcal{N}^i_{j,k} &= N_i / \prod_{m=1}^{n_{j,k}} (|N_m|!) \\ \mathcal{N}^i_{j,k,l} &= N_i / \prod_{m=1}^{n_{j,k,l}} (|N_m|!), \end{aligned} \tag{2.51}$$

where the N_i can also be negative numbers if the species is destroyed in the reaction.

However, the number density can also change due to hydrodynamical motions. In order to have an expression that only due to the nuclear reactions, the equations are written instead in terms of the nuclear abundance:

$$Y_i = \frac{n_i}{\rho N_\text{A}}, \tag{2.52}$$

where N_A is Avogadro's number. For a nucleus with atomic weight A_i, the mass fraction is $X_i = A_i Y_i$, and the total mass fraction is one: $\sum_i A_i Y_i = 1$. Equation (2.50), rewritten in terms of Y_i, reads:

$$\dot{Y}_i = \sum_j \mathcal{N}^i_j \lambda_j Y_j + \sum_{j,k} \rho N_\text{A} \mathcal{N}^i_{j,k} \lambda_{j,k} Y_j Y_k + \sum_{j,k,l} (\rho N_\text{A})^2 \mathcal{N}^i_{j,k,l} \lambda_{j,k,l} Y_j Y_k Y_l, \tag{2.53}$$

where the definition of the reaction cross sections (Equations (2.33) and (2.34)) were inserted. For all species i in the network, Equation (2.53) is a set of first order ordinary differential equations for the evolution of Y_i depending only on the nuclear reaction rates.

The energy release from nuclear reactions is due to the binding energy of the nuclei, Equation (2.36). The total nuclear energy release rate, from all Y_i, is therefore:

$$\dot{\epsilon}_\text{nuc} = -\sum_i N_\text{A} M_i c^2 \dot{Y}_i \qquad [\text{MeV g}^{-1}\,\text{s}^{-1}] \tag{2.54}$$

For the coupling to the hydro equations, only the total energy release rate is of importance, Equation (2.54). However, for our detailed analysis of nucleosynthesis in the envelope, we are interested in the contributions from individual interaction of the CNO cycle to the TNR. Therefore, we use use another expression for the nuclear energy rate, presented in the Results chapter, Section 5.2.

In *SLH*, the numerical solution to the rate equations is performed with the code *YANN* [Pakmor et al. 2012], using the implicit integration method of Bader & Deuflhard [1983]. The coupling to hydrodynamics is done using the Godunov operator splitting method. First, a normal hydrodynamics step is performed (Section 3.1.3). Then, the thermodynamic variables of the new state are used to solve the nuclear reaction network in every grid cell. The resulting energy release and composition define the new state are used to update the state, which is the initial data for the next hydrodynamics step (see Edelmann [2014, Section 2.5.3] for more details).

3. Description of the code

3.1. Multidimensional hydrodynamic simulations

The stellar evolution equations described in the last chapter make the assumption of perfect spherical symmetry, reducing the three spatial dimensions to only one radial coordinate. To account for multi-dimensional processes like convection, approximations such as the mixing length theory, Section 2.1.3, must be included. But to be able to fully account for the effects of these processes, three-dimensional hydrodynamics equations are needed. Stellar environments can be appropriately described as fluids in the continuum approximation, because the mean free path of the nuclei and particles that compose it is orders of magnitude smaller than the dynamical length scale. Then, the fluid can be described by its thermodynamical variables and velocity field. Any fluid volume must fulfill the conservation of mass, momentum and energy. These are expressed as a set of conservation laws, its mathematical formalism known as the Navier-Stokes equations. The presentation of this chapter is inspired by the layout in Edelmann [2014], and is but a short summary of the methods implemented in the code. A detailed account can be found in Edelmann [2014], Miczek [2013] and Miczek et al. [2015].

3.1.1. Euler equations

Conservation laws are *continuity equations* for the conserved quantities of the flow. In a general case, a continuity equation in differential form can be written as:

$$\frac{dU}{dt} + \nabla \cdot f(U) = 0. \tag{3.1}$$

where U is the conserved quantity and $f(U)$ its flux function. Integrating this equation over any volume V with surface ∂V and using Gauss's theorem yields

$$\frac{d}{dt}\int_V U dV + \int_{\partial V} f(U) \cdot \boldsymbol{n} dS = 0. \tag{3.2}$$

The integral manifests that U changes inside V only because of the fluxes at its boundary. If the right hand side of the equation is non-zero, those terms are called *source terms*. They can include effects that influence U regardless of the boundaries, such as gravity, chemical or nuclear reactions.

The equations of fluid dynamics are a system of conservation laws, commonly expressed in terms of the variables $\boldsymbol{U}$:

$$\boldsymbol{U} = (\rho, \rho u, \rho v, \rho w, \rho E, \rho X_i)^T \tag{3.3}$$

where ρ is the density, $\rho u, \rho v, \rho w$ the three components of momentum and ρE is the total energy (internal and kinetic) per volume. In the last expression, X_i stands for any other scalar value advected with the flow. In the framework of stellar simulations X_i

is the mass fraction of the nuclear species i, and the vector $\boldsymbol{U}$ has n_{sp} components X_i, one for each of the n_{sp} species considered. The fully viscous Navier-Stokes equations can be concisely written as [Toro 2009]:

$$\partial_t \boldsymbol{U} + \partial_x \boldsymbol{F}(\boldsymbol{U}) + \partial_y \boldsymbol{G}(\boldsymbol{U}) + \partial_z \boldsymbol{H}(\boldsymbol{U}) = \partial_x \boldsymbol{F}^d + \partial_y \boldsymbol{G}^d + \partial_z \boldsymbol{H}^d + \boldsymbol{S} \quad (3.4)$$

where $\boldsymbol{F}$, $\boldsymbol{G}$ and $\boldsymbol{H}$ are the flux functions, $\boldsymbol{F}^d$, $\boldsymbol{G}^d$ and $\boldsymbol{H}^d$ the diffusive terms and $\boldsymbol{S}$ the source terms. The diffusive terms include terms of the viscous stress tensor τ. Contrary to many engineering applications, stellar matter is commonly assumed to be inviscid. A quantity commonly used to estimate the importance of viscosity is the Reynolds number Re, which is the ratio of inertial to viscous forces:

$$\mathrm{Re} = \frac{\rho\, u L}{\eta}. \quad (3.5)$$

For $\mathrm{Re} \simeq 1 - 100$, viscous effect dominate the flow. In flows with very high Reynolds numbers viscosity can be neglected, the flow is said to be in the *turbulent regime*. For instance, with values typical of the Sun's radiative zone the Reynolds number is $\mathrm{Re} = 3 \times 10^{12}$ [Edelmann 2014]. At the convective boundary of white dwarf novae progenitors the corresponding values are typically $\rho = 10^3\,\mathrm{g\,cm^{-3}}$, $u = 10^7\,\mathrm{cm\,s^{-1}}$, $L \sim H_p = 3 \times 10^7\,\mathrm{cm}$. Assuming a value for the viscosity of ionized gases $\eta = 1\,\mathrm{g\,cm^{-1}\,s^{-1}}$ [Kippenhahn et al. 2013, Sec. 45.1] we get an estimated $\mathrm{Re} = 3 \times 10^7$. Therefore the flow in our simulations of novae will be in the turbulent regime. Any kind of spatial discretization introduces numerical diffusivity that is generally orders of magnitude larger than the physical viscosity, so that including viscous terms does not represent an improvement of the scheme. Indeed, the motivation for the *SLH* was the implementation of a hydro code whose numerical fluxes *reduced* the diffusivity typical of low Mach number flows[1]. Dropping the stress tensor from the Navier–Stokes equations results in the Euler equations of gas dynamics:

$$\partial_t \boldsymbol{U} + \partial_x \boldsymbol{F} + \partial_y \boldsymbol{G} + \partial_z \boldsymbol{H} = \boldsymbol{S}, \quad (3.6)$$

[1] Viscous terms can in fact be optionally included in *SLH*, but are generally switched off. They were included to test if the viscosity helped control the exponential growth of the checkerboard instability discussed in Section 3.3.1.

with the fluxes

$$\boldsymbol{F} = \begin{pmatrix} \rho u \\ \rho u^2 + p \\ \rho uv \\ \rho uw \\ u(\rho E + p) - K\partial_x T \\ \rho u X_i \end{pmatrix}, \qquad \boldsymbol{G} = \begin{pmatrix} \rho v \\ \rho uv \\ \rho v^2 + p \\ \rho vw \\ v(\rho E + p) - K\partial_y T \\ \rho v X_i \end{pmatrix},$$
$$\boldsymbol{H} = \begin{pmatrix} \rho w \\ \rho uw \\ \rho vw \\ \rho w^2 + p \\ w(\rho E + p) - K\partial_z T \\ \rho w X_i \end{pmatrix} \tag{3.7}$$

and source terms

$$\boldsymbol{S} = \begin{pmatrix} 0 \\ \rho g_x \\ \rho g_y \\ \rho g_z \\ \rho \boldsymbol{u} \cdot \boldsymbol{g} + \rho \sum_i e_{\mathrm{nuc},i} \dot{X}_i \\ \rho \dot{X}_i \end{pmatrix}. \tag{3.8}$$

Equation (3.6) is the system of partial differential equations that *SLH* solves to model stellar regions.

The energy equation includes thermal radiation. If the mean free path of the photons is small compared to the length scales of thermal fluctuations, the gas is said to be in local thermodynamic equilibrium. In this case, the thermal conductivity

$$K = \frac{4acT^3}{e\rho\kappa} \tag{3.9}$$

has a source function of the form

$$S_{\mathrm{rad}} = \nabla \cdot (K \nabla T), \tag{3.10}$$

where a is the radiation density constant and κ the opacity. Equation (3.10) can be viewed as the divergence of the radiative flux, so in this description it is added directly to the flux functions. Heat conduction follows an equation of the same form as Equation (3.10), only the definition of the conductivity is different. Therefore both can be included in the same term. It should be noted that radiation in the diffusion limit holds only when the matter is optically think, i.e. it has a large opacity κ. In regions with lower opacities the mean free path of photons is large and radiation cannot be approximated as a diffusive process anymore.

The source terms include the gravitational acceleration $\boldsymbol{g}$. In principle, the gravitational force acting on any cell depends on a whole density distribution ρ, inside and outside of the computational domain. The gravitational potential ϕ is a solution of Poisson's equation $\nabla^2\phi = 4\pi G\rho$, and the gravitational acceleration $\boldsymbol{g}$ its gradient

$$\boldsymbol{g} = -\nabla\phi. \tag{3.11}$$

At the time of writing, gravity is included only as a temporally constant term, independently of any gravitational potential.[2] In our simulations of convective boundaries at the surface of white dwarfs we adopt a point-source acceleration from the core of the star, which is outside of the computational domain.

Lastly, the energy equation also includes the nuclear energy release $e_{\mathrm{nuc},i}$, discussed in detail in Section 2.2.1.

Equation of state

The thermodynamic variables ρ, T, p and e are connected by a relation called the *equation of state* (EoS). The simplest kind is the ideal gas, in which the particles are assumed to interact frictionless and scatter elastically. It is defined by the equations:

$$p_{\mathrm{ideal}} = \rho R_{\mathrm{gas}} \frac{T}{\mu}, \quad e_{\mathrm{ideal}} = \frac{1}{\gamma - 1} R_{\mathrm{gas}} \frac{T}{\mu}. \tag{3.12}$$

There R_{gas} is the universal gas constant and μ the mean molecular weight. Several mono-atomic gases on Earth can be described by ideal gases with good approximation. For mono-atomic gases γ is 5/3. In the high-temperature environment of stellar interiors the energy is much larger than the molecular dissociation energy, so that the existence of molecules can be ruled out and the gas can be treated as mono-atomic.

Stellar matter is subject to very different and extreme conditions that depart from the idealization of Equation (3.12). An immense amount of energy is carried by the photons liberated from thermonuclear reactions, so that the radiation field contributes significantly to the energy and pressure. A correct treatment of the energy conduction by photons would require the equations of radiative transfer. However, in regions of high opacity κ, i.e a small mean free path, radiation can be treated as a diffusive process. In this limit, the terms for radiation pressure simplify and the equation of state becomes:

$$\begin{aligned} p(\rho, T, X) &= \frac{\rho R T}{\mu} + \frac{4\sigma T^4}{3c} \\ e(\rho, T, X) &= \frac{\rho R T}{(\gamma - 1)\mu} + \frac{4\sigma T^4}{c}, \end{aligned} \tag{3.13}$$

where σ is the Stefan-Boltzmann constant.

A more accurate equation of state can be constructed by adding subsequent terms to the energy and pressure [Timmes & Arnett 1999]:

$$p_{\mathrm{tot}} = p_{\mathrm{rad}} + p_{\mathrm{ion}} + p_{\mathrm{ele}} + p_{\mathrm{pos}} \tag{3.14}$$

$$e_{\mathrm{tot}} = e_{\mathrm{rad}} + e_{\mathrm{ion}} + e_{\mathrm{ele}} + e_{\mathrm{pos}}. \tag{3.15}$$

[2] The implementation of a multigrid gravity-solver is currently being carried out by Aron Michel.

Which terms are relevant, depends on the stellar region that is being modeled. Full ionization is true of stellar interiors. In high energy regions the contribution of electron-positron pair creation must be considered. Electron degeneracy pressure is a defining property of white dwarfs.

The pressure in Equation (3.15) cannot be expressed in terms of the conservative variables analytically. If however the conservative variables ρ and ρE are given, the temperature can be iterated numerically with the Newton-Raphson method. The temperature from the ideal gas Equation (3.12) is used as the initial guess for the iteration. The use of tabulated equations of state is widespread, because for multi-dimensional simulations the interpolation from tabulated values is often less costly than direct calculation. The EoS chosen for SLH is the so-called *Helmholtz EoS* of Timmes & Swesty [2000]. Here, the interpolation is performed in the Helmholtz free energy and its derivatives:

$$F = E - TS, \qquad dF = -SdT + \frac{P}{\rho^2} d\rho \tag{3.16}$$

The remaining thermodynamic variables are calculated from the derivatives of F. This method guarantees that the EoS remains thermodynamically consistent, i.e. that the Maxwell relations are always satisfied regardless of the interpolation.

In stellar interiors at temperatures above 10^7 K, one can assume full ionization. Then, the mean molecular weight from all species X_i, each with molecular weight M_i and charge number Z_i, can be written as

$$\mu = \left(\sum_i (1 + Z_i) \frac{X_i}{M_i} \right)^{-1}. \tag{3.17}$$

The temporal evolution of each of the species in the system is calculated in a nuclear reaction network (Section 2.3).

3.1.2. Finite-volume schemes

To show the conservative character of the Euler equations, Equation (3.6), we can write them in the integral form analogous to Equation (3.2). For simplicity, let us assume a Cartesian geometry and define a grid of discrete cells, indexed with integer values i for to indicate their centers and half-valued indices for the cell faces. Then the integral over the control volume $\Omega_{i,j,k}$, defined by the boundaries $[x_{i-1/2}, x_{i+1/2}]$, $[y_{j-1/2}, y_{j+1/2}]$, and $[z_{k-1/2}, z_{k+1/2}]$ yields:

$$\partial_t \boldsymbol{U}_{i,j,k} + {V_{i,j,k}}^{-1} \left(\int_{\Omega_{i,j,k}} \partial_x \boldsymbol{F} + \int_{\Omega_{i,j,k}} \partial_y \boldsymbol{G} + \int_{\Omega_{i,j,k}} \partial_z \boldsymbol{H} \right) = \boldsymbol{S}_{i,j,k}, \tag{3.18}$$

which introduces the cell-averages quantities

$$\boldsymbol{U}_{i,j,k} = \frac{1}{V_{i,j,k}} \int_{\Omega_{i,j,k}} U d\Omega_{i,j,k}, \qquad \boldsymbol{S}_{i,j,k} = \frac{1}{V_{i,j,k}} \int_{\Omega_{i,j,k}} S d\Omega_{i,j,k}. \tag{3.19}$$

Interchanging the integral and derivative operators is legitimate when starting from the strong form of the differential equation. Invoking again Gauss's theorem, the

volume integrals can be rewritten as integrals over the surface, and the finite volume discretization of the Euler equations becomes:

$$\begin{aligned}\partial_t \boldsymbol{U}_{i,j,k} + {V_{i,j,k}}^{-1}(&\boldsymbol{F}_{i+1/2,j,k} - \boldsymbol{F}_{i-1/2,j,k} \\ &+\boldsymbol{G}_{i,j+1/2,k} - \boldsymbol{G}_{i,j-1/2,k} \\ &+\boldsymbol{H}_{i,j,k+1/2} - \boldsymbol{H}_{i,j,k-1/2}) = \boldsymbol{S}_{i,j,k}.\end{aligned} \tag{3.20}$$

From this form, the conservative character of the method is also evident, i.e. that the variables $\boldsymbol{U}_{i,j,k}$ of a volume (cell) change only due to the fluxes at the boundaries or the cell-averaged source terms $\boldsymbol{S}_{i,j,k}$. Therefore, the information stored after each iteration are the cell-averaged values. Equation (3.20) expresses the time evolution of a single cell (i, j, k), but its conservative nature extends to the whole computational domain. The flux across the boundary between two neighboring cells is the same and cancels out when integrating over the whole domain – the values $\boldsymbol{U}$ are conserved except for source terms and for fluxes *at the boundaries of the domain.*

So far we have not specified how the fluxes are calculated from the cell's values. The specific form of the flux functions is what distinguishes the many different existing numerical schemes to solve the Euler equations. A category of schemes is based on the solution of the *Riemann problem* at the boundary between two cells, with piecewise constant left and right states $\boldsymbol{U}_\mathrm{L}$ and $\boldsymbol{U}_\mathrm{R}$. For a general $m \times m$ non-linear hyperbolic system, the initial-value problem is defined by [Toro 2009]:

$$\begin{aligned}&\boldsymbol{U}_t + \boldsymbol{F}(\boldsymbol{U})_x = \boldsymbol{0} \\ &\boldsymbol{U}(x,0) = \begin{cases}\boldsymbol{U}_\mathrm{L} & \text{for } x < 0, \\ \boldsymbol{U}_\mathrm{R} & \text{for } x > 0.\end{cases}\end{aligned} \tag{3.21}$$

In the above equation, $\boldsymbol{F}$ is the flux function. The solution consists of $m+1$ constant states separated by m waves. The waves correspond to the eigenvalues of the system. In non-linear systems such as the Euler equations, the waves can not only be smooth (advection, rarefaction) but also discontinuous (shock, contact). The solutions of the Riemann problem can be used in so-called Reconstruct-Solve-Average schemes (RSA), three-step algorithms to discretize hydrodynamical systems and evolve them in time. We have already described the first step, namely to define cell-averaged quantities as in Equation (3.19), written for the nth time step $\boldsymbol{U}^n$. In the second step, the reconstructed states are evolved in time by a discrete step Δt. The last step is to take the evolved solution from the previous time step and average them to define the new states $\boldsymbol{U}^{n+1}$.

The solution to the Riemann problem at position x and time step $t+1$ can be written as [Toro 2009]:

$$\boldsymbol{U}_i^{n+1} = \frac{1}{\Delta x_i}\int_0^{\Delta x_i/2} \boldsymbol{U}_{i-1/2}\left(\frac{x}{\Delta t}\right) dx + \frac{1}{\Delta x_i}\int_{-\Delta x_i/2}^{0} \boldsymbol{U}_{i+1/2}\left(\frac{x}{\Delta t}\right) dx. \tag{3.22}$$

where $\boldsymbol{U}_{i-1/2}(x/\Delta t)$ is the solution to the Riemann problem at the interface $i-1$ and Δx_i is the width of cell i. By using the conservation property of the Euler equations, the expression can be simplified to:

$$\boldsymbol{U}^{n+1} = \boldsymbol{U}^n + \frac{\Delta t}{\Delta x}\left(\boldsymbol{F}_{i-1/2} - \boldsymbol{F}_{i+1/2}\right), \tag{3.23}$$

where the need to integrate over the cells has been removed. At this point, the Riemann problem needs to be solved, either exactly or by some approximation. The most widespread *approximate Riemann solver* is that of Roe [1981]:

$$\boldsymbol{F}_{1/2} = \frac{1}{2}\left(\boldsymbol{F}(\boldsymbol{U}_L) + \boldsymbol{F}(\boldsymbol{U}_R) - |A_{\text{roe}}|(\boldsymbol{U}_R - \boldsymbol{U}_L)\right), \tag{3.24}$$

where A_{roe} is the Jacobian matrix of the flux function $\boldsymbol{F}$. It is called approximate because in this method, the Riemann problem that is solved is a simplified version of the original Equation (3.21). In the original PDE, which can be written as

$$\boldsymbol{U}_t + \boldsymbol{A}(\boldsymbol{U})\boldsymbol{U}_x = \boldsymbol{0}, \tag{3.25}$$

the Jacobian matrix $\boldsymbol{A}(\boldsymbol{U})$ is replaced by a constant Jacobian matrix $\tilde{\boldsymbol{A}} = \tilde{\boldsymbol{A}}(\boldsymbol{U}_L, \boldsymbol{U}_R)$. The approximate Riemann problem then reads:

$$\begin{aligned} \boldsymbol{U}_t + \tilde{\boldsymbol{A}}\boldsymbol{U}_x &= \boldsymbol{0} \\ \boldsymbol{U}(x,0) &= \begin{cases} \boldsymbol{U}_{\text{L}} & \text{for } x < 0, \\ \boldsymbol{U}_{\text{R}} & \text{for } x > 0, \end{cases} \end{aligned} \tag{3.26}$$

which is a linear system with constant coefficients. This system is then solved *exactly*. A detailed explanation can be found in Toro [2009, Chapter 11]. In *SLH*, a variation of this scheme is used, modified to treat low Mach numbers.

3.1.3. Time-stepping

The numerical scheme as presented in last section by Equation (3.20), can be rewritten in a semi-discrete ordinary differential equation:

$$\frac{\partial \boldsymbol{U}_{i,j,k}}{\partial t} + \boldsymbol{R}_{i,j,k}(\boldsymbol{U}) = 0. \tag{3.27}$$

Here, $\boldsymbol{R}_{i,j,k}$ is called the spatial residual. In general, it may depend on the conservative variables in all other grid cells. For this reason, $\boldsymbol{U}$ is written without any indices. This representation is *semi-discrete*, i.e. the discretization has been done only in space, but not in time. Separating the spatial and temporal derivatives in a form such as Equation (3.27) is called the *method of lines*. The separation allows for great flexibility, as the time-marching scheme can be chosen independently from the hydrodynamic scheme.

The time-evolution of the flow variables, the cell-averaged $\boldsymbol{U}_{i,j,k}$, is usually approximated by discrete time steps $\boldsymbol{U}^n_{i,j,k}$, as in Equation (3.23). The method by which a step $\boldsymbol{U}^{n+1}_{i,j,k}$ is calculated from the previous one can be *explicit* or *implicit*. A method is called explicit, if the calculation of the new quantities can be done directly from the known quantities of the previous step. If instead the scheme does not permit an analytic expression for the next time step, the new quantities are defined by a coupled system of equations that need to be solved iteratively. Such are called implicit methods.

In practice, the choice of explicit or implicit schemes is often decided on the expected flow properties. A necessary condition for the convergence of numerical schemes for

partial differential equations (PDE) is the Courant-Friedrichs-Lewy (CLF) condition [Courant et al. 1928] (the difference between explicit and implicit schemes is explained in the next section). It states that the true domain of dependence of the PDE must be contained within the domain of dependence of the numerical scheme. In other words, the CFL condition ensures that the length of the time step Δt is not longer than the time it takes information to travel from one grid cell to the next. It is limited by the maximum signal speed $S^n_{\max}$ in the system:

$$\Delta t \leq \frac{\Delta x}{S^n_{\max}}. \tag{3.28}$$

The index n in the speed denotes an iteration step, i.e. the size of the time step Δt is not fix and is adjusted after each iteration. The exact determination of the largest signal speed, in the case of the Euler equations, depends on the local solutions to the Riemann problem. Instead, a simplified constraint for the time step is the *acoustic* CLF condition

$$\Delta t \leq \mathrm{CFL}_{uc} \min_{q \in \{u,v,w\}} \frac{\Delta x}{|q| + c}, \tag{3.29}$$

whereby the time step is limited by the speed of sound waves traveling at speeds $|q| + c$. The minimum function has to be applied to all coordinate directions. The dimensionless number CFL_{uc} represents the number of grid cells that a sound wave can traverse in a single time step, whose upper limit is of order one.

Explicit time-stepping

A simple way to discretize Equation (3.27) is to replace the time derivative with a simple finite difference, and to evaluate the residual at the previous time step:

$$\frac{\boldsymbol{U}^{n+1}_{i,j,k} - \boldsymbol{U}^{n}_{i,j,k}}{\Delta t} + \boldsymbol{R}_{i,j,k}(\boldsymbol{U^n}) = 0. \tag{3.30}$$

In this form we can explicitly solve for the state of the new time step $\boldsymbol{U}^n_{i,j,k}$. This method of discretization, called the forward Euler method, is first-order accurate in time. The order of accuracy is the power with which the discretization error scales, in this case $\propto \Delta t^1$. Usually methods of second-order accuracy or higher are preferred.

In *SLH* the explicit Runge-Kutta methods [Shu & Osher 1988] are implemented. Here, the solution of the next time step is performed in three steps:

$$\begin{aligned}
\boldsymbol{U}^{(1)}_{i,j,k} &= \boldsymbol{U}^{(1)}_{i,j,k} - \Delta t\, \boldsymbol{R}_{i,j,k}(\boldsymbol{U}^n) \\
\boldsymbol{U}^{(2)}_{i,j,k} &= \frac{3}{4}\boldsymbol{U}^{n}_{i,j,k} + \frac{1}{4}\boldsymbol{U}^{(1)}_{i,j,k} - \frac{1}{4}\Delta t\, \boldsymbol{R}_{i,j,k}\left(\boldsymbol{U}^{(1)}\right) \\
\boldsymbol{U}^{n+1}_{i,j,k} &= \frac{1}{3}\boldsymbol{U}^{n}_{i,j,k} + \frac{2}{3}\boldsymbol{U}^{(2)}_{i,j,k} - \frac{2}{3}\Delta t\, \boldsymbol{R}_{i,j,k}\left(\boldsymbol{U}^{(2)}\right)
\end{aligned} \tag{3.31}$$

It is commonly called RK3 because of its third-order accuracy. Another desirable property of the scheme is that it fulfills the total variation diminishing (TVD) property.

Explicit methods are generally easy to implement and consume low resources per time step. Their drawback lies on the limitation of the time step size Δt, which is

strictly constrained by the CFL condition. Violating the CFL criterion makes the scheme unstable and makes the numerical solution quickly depart from the true solution. For simulations of low Mach number flows,

$$\mathrm{Ma} = \frac{|q|}{c_\mathrm{s}}, \tag{3.32}$$

where $|q|$ is the fluid velocity. This constrain becomes particularly restrictive. There, the fluid motions of interest are per definition much smaller than the sound speed c_s, which is the fastest signal in the system, yet resolving sound waves is not important. The step sizes Δt resulting from the CFL criterion become very small, so that many iterations are needed to traverse even short time scales.

Implicit time-stepping

If we consider the semi-discrete Equation (3.27) and apply the same finite difference approximation to the time derivative as before, but evaluate the spatial residual in the new time step $n+1$ we obtain:

$$\frac{\boldsymbol{U}^{n+1}_{i,j,k} - \boldsymbol{U}^{n}_{i,j,k}}{\Delta t} + \boldsymbol{R}_{i,j,k}(\boldsymbol{U^{n+1}}) = 0. \tag{3.33}$$

Generally, this equation cannot be solved directly for $\boldsymbol{U}^{n+1}_{i,j,k}$, since it is also contained in the residual. This means that the numerical domain of dependence of one cell has expanded from just its neighboring cells – as in the explicit methods – to the whole numerical grid. This is because the new values of one cell (i,j,k) depend also on the *new* values of its the neighbors, and hence this dependence propagates to the entire domain. Consequently, the size of the time step is not limited by the fastest wave from one cell reaching its neighboring cells (the CFL condition).

The liberty from the strict CFL condition comes at a cost. It is generally not possible to analytically invert the residual in Equation (3.33). Therefore, numerical methods are necessary to solve this expression. This implies that one or more non-linear equations need to be solved. To this end, Equation (3.33) is rewritten in the standardized form suitable for numerical solvers:

$$\boldsymbol{D}_{i,j,k}(\boldsymbol{U}^{n+1}) = \boldsymbol{R}_{i,j,k}(\boldsymbol{U}^{n+1}) + c_t \boldsymbol{U}^{n+1}_{i,j,k} + \boldsymbol{C}_{i,j,k} = 0. \tag{3.34}$$

Here, $\boldsymbol{D}$ is called the defect, and must equal zero in all grid cells. For the backward Euler method, Equation (3.33), the constants c_t and $\boldsymbol{C}_{i,j,k}$ take the values $c_t = 1/\Delta t$ and $\boldsymbol{C}_{i,j,k} = -1/\Delta t^n_{i,j,k}$. However, this method is only first order in time.

Higher order methods can be constructed via a generalized Runge-Kutta scheme with a number of s stages, which can be written as:

$$\begin{aligned} \boldsymbol{U}^{(q)}_{i,j,k} &= \Delta t\, \boldsymbol{R}\left(\boldsymbol{U}^n + \sum_{l=1}^{s} a_{ql}\boldsymbol{U}^{(l)}, t^n + c_q \Delta t\right), \\ \boldsymbol{U}^{n+1}_{i,j,k} &= \sum_{l=1}^{s} b_l \boldsymbol{U}^{(l)}_{i,j,k}. \end{aligned} \tag{3.35}$$

Each intermediate step $\boldsymbol{U}^{(q)}$ has the coefficients a ($s \times s$ matrix), b (row vector of size s) and c (column vector of size s), all of which can be visualized in a so-called Butcher-tableau:

$$\begin{array}{c|cccc} c_1 & a_{11} & a_{12} & \cdots & a_{1s} \\ c_2 & a_{21} & a_{22} & \cdots & a_{2s} \\ \vdots & \vdots & \vdots & \ddots & \vdots \\ c_s & a_{s1} & a_{s2} & \cdots & a_{ss} \\ \hline & b_1 & b_2 & \cdots & b_s \end{array} . \tag{3.36}$$

If the a_{ql} form a lower diagonal matrix (the values on the diagonal and upper right half are zero) then the explicit case is recovered, and the system can be solved by s successive evaluations of $\boldsymbol{R}$, without the need to solve any non-linear equations.

In the general case where a is a full matrix, all the intermediate steps $\boldsymbol{U}^{(q)}$ are implicitly coupled. This means that a large non-linear system must be solved, and not only for one set of conservative values, but for s sets. This requires a high computational cost, as a large Jacobian matrix needs to be inverted at every time step.

A type of Runge-Kutta methods alleviates this problem by using Butcher tableaus in which the upper right part are zero and the diagonal values are equal ($a_{22} = a_{33} = \cdots = a_{ss}$), except for the first diagonal element, which is $a_{11} = 0$. Therefore, the first step is explicit, saving computational resources, while the method as a whole remains implicit. This class of methods are called ESDIRK (Explicit Singly Diagonally Implicit Runge-Kutta). In *SLH*, the following schemes are implemented: ESDIRK23 [Hosea & Shampine 1996], ESDIRK34, ESDIRK46, and ESDIRK58 [Kennedy & Carpenter 2001], where the first number stands for the formal order of accuracy of the method and the second is the number of stages. The Butcher tableaus of these methods are shown in Miczek [2013, Annex B].

For implicit methods, the constraint for stability dictated by the CFL criterion is lifted. In practice, however, the time step cannot be arbitrary large, as the physical time scale of interest needs to be resolved. One possibility is to use the so-called *advective* CFL condition [Miczek 2013, Section 5.3.1]:

$$\Delta t \leq \mathrm{CFL}_u \min_{q \in \{u,v,w\}} \frac{\Delta x}{|q|}. \tag{3.37}$$

The sole modification to the original CFL criterion, Equation (3.29), is that only the fluid speed $|q|$ without the sound speed c is considered. A CFL_u number of 1, means that an advection wave will move approximately one cell per time step. Time steps of that size will dampen the sound waves, but will resolve the advective ways properly. This criterion is appropriate for applications with low Mach numbers, where sound waves become irrelevant (see Section 3.2).

Additional source terms to the Euler equations beget processes, like thermal conduction or nuclear reactions, that evolve in different time scales than the sound crossing time. Therefore, the criterion in Equation (3.37) alone does not necessarily impose a sufficiently strict time step condition. To take account of the gravity source term and the corresponding free-fall time scale, an alternative criterion was suggested by Miczek [2013], labeled the CFL_{ug} criterion. It is in fact somewhat overly restrictive

in the case of stellar atmospheres, which are anyhow close to hydrostatic equilibrium. Nevertheless, it is useful also in the case of initial conditions with zero or near-zero velocity, as is the case in our own simulations, where the advective CFL criterion would yield a time step size that is larger than the age of the universe.

3.1.4. Boundary conditions

The time-marching methods presented in the previous section require for each of the cell states $\boldsymbol{U}_{i,j,k}$ the information of their neighboring cells. The grid cells at the limits of the numerical domain represent a special case, as per definition they lack neighboring cells on at least one cell face. In addition, the finite volume schemes defined by Equation (3.20) have the property to conserve the quantities $\boldsymbol{U}$, except for fluxes at the boundaries of the domain (and excepting source terms). Therefore, the behavior of these cells needs to be treated with appropriate boundary conditions, in a manner that adequately represents the physical scenario. Especially in the case of *box in a star* simulations as our own, where the computational domain is located inside a star. Lateral boundaries may or not take into account spherical symmetry, while correct vertical boundaries are crucial for the stability of hydrostatic atmospheres.

One possibility is to add so-called *ghost cells* at the boundaries of the domain. These are layers of cells around the domain, whose values are chosen to alter the flux at the boundaries. Alternatively, the fluxes at the boundary cells can be altered directly without using extra ghost cells. Then, the reconstruction schemes must use one-sided interpolation.

Reflective boundary conditions act as a solid, non-transmissive, wall. To this end, the ghost cells are filled with reflected states, in which the momenta components mirror the momenta normal to the boundary. This way, after the reconstruction step, the mass flux at the boundary is approximately zero. Unfortunately, not all reconstruction schemes are able to ensure an absolute zero mass flux. In addition, because the density and energy profiles at the boundary are also mirrored in the ghost cells, this represents an unphysical situation in hydrostatic atmospheres.

Wall boundary conditions are also a zero-flux method, but they belong to the flux boundary conditions. Here, the boundary flux function is modified so that the momenta normal to the boundary interface are zero. The flux depends then only on the wall pressure. This way, sound waves can exit the domain, but there is zero mass flux.

Constghost or constant ghost cells, are filled at the start with values from the initial conditions with zero velocity, but don't change for the rest of the simulation. This boundary condition allows for inflow and outflow, but generally the velocities adjacent to the boundary are underestimated because of the zero velocity at the ghost cells. Nevertheless, this method is well-suited to maintain hydrostatic profiles without excessive artifacts.

Far-field condition, in which a background state of the fluid far-away from the domain is defined, which allows hydrodynamically consistent inflow and outflow. However, this method cannot be used in hydrostatic atmospheres, where the state (pressure and density) is a function of the height.

In our simulations of classical novae, we used mainly the *wall* condition for zero flux, and the *constghost* condition for inflow and outflow.

3.1.5. Coordinate systems and frames of reference

The derivation of the discretization techniques presented in the past sections assumed, for simplicity, Cartesian coordinates. In practice, the discretized Euler equations in *SLH* are implemented in general curvilinear coordinates: ξ, η, ζ. These coordinates are transformed from a global Cartesian coordinate system:

$$x(\xi, \eta, \zeta), \qquad y(\xi, \eta, \zeta), \qquad z(\xi, \eta, \zeta). \tag{3.38}$$

These functions must be invertible and the second derivative of the transformation must commute, but can else be arbitrary. This allows the grid cells, defined by the coordinates of their nodes, to have arbitrary shapes. Skewed or contorted grids, such as the *cubed sphere*, can be used to get around coordinate singularities of polar or spherical grids. The details of the coordinate transformations can be found in Miczek [2013, Section 3.1 and Section 3.3].

The fluid equations presented in this section are written in the *Eulerian* form. That is, the quantities are treated as fields moving through a fixed coordinate system. The velocity field $u(x, t)$, for instance, is expressed by its value at a given position x and a time t. The positions x are often (in structured meshes) discretized values that are chosen according to a specific geometry. In the *Lagrangian* description, the coordinates ξ move with the fluid particles – an infinitesimal volume of the fluid, still many times larger than the mean free path. It is equivalent to tracking a fluid particle as it moves through a streamline, its shape changing due to stress and motion. Then the velocity $U(\xi, t)$ refers to the velocity of this particle at time t. The Lagrangian and Eulerian velocities are related by

$$U(\xi, t) = u\left(X(\xi, t), t\right). \tag{3.39}$$

The map $X(\xi, t)$ gives the physical location of the particle 'labeled' by ξ. The Lagrangian coordinates

$$\xi = \int_{x_0}^{x} ds\, \rho_0(s) \tag{3.40}$$

have the units of mass. ξ gives the total mass between x_0 and $X(\xi, t)$, and $\xi_1 - \xi_0$ the total mass of all fluid particles between them [LeVeque 2002]. When symmetries exist in the system, they can be useful in the Lagrangian formalism. In a spherically symmetric star that is undergoing pulsations, the radius is changing with time (an Eulerian coordinate), but the mass enclosed within its outermost shell (a Lagrangian coordinate) is constant in time. However, in the presence of convection, turbulence or differential rotation, spherical symmetry is broken and the description becomes simpler in the Eulerian formalism. For these reasons, the equations of stellar evolution are more commonly expressed in Lagrangian coordinates, but our simulations of convective flow are performed in an Eulerian grid.

3.2. Low Mach number hydrodynamics

The use of approximate Riemann solvers in RAE schemes enables the efficient simulation of fluid flow in a wide range of applications from engineering to astrophysics. In the supersonic regime ($\mathrm{M} \geq 1$), they are able to capture shocks very accurately within a few cells. On the other hand, the phases of stellar evolution in which we are interested proceed in low Mach numbers ($\mathrm{M} \approx 10^{-6} - 10^{-1}$), where strong shocks are absent. However, common Roe schemes become increasingly dissipative as the Mach number decreases. In stellar plasma, where viscosity is assumed to play a negligible role, numerical viscosity dominates over any kind of true physical viscosity, so that an untreated solver smears out the true solution. Guillard & Viozat [1999] performed an analysis of the asymptotic behavior of the dissipation term in the numerical flux as the Mach number tends to zero, and found that the discretized equations have the wrong scaling order when compared to the analytical result. The solution lies in the use of *flux preconditioning* techniques.

3.2.1. Scaling of the fluid equations with low Mach numbers

The analysis starts with the non-dimensional Euler equations, where the physical quantities are replaced by the multiplication of a non-dimensional factor and a global reference value, e.g. for the density ρ:

$$\rho = \hat{\rho}\rho_\mathrm{r}. \tag{3.41}$$

The hat denotes the dimensionless quantity, the subscript 'r' the reference value. Replacing all quantities in the homogeneous Euler equations with such expressions and canceling the reference quantities results in the non-dimensional fluxes:

$$\hat{\boldsymbol{F}} = \begin{pmatrix} \hat{\rho}\hat{u} \\ \hat{\rho}\hat{u}^2 + \frac{1}{\mathrm{M}_\mathrm{r}^2}\hat{p} \\ \hat{\rho}\hat{u}\hat{v} \\ \hat{\rho}\hat{u}\hat{w} \\ \hat{u}(\hat{\rho}\hat{E} + \hat{p}) \end{pmatrix}, \qquad \hat{\boldsymbol{G}} = \begin{pmatrix} \hat{\rho}\hat{v} \\ \hat{\rho}\hat{u}\hat{v} \\ \hat{\rho}\hat{v}^2 + \frac{1}{\mathrm{M}_\mathrm{r}^2}\hat{p} \\ \hat{\rho}\hat{v}\hat{w} \\ \hat{v}(\hat{\rho}\hat{E} + \hat{p}) \end{pmatrix}, \qquad \hat{\boldsymbol{H}} = \begin{pmatrix} \hat{\rho}\hat{w} \\ \hat{\rho}\hat{u}\hat{w} \\ \hat{\rho}\hat{v}\hat{w} \\ \hat{\rho}\hat{w}^2 + \frac{1}{\mathrm{M}_\mathrm{r}^2}\hat{p} \\ \hat{w}(\hat{\rho}\hat{E} + \hat{p}) \end{pmatrix}. \tag{3.42}$$

Out of all reference quantities, the only one remaining in the system is the reference Mach number $\mathrm{M}_\mathrm{r} = u_\mathrm{r}/c_\mathrm{r}$, the ratio of the reference velocity to the reference sound speed. To analyze the scaling of the equations with M_r, all quantities are asymptotically expanded for $\mathrm{M}_\mathrm{r} \to 0$ in powers of M_r, e.g for ρ:

$$\hat{\rho} = \hat{\rho}^{(0)} + \mathrm{M}_\mathrm{r}\hat{\rho}^{(1)} + \mathrm{M}_\mathrm{r}^2\hat{\rho}^{(2)} + \mathcal{O}(\mathrm{M}_\mathrm{r}^3). \tag{3.43}$$

The expanded equations read:

$$\partial_t \rho^{(0)} + \nabla \cdot (\rho^{(0)} \boldsymbol{q}^{(0)}) + \mathcal{O}(\mathrm{M_r}) = 0 \tag{3.44}$$

$$\partial_t (\rho^{(0)} \boldsymbol{q}^{(0)}) + \nabla \cdot (\rho^{(0)} \boldsymbol{q}^{(0)} \otimes \boldsymbol{q}^{(0)}) + \frac{1}{\mathrm{M_r^2}} \nabla p^{(0)} + \frac{1}{\mathrm{M_r}} \nabla p^{(1)} + \nabla p^{(2)} + \mathcal{O}(\mathrm{M_r}) = 0 \tag{3.45}$$

$$\partial_t (\rho^{(0)} E^{(0)}) + \nabla \cdot (\rho^{(0)} E^{(0)} \boldsymbol{q}^{(0)} + p^{(0)} \boldsymbol{q}^{(0)}) + \mathcal{O}(\mathrm{M_r}) = 0, \tag{3.46}$$

where $\boldsymbol{q}$ is the velocity vector. The terms with negative powers of $\mathrm{M_r}$ must vanish individually, in order for the equation to converge in the limit $\mathrm{M} \to 0$. This yields two conditions:

$$\nabla p^{(0)} = 0, \qquad \nabla p^{(1)} = 0. \tag{3.47}$$

Therefore, the pressure is constant in space up to terms of order $\mathrm{M_r^2}$ [Guillard & Viozat 1999]:

$$p(\boldsymbol{x}, t) = p^{(0)}(t) + \mathrm{M_r^2}\, p^{(2)}(\boldsymbol{x}, t). \tag{3.48}$$

The equation of state is assumed to be that of an ideal gas. Expanding the non-dimensional quantities in $\mathrm{M_r}$ in the non-dimensional equation of state yields:

$$p^{(0)} = (\gamma - 1) \rho^{(0)} E^{(0)}. \tag{3.49}$$

A time-dependance of $p^{(0)}$ according to Equation (3.48) can only be imposed by source terms or boundary conditions. If they are set as constant in the initial conditions, then $p^{(0)}$ remains constant in space and time. With the EoS, Equation (3.49), and the conditions Equation (3.47), the energy equation can be rewritten as:

$$\partial_t p^{(0)} + \gamma\, p^{(0)} \nabla \cdot \boldsymbol{q}^{(0)} + \mathcal{O}(\mathrm{M_r}) = 0, \tag{3.50}$$

and because of the temporally constant $p^{(0)}$, it holds:

$$\nabla \cdot \boldsymbol{q}^{(0)} = 0. \tag{3.51}$$

Therefore, the velocity field must be divergence-free in the zero Mach number limit, i.e., the incompressible case is recovered.

The expansion in $\mathrm{M_r}$ of the compressible Euler equations shows that the pressure fluctuations scale with $\mathrm{M_r^2}$, see Equation (3.48). However, linear stability analysis of the Euler equations (keeping terms up to order $\mathrm{M_r}$) shows that sound waves with arbitrarily small velocity fluctuations are also allowed solutions to the equations, at arbitrarily small $\mathrm{M_r}$ [Miczek et al. 2015]. In sound waves, pressure fluctuations scale linearly with $\mathrm{M_r}$, i.e.:

$$p(\boldsymbol{x}, t) = p^{(0)}(t) + \mathrm{M_r}\, p^{(1)}(\boldsymbol{x}, t). \tag{3.52}$$

Sound waves are not solutions to the incompressible Euler equations. Therefore, in the $M \to 0$ limit, the compressible Euler equations allow for two different solutions: incompressible flows – with $p \propto \mathrm{M_r^2} p^{(2)}$ – and sound waves – with $p \propto +\mathrm{M_r} p^{(1)}$ – which decouple as the Mach number declines.

3.2.2. Flux preconditioning

Miczek [2013] performed an alternative kind of analysis, based on the work of Turkel [1999], to compare the asymptotic behavior of the analytical and discretized equations. In this approach, the scaling with $\mathrm{M_r}$ of the individual matrix elements in the flux functions is compared. The flux function from a Godunov-like scheme can be written as

$$\boldsymbol{F}_{1/2} = \frac{1}{2}\left(A_L\boldsymbol{U}_L + A_R\boldsymbol{U}_R - D(\boldsymbol{U}_R - \boldsymbol{U}_L)\right), \tag{3.53}$$

where A denotes the flux Jacobian matrix and D the upwind matrix. It referred to as *upwind*, because the spatial derivative is one-sided, namely on the side from which the information flows. This ensures that the numerical domain of dependence contains the original domain of dependence of the PDE. The opposite case is called *downwind*, which is unconditionally unstable. Therefore, the upwind term can be regarded as a stabilizing term, equivalent in its effect to dissipation.

Transforming the terms in Equation (3.53) into the so-called primitive variables $\boldsymbol{V} = (\rho, u, v, w, p)^T$ makes the expressions simpler. Then, the non-dimensional flux Jacobian matrix is given by $A_{\boldsymbol{V}} = \frac{\partial \boldsymbol{V}}{\partial \boldsymbol{U}}\frac{\partial \boldsymbol{F}}{\partial \boldsymbol{U}}\frac{\partial \boldsymbol{U}}{\partial \boldsymbol{V}}$, and its individual elements scale as:

$$A_{\boldsymbol{V}} \propto \begin{pmatrix} \mathcal{O}(1) & \mathcal{O}(1) & \mathcal{O}(1) & \mathcal{O}(1) & 0 & 0 \\ 0 & \mathcal{O}(1) & 0 & 0 & \mathcal{O}(\frac{1}{\mathrm{M_r^2}}) & 0 \\ 0 & 0 & \mathcal{O}(1) & 0 & \mathcal{O}(\frac{1}{\mathrm{M_r^2}}) & 0 \\ 0 & 0 & 0 & \mathcal{O}(1) & \mathcal{O}(\frac{1}{\mathrm{M_r^2}}) & 0 \\ 0 & \mathcal{O}(1) & \mathcal{O}(1) & \mathcal{O}(1) & \mathcal{O}(1) & 0 \\ 0 & 0 & 0 & 0 & 0 & \mathcal{O}(1) \end{pmatrix}. \tag{3.54}$$

Applying the same analysis to the Roe scheme, Equation (3.24), reveals the asymptotic scaling of the discretized flux Jacobian:

$$A_{\boldsymbol{V},\mathrm{Roe}} \propto \begin{pmatrix} \mathcal{O}(1) & \mathcal{O}(\mathrm{M_r}) & \mathcal{O}(\mathrm{M_r}) & \mathcal{O}(\mathrm{M_r}) & \mathcal{O}(\frac{1}{\mathrm{M_r}}) & 0 \\ 0 & \mathcal{O}(\frac{1}{\mathrm{M_r}}) & \mathcal{O}(\frac{1}{\mathrm{M_r}}) & \mathcal{O}(\frac{1}{\mathrm{M_r}}) & \mathcal{O}(\frac{1}{\mathrm{M_r}}) & 0 \\ 0 & \mathcal{O}(\frac{1}{\mathrm{M_r}}) & \mathcal{O}(\frac{1}{\mathrm{M_r}}) & \mathcal{O}(\frac{1}{\mathrm{M_r}}) & \mathcal{O}(\frac{1}{\mathrm{M_r}}) & 0 \\ 0 & \mathcal{O}(\frac{1}{\mathrm{M_r}}) & \mathcal{O}(\frac{1}{\mathrm{M_r}}) & \mathcal{O}(\frac{1}{\mathrm{M_r}}) & \mathcal{O}(\frac{1}{\mathrm{M_r}}) & 0 \\ 0 & \mathcal{O}(\mathrm{M_r}) & \mathcal{O}(\mathrm{M_r}) & \mathcal{O}(\mathrm{M_r}) & \mathcal{O}(\frac{1}{\mathrm{M_r}}) & 0 \\ 0 & 0 & 0 & 0 & 0 & \mathcal{O}(1) \end{pmatrix}. \tag{3.55}$$

Clearly, the scaling behavior is significantly different in both cases. As the Mach number tends to zero, the elements in the numerical Jacobian that scale as $\propto 1/\mathrm{M_r}$ grow faster than in the analytical case, and dominate over all other terms of the flux function. The *numerical* dissipation becomes greater than the *physical* one.

A popular approach in the solution of steady-state flows is the use of *preconditioning* matrices. These are specifically chosen operators that applied to matrices

$$A \to P^{-1}A, \tag{3.56}$$

reduce the stiffness of the system, i.e, they even out the eigenvalues of the new matrix[3]. This operation speeds up the convergence to a steady state. Preconditioning

[3] In this context, a stiff system of equations is one where the ratio of the eigenvalues is large.

can also be applied to time-dependent flows. In the case of the Roe fluxes, the upwind matrix is multiplied by an appropriate matrix P. The term *flux preconditioning* is used to distinguish this procedure from the preconditioning of linear system. The flux-preconditioned Roe solver reads:

$$\boldsymbol{F}_{1/2} = \frac{1}{2}\left(\boldsymbol{F}(\boldsymbol{U}_L) + \boldsymbol{F}(\boldsymbol{U}_R) - (P^{-1}|PA|)_{\text{roe}}(\boldsymbol{U}_R - \boldsymbol{U}_L)\right). \tag{3.57}$$

Miczek [2013] found that the scaling of this modified Roe-Turkel scheme[4] is significantly improved, but still contains terms in the fifth column of the upwind matrix which exaggerate the response of density and pressure fluxes to pressure gradients. This is problematic for the simulation of stellar atmospheres, because the stratification in stars has very large pressure gradients. Therefore, even small fluctuations in pressure can lead to spurious fluxes. For this reason, Miczek [2013] proposed an alternative preconditioning matrix:

$$P_{\boldsymbol{V}} = \begin{pmatrix} 1 & n_x\frac{\rho\delta \mathrm{M_r}}{c} & n_y\frac{\rho\delta \mathrm{M_r}}{c} & n_z\frac{\rho\delta \mathrm{M_r}}{c} & 0 & 0 \\ 0 & 1 & 0 & 0 & -n_x\frac{\delta}{\rho c \mathrm{M_r}} & 0 \\ 0 & 0 & 1 & 0 & -n_y\frac{\delta}{\rho c \mathrm{M_r}} & 0 \\ 0 & 0 & 0 & 1 & -n_z\frac{\delta}{\rho c \mathrm{M_r}} & 0 \\ 0 & n_x\rho c\delta \mathrm{M_r} & n_y\rho c\delta \mathrm{M_r} & n_z\rho c\delta \mathrm{M_r} & 1 & 0 \\ 0 & 0 & 0 & 0 & 0 & 1 \end{pmatrix}, \tag{3.58}$$

where

$$\delta = \frac{1}{\min(1, \max(\mathrm{M}, \mathrm{M_{cut}}))} - 1. \tag{3.59}$$

The Roe fluxes preconditioned with the above matrix, christened *Roe-Lowmach* scheme, have the asymptotic scaling:

$$\begin{pmatrix} \mathcal{O}(1) & \mathcal{O}(1) & \mathcal{O}(1) & \mathcal{O}(1) & \mathcal{O}(1) & 0 \\ 0 & \mathcal{O}(1) & \mathcal{O}(1) & \mathcal{O}(1) & \mathcal{O}(\frac{1}{\mathrm{M_r^2}}) & 0 \\ 0 & \mathcal{O}(1) & \mathcal{O}(1) & \mathcal{O}(1) & \mathcal{O}(\frac{1}{\mathrm{M_r^2}}) & 0 \\ 0 & \mathcal{O}(1) & \mathcal{O}(1) & \mathcal{O}(1) & \mathcal{O}(\frac{1}{\mathrm{M_r^2}}) & 0 \\ 0 & \mathcal{O}(1) & \mathcal{O}(1) & \mathcal{O}(1) & \mathcal{O}(1) & 0 \\ 0 & 0 & 0 & 0 & 0 & \mathcal{O}(1) \end{pmatrix}. \tag{3.60}$$

This behavior is compatible with the scaling of the analytic flux Jacobian of Equation (3.54). Therefore, the numerical viscosity resulting form the upwind term should be independent of the Mach number. A rigorous mathematical prove of the stability is still missing, but numerical tests with the Gresho vortex [Liska & Wendroff 2003] have shown the ability of Roe-Lowmach scheme to correctly handle low Mach number flows (see Miczek et al. [2015]).

[4] The specific form of the matrix, as well as a more extensive discussion can be found in the PhD thesis of Miczek [2013, Section 4.3]

3.2.3. AUSM$^+$-up

An alternative approach to the common approximate Roe solver was proposed by Liou & Steffen [1993], motivated by the observation that convective transport and pressure waves are different mechanisms, acting in distinct timescales. Hence, the hydrodynamic fluxes (here exemparily in one dimension) are split into an advective and a pressure part, thusly:

$$\boldsymbol{F} = \begin{pmatrix} \rho \\ \rho u \\ \rho H \end{pmatrix} u + \begin{pmatrix} 0 \\ p \\ 0 \end{pmatrix} = \boldsymbol{F}^{(c)} + \begin{pmatrix} 0 \\ p \\ 0 \end{pmatrix}, \tag{3.61}$$

or concisely as

$$\boldsymbol{F} = \boldsymbol{F}^{(c)} + \boldsymbol{P} = \dot{m}\boldsymbol{\psi} + \boldsymbol{P}, \tag{3.62}$$

with the definitions

$$\dot{m} := \rho u, \qquad \boldsymbol{\psi} := (1, u, H)^T \tag{3.63}$$

Here, H is the total specific enthalpy $H = E + p/\rho$. The convective term can be considered as a set of passive scalars advected with the flow with a *suitable* velocity or Mach number. The pressure flux terms, conversely, are associated with the acoustic speed. Therefore, the discretization of the two parts is done separately.

The numerical flux is written analogously to the analytical flux:

$$\boldsymbol{f}_{1/2} = \dot{m}_{1/2}\boldsymbol{\psi}_{\mathrm{L/R}} + \boldsymbol{p}_{1/2}. \tag{3.64}$$

The subscript '1/2' indicates the interface, and 'L/R' the left and right states. The aim of the method is to define an appropriate cell-face advection Mach number from the values of the adjacent cells, and use the Mach number to determine the upwind extrapolation of the convective variables. The specific method used to define the mass and pressure fluxes is what distinguishes the different AUSM methods (AUSM [Liou & Steffen 1993], AUSM$^+$ [Liou 1996] and AUSM$^+$-up [Liou 2006]). Very generally, the mass flux will be written, in conformance to the idea of upwinding, as:

$$\dot{m}_{1/2} = a_{1/2}\mathrm{M}_{1/2} \begin{cases} \rho_{\mathrm{L}} & \text{if } \mathrm{M}_{1/2} > 0, \\ \rho_{\mathrm{R}} & \text{otherwise,} \end{cases} \tag{3.65}$$

where $a_{1/2}$ is the sound speed at the interface. In Liou [2006], the interface Mach number is, in terms of the left and right Mach numbers $\mathrm{M}_{\mathrm{L/R}} = u_{\mathrm{L/R}}/a_{\mathrm{L/R}}$:

$$\mathrm{M}_{1/2} = \mathcal{M}^+_{(m)}(\mathrm{M}_{\mathrm{L}}) + \mathcal{M}^-_{(m)}(\mathrm{M}_{\mathrm{L}}) + \mathrm{M}_p. \tag{3.66}$$

The 'split Mach numbers' $\mathcal{M}^{\pm}_{(m)}$ are polynomial functions of degree $m(= 1, 2, 4)$. More importantly, the *pressure diffusion term* M_p was introduced to improve the behavior of the scheme in the low Mach number regime. It ensures pressure–velocity coupling at low speeds.

However, Miczek [2013] realized that the pressure diffusion term in the mass flux suffers from the same vulnerability as the Roe-Turkel scheme for nearly-hydrostatic flows. The term scales $\propto 1/\mathrm{M}$ and the local pressure gradient. Such gradients are an attribute of hydrostatic atmospheres, in which case the diffusion term generates vertical mass fluxes. By setting the factor $f_a = 1$ [Miczek 2013, Equation (4.3.25)], the problem is removed. The new scheme is called AUSM$^+$-Lowmach. In tests examining its performance in low Mach numbers and the conservation of hydrostatic stability, the scheme proved to be on a par with the Roe-Lowmach preconditioning.

3.3. Well-balancing

3.3.1. Checkerboard instability

The flux preconditioning methods presented in Section 3.2.2 solve the dissipation problems typical of low Mach number flows. Inadvertently, they also introduce a side effect. In simulations of atmospheres that are initially stable against convection, an instability appears when using the preconditioned fluxes. It shows up as alternating maxima and minima in various physical values. Due to its appearance, it is called 'checkerboard instability'. An example is shown in Figure 3.1, which displays the fluctuations in density from the horizontal mean, just 0.5 s after the start of one of our 2D classical nova simulations. In a given time step, the amplitude is strongest at the white dwarf-envelope interface, where the Brunt–Väisälä frequency has a peak. It is also called bouyancy frequency, and is the frequency with which a fluid element in a dynamically stable layer oscillates around its equilibrum position, as $\Delta r = \Delta r_0 e^{iNt}$. It is defined as [Kippenhahn et al. 2013, Section 6.2]:

$$N^2 = \frac{g\delta}{H_P}\left(\nabla_{\mathrm{ad}} - \nabla + \frac{\phi}{\delta}\nabla_\mu\right), \tag{3.67}$$

where the terms in the parenthesis correspond to those in the Ledoux criterion, see Equation (2.18). This means that in layers where the criterion is not satisfied $N^2 < 0$, N is imaginary and a displaced fluid element does not oscillate but is propelled away.

Without flux preconditioning, in an atmosphere stable against convection, small Mach numbers are present due to discretization errors, and in time they settle at a small mean value. However, with preconditioning, self-amplifying modes grow exponentially in time, leading to spurious motions with Mach numbers which also rise exponentially, eventually surpassing the values of the untreated atmosphere without preconditioning (see e.g. Figure 2.7 in Edelmann [2014]). Ultimately, the true solution is destroyed by the instability. Miczek [2013] realized that this instability emerges with every low Mach number scheme implemented, and also observed this instability in simulations of hydrostatic stratifications in an unrelated code, *Fire Dynamics Simulator*, designed for simulations of fire propagation in buildings. Therefore, it is very unlikely that the instability stems from a bug in our program.

Edelmann [2014, Section 2.4] describes the checkerboard instability in more detail. He suggests that the reason of the checkerboard instability is missing *pressure-velocity coupling* in the preconditioned Roe schemes. That is, the *four-field* mode (or checkerboard mode) allowed by the preconditioned schemes are excited – possibly through discretization errors at the cell boundaries or through source terms like gravity or

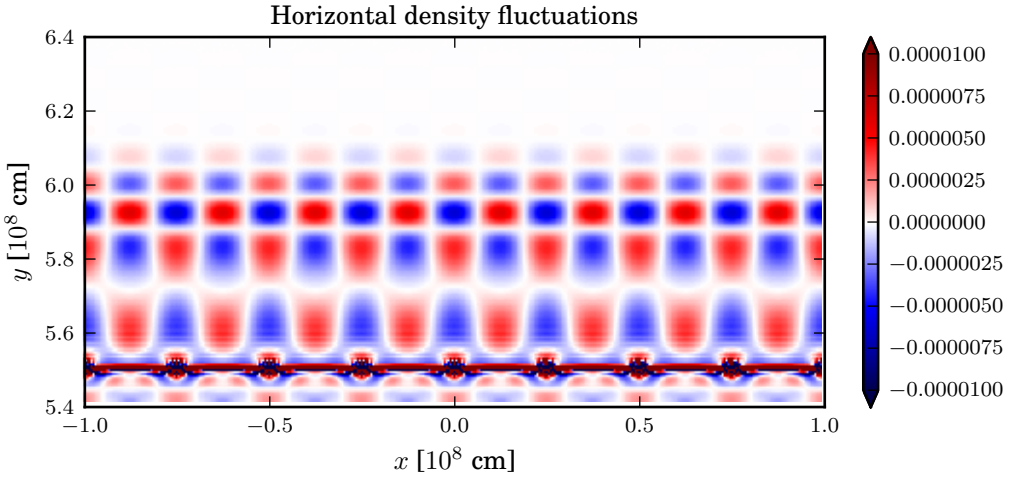

Figure 3.1.
Horizontal density fluctuations in a 2D nova simulation at $t = 0.5\,\mathrm{s}$, before the start of convection. A 'checkerboard' pattern is clearly discernible. The fluctuations are strongest at the interface ($r = 5.5 \times 10^8\,\mathrm{cm}$), where the Brunt–Väisälä frequency has a maximum. The fluctuations at this point reach $\pm 0.1\%$ (the colors are scaled to show that the checkerboard pattern reaches up to higher layers of the envelope).

nuclear energy – at a faster rate than they would naturally damp down. One possible way to solve problems introduced by a gravity source term is *well-balancing*. A method is said to be well-balanced if it is able to preserve the hydrostatic equilibrium. Violations of HSE occur in many schemes at the discrete level, because the ρg source term has a different discretization than the ∇p term. Therefore, an analytically hydrostatic structure will generally have $\nabla p \neq \rho g$ in the discrete description. In the next section, the well-balancing method of Cargo & Le Roux is presented.

3.3.2. The Cargo–Le Roux method

The original method was developed for the one-dimensional Euler equations with gravity [Cargo & Le Roux 1994]:

$$\partial_t \begin{pmatrix} \rho \\ \rho u \\ \rho E \end{pmatrix} + \partial_x \begin{pmatrix} \rho u \\ \rho u^2 + p \\ u(\rho E + p) \end{pmatrix} = \begin{pmatrix} 0 \\ \rho g \\ u \rho g \end{pmatrix}. \tag{3.68}$$

An additional variable can be defined, a potential q with the properties:

$$\partial_x q = \rho g \tag{3.69}$$

$$\partial_t q = -\rho g u. \tag{3.70}$$

The potential can be regarded for the moment to behave like a passive scalar, i.e. it obeys a normal advection equation:

$$\partial_t(\rho q) + \partial_x(\rho q u) = 0. \tag{3.71}$$

This equation can be simplified by applying the product rule and the conservation law for mass, yielding:

$$\partial_t q + u \partial_x q = 0, \tag{3.72}$$

which relates the Equations (3.69) and (3.70). Consequently, if the potential at the initial conditions fulfills Equation (3.69) and its evolution is dictated by Equation (3.71), then Equation (3.70) is also satisfied.

The right hand side of the potential properties, Equations (3.69) and (3.70), are precisely the inhomogeneous side of Equation (3.68). Inserting the terms into the Euler equations thus:

$$\partial_t \begin{pmatrix} \rho \\ \rho u \\ \rho E \end{pmatrix} + \partial_x \begin{pmatrix} \rho u \\ \rho u^2 + p \\ u(\rho E + p) \end{pmatrix} = \begin{pmatrix} 0 \\ \partial_x q \\ -\partial_t q \end{pmatrix}, \tag{3.73}$$

incorporating the derivatives with respect to the same variable, and adding a zero, $0 = q - q$, yields:

$$\partial_t \begin{pmatrix} \rho \\ \rho u \\ \rho E + q \end{pmatrix} + \partial_x \begin{pmatrix} \rho u \\ \rho u^2 + p - q \\ u(\rho E + q + p - q) \end{pmatrix} = \begin{pmatrix} 0 \\ 0 \\ 0 \end{pmatrix}. \tag{3.74}$$

A modified equation of state can be defined, with the modified pressure ϕ and total energy per volume F:

$$\phi = p - q \qquad\qquad F = \rho E + q. \tag{3.75}$$

The modified Euler equations have the same form as the original, homogeneous equations, with the replaced pressure and energy:

$$\partial_t \begin{pmatrix} \rho \\ \rho u \\ F \end{pmatrix} + \partial_x \begin{pmatrix} \rho u \\ \rho u^2 + \phi \\ u(F + \phi) \end{pmatrix} = \begin{pmatrix} 0 \\ 0 \\ 0 \end{pmatrix}. \tag{3.76}$$

From the property Equation (3.69) and the equation of hydrostatic equilibrium, $\partial_x p = -\rho g$, follows that the potential q is the same as the original pressure p up to a spatial constant. Therefore, the modified pressure in a hydrostatic atmosphere is equally spatially constant. The Euler equations with gravity source term has been recast back to a homogeneous, hyperbolic system. Therefore, the Riemann invariants are the same as for the Euler equations. An atmosphere in near hydrostatic equilibrium is close to an isobaric state in terms of the Cargo–Le Roux method. When solving the system Equation (3.76) in *SLH*, the well-balancing property is preserved by all implemented schemes when using pressure and density as the reconstruction variables.

Extension to multi-D

The seemingly obvious extension to multiple dimensions of the potential equation Equation (3.69) would be:

$$\nabla q = \rho \boldsymbol{g} \tag{3.77}$$

However, necessary condition for the existence of such a potential, from the fundamental theorem of calculus and Stokes' theorem, is:

$$\nabla \times \rho \boldsymbol{g} = \boldsymbol{0} \tag{3.78}$$

Then, using $\nabla \times \boldsymbol{g} = \boldsymbol{0}$ it follows that

$$\nabla \times \rho \boldsymbol{g} = -\boldsymbol{g} \times \nabla \rho. \tag{3.79}$$

Therefore, q can only be defined if the density gradient $\nabla \rho$ is (anti-) parallel to the direction of gravity. That is, there should be no lateral density gradients, as in the spherically-symmetric case. Clearly, fluid motions in any direction are allowed by the Euler equations, and particularly in convective regions, lateral variations of temperature and density are natural.

Edelmann [2014] suggests the definition of an *appropriate* horizontal mean ρ_0, such that $\nabla \rho_0$ is indeed parallel to $\boldsymbol{g}$, and hence a potential q can be found:

$$\nabla q = \rho_0 \boldsymbol{g}. \tag{3.80}$$

The equation of state is modified as previously. The resulting equations preserve some of the advantageous properties of the 1D method. However, they are not entirely equivalent, and the momentum components in the modified Euler equations contain source terms of the form $(\rho - \rho_0) g_i$ (for $i = x, y, z$), which correspond to acceleration due to buoyancy. In this method, q is fixed in time. Therefore, if the densities start to depart to much away from ρ_0, the properties of the scheme are partially lost. A possible solution is to regularly update the mean ρ_0 (for details see Edelmann [2014, Section 2.4.4])

4. Engineering a nova model

The origin of classical novae is binary stellar systems. Global parameters such as the masses of both stellar companions and the orbital period determine the mass accretion rate. The composition of the transferred material depends on the type of companion. The macroscopic parameters of the whole system ultimately affect the conditions at the bottom of the accreted envelope, the burning region, in which the physical processes giving birth to the nova outburst take place. In order to perform a multidimensional calculation of a nova explosion, the first deliberation revolves around the stellar parameters: the kind of white dwarf (CO/ONe), mass of the white dwarf and the nuclear composition of the accreted matter. Typically, the evolution of the white dwarf under the influence of accretion is studied in stellar evolution codes until hours or minutes before the final outburst. Multidimensional simulations start from the mapping of such a spherically symmetric configuration to a 2D or 3D grid. Therefore, the crucial part of multi-D nova modeling is the choice of an appropriate model of the radial profiles of the white dwarf–envelope region.

To take the values describing the thermodynamical state of a stellar object obtained through calculation from a one-dimensional Lagrangian code and adapt them for use in multi-dimensional Eulerian code requires several steps. Attention to detail is crucial to ensure consistency between the original model and its multidimensional counterpart. Intuitively, one could take a one-dimensional scalar field –representing any physical value of the star– along the radial coordinate and expand it across one or two orthogonal dimensions to create a two or three-dimensional field, respectively. The programmatic operation is trivial. However, the different nature of Lagrangian 1D and Eulerian hydrodynamical codes means that their values must first be 'translated' from one to the other. Lagrangian codes can capture very steep gradients, while Eulerian codes tend to smooth them out. More importantly, the methods by which these values are computed differ. For instance, if the equations of state differ, a stellar atmosphere that was in hydrostatic equilibrium in the Lagrangian code will not necessarily be so in the Eulerian case, due to differences in the pressure gradients that will not balance the gravitational acceleration. Moreover, boundaries between regions where energy transport is radiation dominated and convective regions can shift, as the Ledoux or Schwarzschild criteria (Equations (2.18) and (2.19)) will not be met at the same positions.

This chapter is structured as follows. In Section 4.1, we discuss the initial conditions of the nova envelope models of Kercek et al. [1998], which form the template for our models. In Section 4.2, we describe our own model-building procedure. A large part of it concerns the spatial discretization mesh, a topic upon which we expand in Section 4.3. With a particular set of simulations, we inspect the details of the core-envelope transition and burning regions in Section 4.4. Section 4.5 briefly describes some experiments with the code *MESA*.The susceptibility of the numerical solution to boundary conditions, box size and perturbations is tested in Section 4.6.

4.1. The Kercek Model

Kercek et al. [1998, 1999] performed 2- and 3D simulations of the thermonuclear runaway in classical nova envelopes. In Section 1.2.2 their results were discussed in the context of the historical progress of the study of novae. In this section we discuss in detail their initial conditions, as they served as template for our own models.

The *Kercek model* consists of a 1 $M_\odot$ CO white dwarf with a hydrogen-rich envelope accreted at a rate of 5×10^{-9} $M_\odot\,\mathrm{yr}^{-1}$ with solar composition in a stellar evolution code. When the temperature at the bottom of the envelope reaches 1×10^8 K in the 1D model, the simulation is stopped. The star's structure is given by the radial profiles of density, temperature, pressure and the mass fractions of twelve nuclear species involved in the CNO cycle. These are ^{1}H, ^{4}He, ^{12}C, ^{13}C, ^{13}N, ^{14}N, ^{15}N, ^{14}O, ^{15}O, ^{16}O, ^{17}O and ^{17}F. These are mapped onto a 2D grid of a modified version of the code *PROMETHEUS* [Fryxell et al. 1989]. The code solves the hydrodynamic equations together with a nuclear reaction network. The equation of state is that of ideal Boltzmann gases of the nuclei, an electron gas component with arbitrary degeneracy and a photon gas component. Heat conduction and magnetic fields are ignored. The atmosphere is relaxed for several hundred dynamical time scales before being mapped onto the full 2D grid. The simulation box spans 1000 km in the vertical direction (several pressure scale heights), where the lower 100 km are the uppermost layers of the white dwarf. Laterally, the domain spans a 0.1π arc of the white dwarf circumference, approximately 1800 km. The curvature of the white dwarf is ignored, the grid has a plan-parallel geometry in Cartesian coordinates. They performed two simulations with equal initial conditions but different grid resolutions. In the first, 100 unevenly-spaced cells in the radial direction and 220 evenly-spaced horizontal cells cover the domain. The second has a finer grid: 500 uneven radial times 1000 even horizontal cells. The cells at the burning region have 5 km × 8 km and 1 km × 2 km, respectively.

Even though the initial conditions were essentially the same in Kercek et al. [1998] and Kercek et al. [1999] as in Glasner et al. [1997], their results stand in stark contrast. Some differences were to be expected, as they employed different codes. However, Kercek et al. obtain a much more modest enrichment of envelope than the Glasner team. In a subsequent paper, Glasner et al. [2005] argue that the reason behind the discrepancy is the boundary condition at the top of the simulation box. For a runaway to occur, a critical pressure must be present at the bottom of the envelope (Equation (1.7)). An inflow-outflow boundary at the top of the simulation box, as implemented in the simulations of the Kercek team, allows mass to escape from the domain, resulting in a gradual drop of pressure. The arbitrary-Lagrangian-Eulerian scheme of Glasner et al. expands with the envelope, while preserving the pressure at the burning region.

The next section illustrates in detail the modifications applied to the one-dimensional model for appropriate use in our multi-dimensional code. In the first part, we explain how we dealt with the distribution of nuclear mass fractions. Next, we explain the integration of the hydrostatic equilibrium equation. In some cases, the integration is performed twice: first to ensure that hydrostatic equilibrium holds throughout the computational domain, and a second time to constrain convection only to the

envelope.

4.2. The Würzburg Model

The initial conditions for our calculations are based on the Kercek model. Lacking the actual numerical data, our model building procedure starts by digitizing the figures of the paper Kercek et al. [1998][1]. Radial profiles of temperature and density are accessible. However, not all quantities needed to fully describe the atmosphere are presented in the publication. Profiles of ^{12}C, ^{14}O, ^{15}O and ^{17}O are included in the publication; for the remaining isotopes, we take several steps to fill the gaps and obtain a sensible model. Our region of interest comprises the outermost layers of the degenerate white dwarf and about 900 km of the accreted envelope. They are treated separately, as they are quite distinct in composition and density.

4.2.1. Treatment of the isotopic mass fractions

In the envelope region (we define this to be above $R \geq 5500\,\mathrm{km}$), we used the solar composition values for the species not included in Kercek et al. [1998]. The elemental abundances of the "solar-like" envelope used in KHT are the same as in Glasner et al. [1997]; they used tables provided by Anders & Grevesse [1989]. The abundances used in *MESA* stem from more recent data of abundances in the solar system by Lodders [2003][2]. Specifically, the mass fraction of ^{1}H and ^{4}He are $X = 0.749$ and $Y = 0.237$. We want to preserve the profiles of the four isotopes mentioned above. These exhibit some features near the burning region, which are traces of the nuclear activity of the evolution of the model in 1D, up to the point where the simulation was stopped. Two criteria must be fulfilled. First, the metallicity of the envelope is normalized to the canonical $Z = 0.02$. Second, for each cell, the sum $\sum_i X_i = 1$ must hold.

For the core, we assume mass fractions of ^{12}C and ^{16}O in equal parts. As in the envelope, we want to preserve the profiles available from the Kercek paper. In a small area $5500\,\mathrm{km} > r > 5498\,\mathrm{km}$ just above the interface, the mass fractions of ^{14}O, ^{15}O and ^{17}F from Kercek et al. [1998] exhibit some features stemming from the quiescent burning stage prior to the runaway. These details are preserved. In the final step, all mass fractions are normalized to 1.

4.2.2. Hydrostatic equilibrium

Once the mass fractions have been treated appropriately, all quantities needed for describing the thermal state of the star are at hand. In general, after re-gridding and interpolation steps, the stratification is not hydrostatically stable. To enforce hydrostatic equilibrium (HSE), the equation

$$\frac{dp}{dr} = -\rho g \tag{4.1}$$

[1] This is the reason we refer to the model as 'Kercek' and not 'Glasner'.

[2] The elements H, C, N and O are highly volatile and incompletely condensed in meteorites. They are also depleted at the solar corona through a fragmentation process. Therefore, only photospheric data can be used for their abundance determination.

must be integrated numerically. The density ρ and pressure are related by the equation of state, so we rewrite the equation as

$$p'(r) = \rho\left(p(r), X_i(r), T(r)\right) g_r(r). \tag{4.2}$$

The vertical extension of the domain in our simulations is typically 1000 km, which is $\approx 20\%$ of the white dwarf's radius. Over this distance, gravitational acceleration can't be approximated as being radially constant. We use a point-source square law for the acceleration g acting on each radial shell. Temporally constant gravity is an acceptable approximation because the free-fall time scale during a nova event is much larger than the nuclear time scales and the typical time scales of our simulations, which is in the order of minutes.

Equation (4.2) can be solved numerically for p if an initial value p_0 and the profiles of X_i and T for each cell are given. Alternatively, one can use the specific entropy s instead of T as the given variable. Also, if the density ρ is known, p can be calculated by numerical integration. When performing these operations, only the 'given' quantities will remain identical to the original data, while the rest are derived from the EOS and the hydrostatic equilibrium.

First integration

In classical novae, where the nuclear energy rate from the CNO cycle is extremely sensitive to temperature variations, (see Figure 4.6), it is of critical importance to capture the peak of the temperature profile. It lies at the base of the envelope. For this reason, when integrating Equation (4.2), we choose the temperature to be the fixed variable. The density is then derived from the EOS, but the nuclear energy rate is less dependent on density, so the difference between integrated model and the original data will be smaller.

Second integration: definition of the convective boundary

A common characteristic of nova models is the strict boundary between the envelope, which at the stage of the mapping from 1D to multi-D is fully convective, and the surface layers of the white dwarf, which according to 1D models energy transport is radiative.

A stratification is said to be radiative if it fulfills the Ledoux criterion (Section 2.1.2, Equation (2.18)), convective otherwise. This criterion can be rewritten in terms of the Brunt–Väisälä frequency as $N^2 < 0$. Analyzing the Brunt–Väisälä frequency after the first HSE integration, we find that the situation is not clear-cut across the interface. The envelope displays alternating stable/unstable layers, where we would expect one homogeneous layer of convective instability (see Figure 4.1, panel (a)). In some cases, N^2 becomes negative also in parts of the white dwarf, where it ought to be free of convection. Panel (b) shows a snaphot of a simulation that initiated from an atmosphere with such an alternating stratification. Convection arises in disjoint layers that do not merge with time. The eddies remain small (smaller than a pressure scale height) throughout the length of the run, and with small velocities. The results are slow cross-boundary mixing and a paucity of white dwarf ^{12}C in the envelope, which does not lead to a runaway in the simulated time of a few hundred seconds.

To solve this problem, we solve Equation (4.2) again, this time with the specific entropy s from the last step as the given variable. By setting the entropy in the envelope as a constant, slightly superadiabatic gradient $\partial s/\partial r$, we aim to ensure that the buoyancy frequency is negative throughout the envelope. Conversely, the gradient in the white dwarf should be radiative. The results from this procedure are not always predictable, and some patience is needed to fine-tune the temperature and entropy profiles until the desired result is obtained; hence the term 'stellar engineering'. An improved stratification, where $N^2 < 0$ is constrained to the base of the envelope, is shown in panels (c) and (d).

In a discrete atmosphere, the balance of both sides of Equation (4.1) will seldom be exact. Deviations from perfect equilibrium are especially large at the convective boundary, where the density changes in a small region by one order of magnitude.

One aspect omitted in the previous paragraphs, but also implicitly present in Equation (4.2), is the discretization of the radial coordinate r. The spatial discretization in curvilinear coordinates Equation (3.38) allows for a flexible definition of meshes by the coordinates of cell centers or cell nodes ('corners'). This mesh remains fixed in time, as our code includes neither adaptive mesh refinement nor a moving grid at the time of this writing. Therefore, the shape of the grid must be chosen carefully. It turns out that the specific way in which the spatial grid is defined and the subsequent integration of the HSE equation along this grid is the single most difficult step in our modeling procedure. While the definition of a prescription for the cell radii is a menial task, the strong change of all important physical quantities across the white dwarf–envelope boundary makes the effects of the discretization particularly laborious. Therefore Section 4.3, is dedicated to this regard, explaining some alternatives and pointing out possible pitfalls.

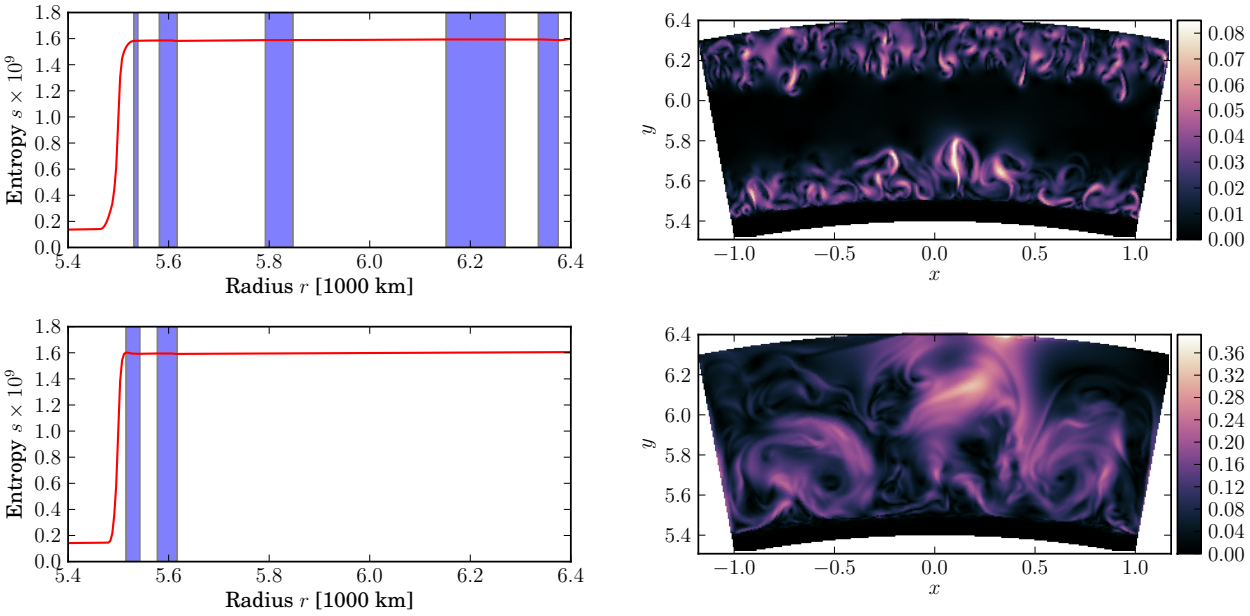

Figure 4.1.
Panel (a) shows the entropy profile in red resulting from the first hydrostatic equilibrium integration. The shaded blue regions signal the strata that are unstable against convection. In this case, some regions almost at the uppermost end are also convectively unstable at the start of the simulations. (b) The result are disjoint convective layers that do not merge, the eddies at the burning region do not grow and the velocities are small. (c) The profile from the upper panel is straightened slightly to restrict convection to a few layers above the star-envelope. (d) The convective eddies resulting from this initial configuration ultimately fill up the whole box and achieve higher velocities.

4.3. The spatial grid

The differential equations that govern the flow must be solved on a discrete grid with a finite number of cells. A physical scenario with complete isotropy, per definition, does not require a mesh with a singled-out axis. On the other hand, in *box in a star* simulations where a concrete region of a star is calculated in a computational box of finite volume, the radial axis of the star is a clear reference axis. In our specific case where we study a stellar region with a convective boundary, the radial coordinates of the grid cells sampling this boundary acquire a particular importance. Consider two hypothetical cases where the vertical extension Δr of a volume centered around the core-envelope interface is sampled with a number n_r of equilateral cells in one grid, and the cell centers are shifted by a small and arbitrary amount δr in a second grid. Our experience shows that the results will be in general significantly different. This was noted by Krueger [2012]. The large effect of the grid radial coordinates is due to several issues. First, the large density and composition jump across the star-envelope boundary means that interpolating from a stellar evolution model onto a hydrodynamic grid, where the former in general has many times the number of cells than the latter, will inevitably create some aliasing effects when interpolating. This in turn strongly affects the calculation of the hydrostatic equilibrium discussed in the last section. The second issue concerns the very steep dependence on temperature of the energy generation rate of the hot CNO cycle. In the case in which the hydro grid does not sample the peak of the temperature profile of the initial model appropriately, the cells around the peak will have values different from the initial model. Due to interpolation effects, particularly noticeable in discontinuous data, the shape of the peak becomes distorted, so that the peak position is shifted to neighboring cells. Because we integrate the HSE with the temperature as the given value, this effect propagates to the entire stratification. A third issue involves the spatial position of the point where the integration of the hydrostatic equilibrium starts. These issues are explained in detail in the following paragraphs.

When the resolution of the grid is increased (the cell size is reduced and the number of cells in the domain increased), the spatial discretization errors become smaller. With increasing resolution, these errors should should asymptotically approach zero and the numerical solution, ideally, approaches the true physical solution. Figure 4.2 shows the density profiles of two nova setups, where one grid has twice the vertical resolution of the other. In an ideal situation, both curves should fall on top of each other. In a logarithmic scale, almost no difference is observable. However, a detailed inspection reveals significant differences. The grid with resolution $n_r = 512$ has a consistently higher density ρ both in the core and envelope sections. The difference between the profiles suffice to make them not physically equivalent; the dynamics and energetics resulting from them will be not only different because of the numerical resolution, but also for physical reasons. In a comparison of both simulations, it becomes challenging to distinguish between numerical and 'real' physical effects. The profiles shown in Figure 4.2 are from two of our simulations. The origin of this defect went undetected for some time. The reason lies in the subtleties in which the sampling points for the grid are defined.

Let the typical height of our simulation boxes be Δr. One can distinguish two

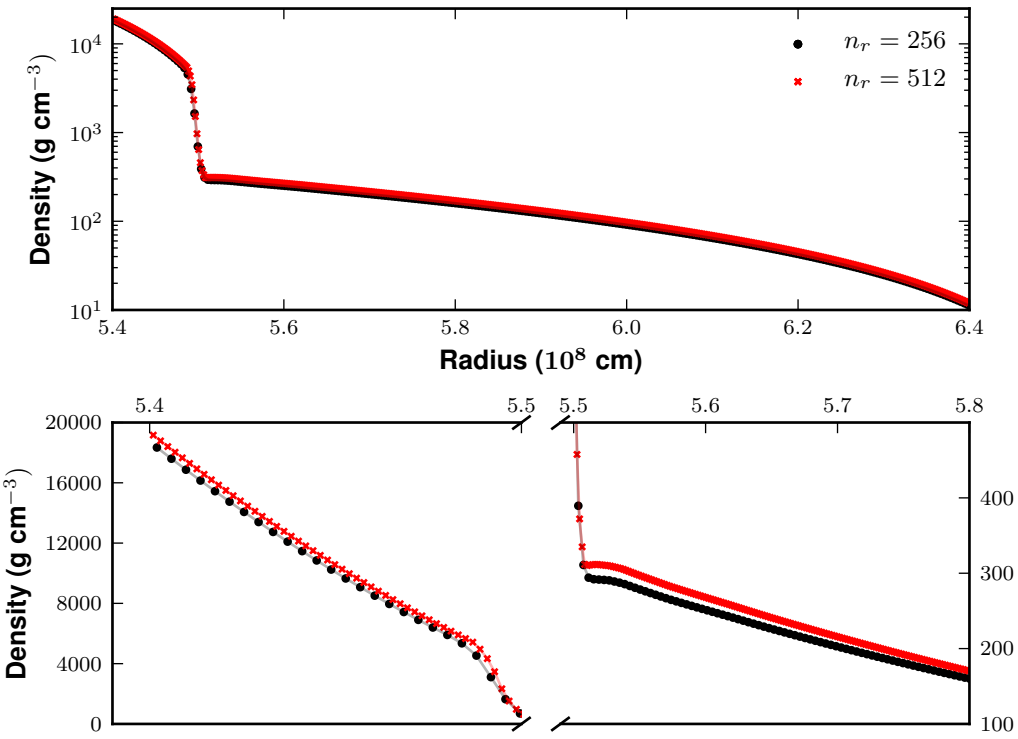

Figure 4.2.
Density profiles of initial conditions of the same atmosphere, in two resolutions. Modifying the resolution shouldn't affect the profile's shape. The marginal shift of the bottom cell's center r_0 without correcting for the density results in small but critical differences at the burning region and envelope.

ways of specifying this length. For one, it can be defined as the distance between the lower boundary of the deepest cell and the upper boundary of the highest cell. In this approach, the cell *faces* of the lowest and highest cells f_0, f_{n_r-1} are fixed – their cell centers are not – when the number of cells are doubled: $n_r' = 2^m \times n_r$. This kind of grid was implemented in our initial runs, in which we tested the sensitivity of the solution to the boundary conditions. In that case, the distance between the boundaries Δr should be equal when comparing different setups (see Section 4.6.1). The disparity in the models in Figure 4.2 lies at integrating the hydrostatic equilibrium starting from the bottommost cell, while taking the same initial density ρ_0 from the original model in both cases, despite the fact that the radii r_0 –the cell centers– are not identical, as shown in Figure 4.3. An alternative approach is to define the grids by fixing the boundary cells' *centers*, r_0, r_{n_r-1}, of the extreme cells instead. In this case, doubling the resolution keeps the cell center r_0 intact.

The ideal discrete grid should have fine enough cells to resolve the smallest scales of the physical processes one intends to simulate. Diffusion across a chemically inhomogeneous boundary operates in microscopical scales that are many orders of magnitude smaller than the size of the computational box. Shear flow-induced Kelvin-Helmholtz (KH) instabilities, on the other hand, can be resolved. According to Chandrasekhar

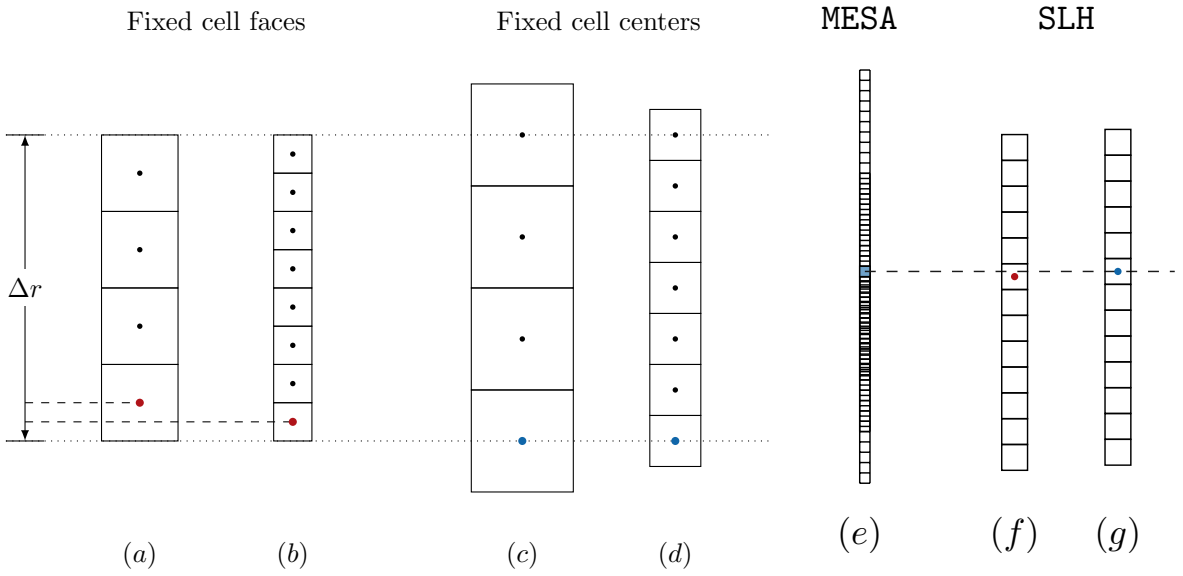

Figure 4.3.
Schematic of possible grid prescriptions. The typical vertical size of our simulation boxes is Δr. (a,b) Doubling the resolution while preserving distance between the extreme cell faces as Δr displaces the cell center of the bottommost cell. (c,d) Alternatively, defining Δr as the distance between the extreme cell centers makes the integration from the bottom consistent. (e) The grid in stellar evolution codes is irregular. (f,g) The grid in the hydro code must capture the peak source shell temperature of the 1D model.

[1961], the minimal unstable wavelength to the KH instability is

$$\lambda_{\mathrm{inf}} = \frac{2\pi\alpha_2(U_1 - U_2)^2}{(\alpha_1 - \alpha_2)g}, \tag{4.3}$$

where the two indices indicate the white dwarf and the envelope, respectively. The α_i are

$$\alpha_1 = \frac{\rho_1}{\rho_1 + \rho_2}, \qquad \alpha_2 = \frac{\rho_2}{\rho_1 + \rho_2}, \tag{4.4}$$

the U_i are the transversal velocities and g the gravitational acceleration. Glasner et al. [1997] found a value of $\lambda_{\mathrm{inf}} = 5\,\mathrm{km}$ for their simulations. The smallest cells in the grid of Kercek et al. [1998] had a size of $1\,\mathrm{km} \times 2\,\mathrm{km}$. We aim to resolve comparable scales.

We are typically computing models with grid cell numbers $n_r \times 2n_r$, with $n_r = \{256, 512, 1024\}$. A simulation box of size $L \times 2L$, with $L = 1000\,\mathrm{km}$ would require 1024×2048 grid cells to resolve $\lambda_{\mathrm{inf}} = 1\,\mathrm{km}$. The explicit timestep is limited by the CLF criterion, which scales also with the cell size Δx:

$$\Delta t \leq \mathrm{CFL}_{uc} \min_{q \in \{u,v,w\}} \frac{\Delta x}{|q| + c}. \tag{4.5}$$

With the sound speed at the base of the envelope $c_{\mathrm{s}} \approx 1.5 \times 10^8\,\mathrm{cm\,s^{-1}}$ and grid cells with $\Delta x = 1 \times 10^5\,\mathrm{cm}$ (radial resolution $n_r = 1024$), the timestep is $\Delta t \approx 3 \times 10^{-4}\,\mathrm{s}$.

It takes approximately 200 s for the TNR to develop. This is also about the same time scale of a full CNO cycle. Ideally, a simulation should run for at least two cycles. A simulation of 500 s duration would require 15 million time steps. Running multiple simulations to test the effect of the many numerical and physical parameters that can affect the solution becomes very expensive. One option may be to reduce the resolution when performing only tests. In our case this is not a solution, as large cells affect very strongly the flow at the interface and, as numerous runs showed, often lead to undesirable results (negative energy or density).

The burning region lies at the base of the envelope; the onset of convection and mixing occur at the region around the interface. Therefore it is reasonable to resolve that region with finer cells and sample the regions farther away from it with larger cells. This is the idea behind the radially 'uneven mesh', whose cell sizes are computed according to the following derivation.

Consider two neighboring grid cells i and $i+1$, the latter standing farther away from the interface cell i_0. The cell $i+1$ will have a slightly larger height than i, thus $dr_{i+1} = (1+\alpha)dr_i$, with some $\alpha > 1$ yet to be derived. Let the height of the cell i_0 at the interface be dr_0, then the height of the ith cell must be

$$dr_i = (1+\alpha)^{i-1} dr_1. \tag{4.6}$$

If r_1 is the radius at which one starts the grid spacing and r_2 is the upper boundary, then r_2 is reached from r_1 after summing over the heights of n cells:

$$\begin{aligned} r_2 = r_1 + \sum_{i=1}^{n} dr_i &= r_1 + dr_0 \sum_{i=1}^{n} (1+\alpha)^{i-1} \\ &= r_1 + \frac{dr_0}{1+\alpha} \sum_{i=1}^{n} (1+\alpha)^{i} \\ &= r_1 + \frac{dr_0}{1+\alpha} \left(\frac{1-(1+\alpha)^{n+1}}{1-(1+\alpha)} - 1 \right). \end{aligned}$$

In the last step, the geometric series was applied. Finally, rewriting $r_2 - r_1$ as Δr and simplifying yields

$$\frac{\Delta r}{dr_0} = -\frac{1-(1+\alpha)^n}{\alpha} \tag{4.7}$$

Thus, with a fixed Δr, a given number of cells n and an initial (smallest) height dr_0, one can solve Equation (4.7) for α and the height of every cell is then given by Equation (4.6).

Assuming a uniform grid and a computational domain of 1000 km height in the vertical direction, the smallest scales that can be resolved with n_r cells are listed in Table 4.1. A visualization of this is given in Figure 4.4. It shows the cell height of various grids in an area around the interface. The horizontal lines are the cell sizes for grids with uniform, equilateral cell spacing, with $n_r = 256, 384$ and 512. To understand the scatter plots showing the non-uniform grid, further explanation is needed. The white dwarf's outer layers take up the bottom $\approx 12\,\%$ of the computational domain. For a coarse resolution of $n_r = 256$, this corresponds to the bottom ~ 31 cells. If we

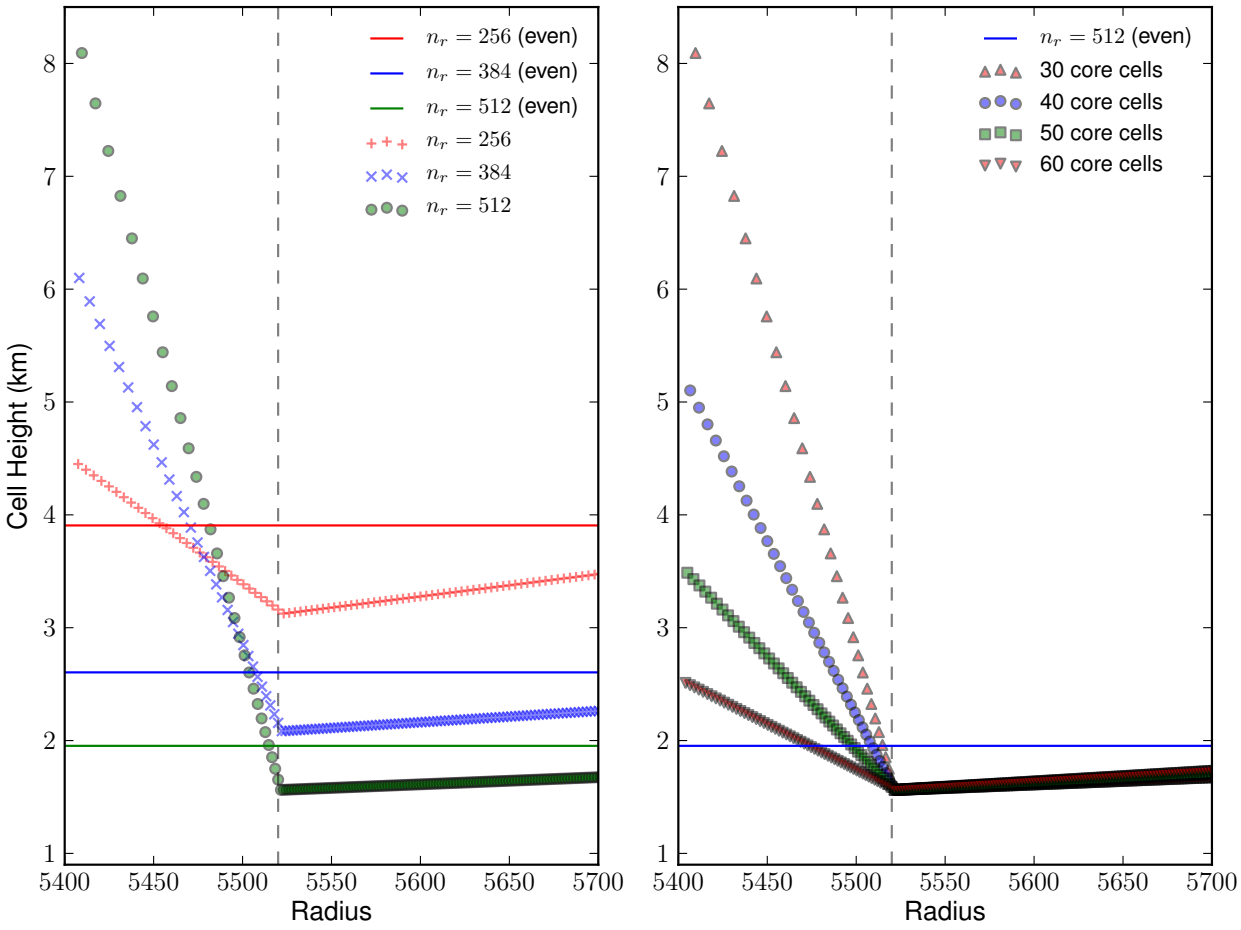

Figure 4.4.
Cell sizes in the uneven grid in the `echo` setup using Equation (4.6). The cells become progressively smaller as they approach the interface (*vertical line*). Details in the text.

wished to resolve the envelope with a finer discretization than the core, based on the observation that the fluid motions are much faster in the envelope, we could choose to increase the total number of cells, but leave the cell number on the core around 30, as in Table 4.1. The resulting cell sizes are the scatter plots in Figure 4.4. The area close to the interface (*vertical line*) is more finely resolved. Consequently, the areas close to the bottom and top boundaries have larger cells than they would in an evenly spaced mesh. Increasing the number of cells from 256 to 512 while assigning only 30 cells to the core allows us to resolve the burning region with even higher precision. We performed several test runs with these parameters, the `echo` runs, listed in Table 4.2. This stands in contrast to the distribution of cells between core and envelope in the Glasner and Kercek simulations, where the core has a higher cell density than the envelope. Experience shows that strong gradients where the density changes by one order of magnitude should be resolved with at least 10 cells (Rüdiger Pakmor, personal communication). In hindsight, it appears more reasonable to dedicate more cells to the core than the envelope.

	Even spacing			Uneven spacing		
n_r	n_{core}	n_{env}	dr_0	n_{core}	n_{env}	dr_0
256	30	226	3.91	32	224	3.13
384	—[a]	—[a]	2.60	32	352	2.01
512	55	457	1.95	30	482	1.56
1024	111	913	0.98	—[a]	—[a]	0.78

Table 4.1.
Smallest scales resolved with two different prescriptions for the grid. [a]Simulations that were not actually performed.

Nevertheless, let's entertain the `echo` for the next discussion. With a small, fixed dr_0 in Equation (4.7) at the core-envelope interface, one forces the desired resolution where it is most important. In practice, with a computational box of fixed horizontal width of the box, the horizontal resolution cannot be completely neglected. Varying cell height dr and constant cell width $r\,d\phi$ means the cells change their aspect ratio as their distance from the interface increases. Cells whose aspect ratio depart too much from $a_{r,\phi} = dr/(r\,d\phi) \approx 1$ have different numerical viscosities along their two axes. It also means that convective eddies, which in two dimensions are approximately circular, will be better resolved in one direction than the other(s), and thus more quickly distorted by the rectangular form of the cells and the anisotropy of the viscosities. Let the horizontal width of the box[3] be $W = 800\,\text{km}$. In test run (a), we force $dr = 1\,\text{km}$ at the interface. With 256×256 cells and equidistant horizontal spacing $d\phi$, it amounts to $r\,d\phi = 3.125\,\text{km}$. In a second test, (b) the minimal cell height at the interface r_i is chosen so that $a_{r,\phi} \approx 1$. Figure 4.5 shows the Mach numbers in two simulations with meshes according to these prescriptions, at $t = 23\,\text{s}$. In case (a), allowing the cells at the interface to be arbitrarily thin results in radially elongated cells in the envelope, $a_{r,\phi} \ll 1$. The convective eddies become deformed and the velocities in the vertical fluxes are disproportionately high. Case (b) shows a flow similar to a grid with equilateral cells. The eddies remain approximately circular and no excessive Mach numbers develop.

Despite all of the above considerations, one final issue is missing. Resolving the peak of the temperature as given by the initial model onto the hydro grid is of paramount importance [Krueger 2012]. The "clipping" of the temperature peak by choosing an inappropriate sampling not only lowers the *value* of the maximum temperature, but it also shifts its *radial position*, altering the stratification of the upper atmosphere. Therefore, the grid must be chosen so as to capture the temperature peak in the cell center of a given cell and constructing the rest of the cells around this key cell. This method was proposed by Zingale et al. [2002] and is presented in the next section.

[3]In the echo simulations we chose a box with similar dimensions to that of Casanova et al. [2011], both to be able to compare to their 3D runs and to reduce the cell width $d\phi$

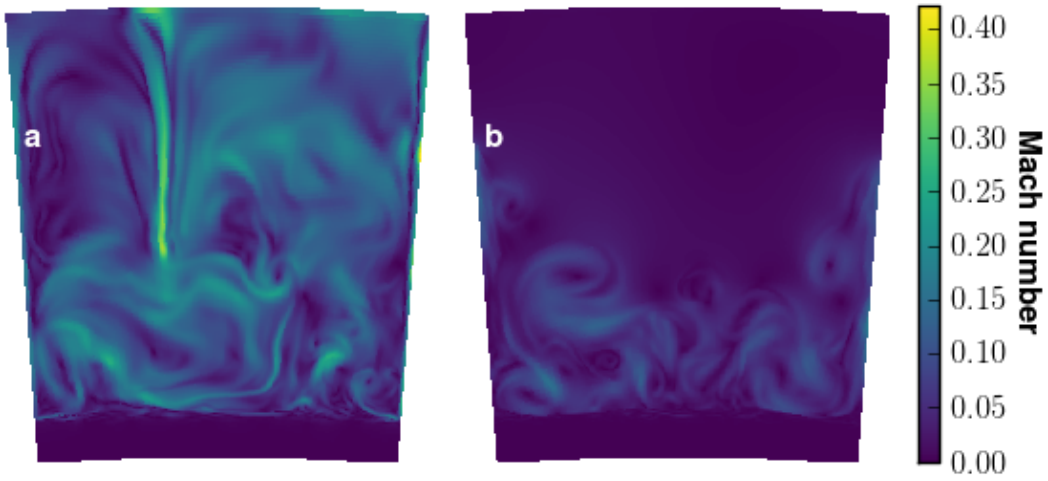

Figure 4.5.
Two simulations with uneven radial cell spacing according to Equation (4.7), at $t = 23\,\mathrm{s}$. (*a*) Arbitrarily thin cells at the interface make the cells at the envelope vertically elongated and the velocities in the radial direction are magnified. (*b*) has 'equilateral' cells at the interface. The maximum Mach numbers are Ma = 0.42 and Ma = 0.17, respectively.

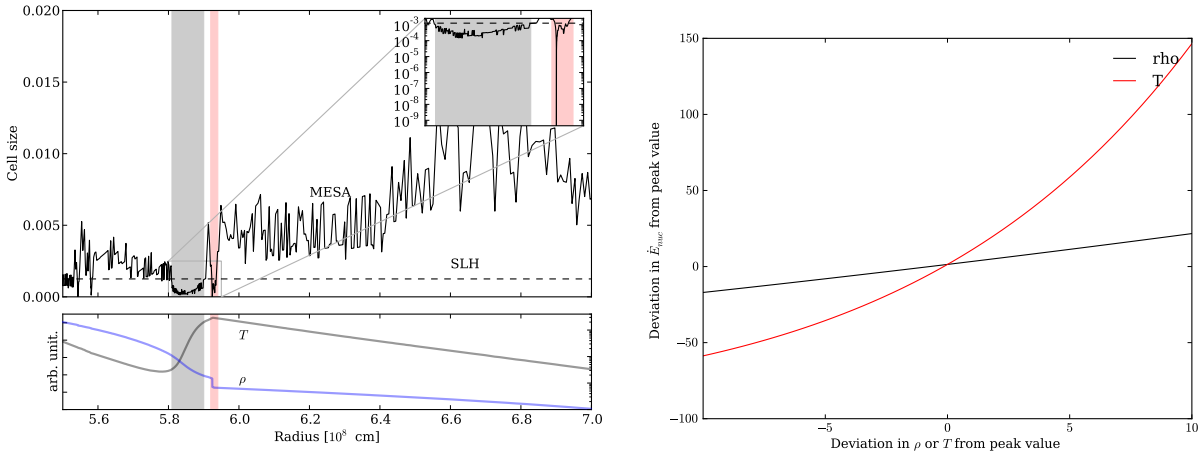

Figure 4.6.
(*Left*) The cell sizes of the Langrangian grid in the evolution code *MESA*, compared with a uniform grid in *SLH*. In the transition region and especially at the base of the envelope (*red area*) the *MESA* grid has very fine cells. (*Right*) The sensitivity of the nuclear energy rate to temperature and density at the burning layer in the *MESA* model. When interpolating, even a 1% deviation from the initial model create large errors ($\approx 10\%$) in the resulting nuclear energy generation rate.

Simulation	n_r	n_{core}	n_{env}	Resolution[a] (km)
Dp256	256	32	224	3.91
Dp512	512	64	448	1.95
Dp1024	1024	128	896	0.98
Ep256	256	32	224	3.13
Ep384	384	32	352	2.08
Ep512b30	512	30	482	1.56
Ep512b40	"	40	472	"
Ep512b50	"	50	462	"
Ep512b60	"	60	452	"
Glasner et al. [2005]	180	130	50	—[b]
Glasner et al. [2007]	113	22	91	1.4
Glasner et al. [2012]	—[b]	—	—	1.4

Table 4.2.
The number of cells in the literature and our own simulations. [a] The resolution of the smallest cell at the interface. [b] Not specified in the source.

4.3.1. Improved integration of hydrostatic equilibrium

Zingale et al. [2002] performed an extensive study of many issues regarding the mapping of one-dimensional models to multi-dimensional codes, including the choice of proper boundary conditions and restoring hydrostatic equilibrium after a re-gridding step. In one test case the authors investigated a model with similar characteristics to ours: a neutron star star accreting H and He until it has formed a fuel layer on top, which ignites into a TNR. This layer is much more compact than on a white dwarf because of the deeper gravitational well of neutron stars. The model was evolved in the one-dimensional code *KEPLER* [Weaver et al. 1978], and stopped shortly before the runaway. The composition change is abrupt between the dense neutron star matter and the H/He layer, as is the density jump. The Lagrangian grid is irregular and denser than the Eulerian grid that would be used in the multi-dimensional *FLASH* code, so the data must be re-gridded and interpolated, just as in our case. Because the EOS in *KEPLER* and *FLASH* differ, the thermodynamic variables must be updated. They find a difference in the values of less than 1%. The particular characteristic in this and our model is the strong density and composition jump at the region of interest. When hydrostatic equilibrium is recalculated after the re-gridding step, a point in the model must be chosen, where ρ, T and X_i remain fixed variables and the integration is performed outward from there. In the last section, we discussed that the location of this point must be consistent when resizing the grid. In the cases shown in Figure 4.2, we always integrated from the lowest cell (including ghost cells) upward (recall also Figure 4.3). [Zingale et al. 2002, Fig. 9] shows an example of a similar procedure. Because of the differences in the EOS between the codes, the

disagreement between the original model and the newly integrated model propagates upward with the integration, and is especially strong across the star-fuel discontinuity. The density of the envelope is then significantly lower than in the original model. The alternative is to start the integration at the core-envelope transition, they chose the cell at the bottom of the fuel layer. Integrating outward from there keeps the area just below and above the interface fairly close to the original model, and the greatest differences are at the bottom and top boundaries, which should affect the results to a lesser degree. In the most recent version of our model builder, we center the grid around the peak of energy generation [Krueger 2012] and start the integration at the interface [Zingale et al. 2002], thus profiting from the benefits of both methods.

4.4. Behavior of the core-envelope transition

The last section covered the several details of the spatial discretization needed for our nova simulations. In this section, we analyze a particular subset of them, with an emphasis on the quantities at and around the core-envelope transition and the burning region. An overview of the evolution of our modeling procedure is given in Table 4.3. In this section, we deal primarily with the `delta` runs.

For our preliminary test runs, we chose a radial resolution of $n_r = 256$. As we worked toward higher resolutions in search for convergence, our analysis showed the discrepancies illustrated in Figure 4.2 and thoroughly discussed in the previous section. No convergence was found. Instead, with finer gridding, the flow develops lower Mach numbers, lower peak temperatures and slower dredge-up efficiencies. The reason behind this is investigated in the next paragraphs.

Figure 4.7 shows the crucial quantity for the dynamics and nucleosynthesis of the TNR, the nuclear energy generation rate $\dot{\epsilon}_{\mathrm{nuc}}$ for three simulations of increasing resolution: `Dp256`, `Dp512` and `Dp1024`. At the start of the simulations, the energy rate is higher in the more finely resolved simulations. This difference is owed to sampling error of the temperature peak. The relevant question is how these differences in the initial conditions will affect the outcome of the simulation. In the first dozen seconds, the energy generation drops quickly in all three cases. They fall with practically the same slope (in a log scale) for the first $\sim 10^1$ seconds. Afterward, energy generation recovers and rises steadily for `Dp256` and `Dp512`. The run with the coarsest resolution develops the highest energy rates. In `Dp1024`, $\dot{\epsilon}_{\mathrm{nuc}}$ reaches a plateau and falls again. We expect that the curve would rise again in time, if the simulation were to continue. The simulations with higher resolution were not run for much longer times due to time constraints. At this stage, it seems puzzling that the simulation with the initially highest $\dot{\epsilon}_{\mathrm{nuc}}$ should exhibit the least violent burning.

Figure A.1 (in Appendix A) shows the time evolution of four key values of the run `Dp256` in a small region around the WD-envelope transition. Time points to the right along the abscissa. The ordinate is the radius in units of R_{WD}. For each t and r, the averages of all cells in horizontal direction of a physical value is plotted. We define the lateral average of the quantity q as

$$q_{\mathrm{avg}}(y,t) = \langle q(x,y,t) \rangle_x \tag{4.8}$$

Generation	Description
`alpha`	Proof of concept
	Test of boundary conditions, box size, resolution
`bravo`	Digitized Kercek et al. [1998]
	Tests of perturbations
`charlie`	Control BV-frequency: correct interpolation and mapping 1D → 2D
`delta`	
`echo`	Uneven vertical grid cells, finer at the burning region
	3D simulations
`foxtrot`	Using Zingale et al. [2002]

Table 4.3.
Outline of the simulations performed in the scope of this work. In Chapter 5, we mainly discuss simulations from the `delta` generation. The 3D simulations belong to the `echo` generation.

in Cartesian coordinates, or equivalently in polar coordinates:

$$q_{\mathrm{avg}}(r,t) = \langle q(\phi,r,t)\rangle_{\phi}. \tag{4.9}$$

The first panel shows the nuclear energy generation rate: In the initial conditions, the energy rate is at its highest value $\dot{\epsilon}_{\mathrm{nuc}} = 4.4 \times 10^{13}$ erg g^{-1}s^{-1} or $\dot{\epsilon}_{\mathrm{nuc}} = 1.3 \times 10^{16}$ erg cm^{-3} s^{-1} at the bottom of the envelope. This small point is barely noticeable in the heatmap. Already in the first computed timestep, $\dot{\epsilon}_{\mathrm{nuc}}$ drops to a fraction of the original rate. It rises steadily afterward, but never reaches the initial values. In the initial condition, the nuclear energy rate is high in the whole of the envelope, but for the rest of the simulated time, the burning is restricted to a thin layer in the envelope's bottom. The second panel shows the difference between the current and the initial temperature, $\Delta T = T(t)/T_0 - 1$, in percent. With the onset of convection, the hot matter at the burning region streams up with the convective eddies and heats up the envelope. Also evident is a strong cooling of the white dwarf's upper layers (the values are even lower than -4%, but the color scale in Figure A.1 was chosen so as to not lose sight of the warming in the envelope). The green diamonds pinpoint the location of the peak of nuclear energy rate (the maxima in the upper panel). All throughout the simulation, the burning zone lies in a region of lower temperature than initially, possibly explaining the radical drop in $\dot{\epsilon}_{\mathrm{nuc}}$. The WD-envelope transition has wandered a few cells upward. The next panel shows $\Delta\rho = \rho(t)/\rho_0 - 1$ (again in percent). We observe that burning is taking place in a lower density region. Finally, the metallicity enrichment is shown in the last panel. At time $t = 120\,\mathrm{s}$, the mean metallicity in the envelope has risen to $Z_{\mathrm{CNO}} \approx 0.04$ from the initial 0.02.

A more practical way to analyze the state of the nova is by looking at the evolution of its radial profile in ρ–T space. For every radial shell r, the averages $\rho_{\mathrm{avg}}(r,t_0)$ and

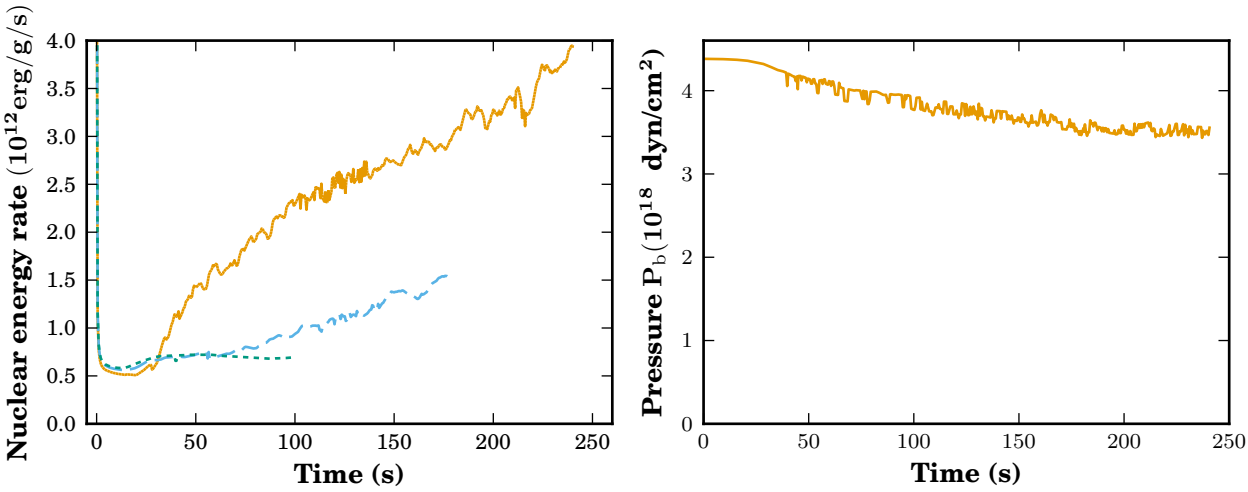

Figure 4.7.
(*Left*) Average of nuclear energy generation rate $\dot{\epsilon}_{\rm nuc}$ in the envelope, for the `delta` simulations. Initially, the rates are larger for the finest mesh with $n_r = 1024$. After a turning point around $t = 20\,$s the relations are inverted and the coarsest mesh, $n_r = 256$, develops the highest values. (*Right*) The pressure at the base of the envelope $P_{\rm b}$ as a function of time, for the simulation Dp256. Within the 240 s of simulated time, the pressure has dropped by approximately 20 %.

$T_{\rm avg}(r, t_0)$ are calculated and marked as points in ρ and T. Figure 4.8 shows the profiles of the three runs with increasing resolution in such a diagram, for the initial conditions at $t = t_0$. In each profile, three segments are clearly recognizable. Starting from the right, with the highest densities and (comparably) lower temperatures, is the white dwarf matter. The sharp rise in temperature and fall in density characterizes the star-envelope boundary. In the accreted envelope, density and temperature fall monotonically. Recall that in these simulations, when calculating HSE, the temperature is fixed for each grid cell and the density is calculated from the EOS (see Section 4.2.2). Therefore, when comparing nearby sections of the curves, points along an isothermal are also at the same radius on the grid. There are systematic discrepancies in the envelope and core among all three setups: the density is consistently lower in the coarser meshes. These differences are stronger at the interface. Panel (*b*) shows a detail around the peak of temperature. The small jump in temperature stems from the ignition perturbation applied to the cells just above the interface. The scatter points are color-coded to visualize the strength of nuclear burning. It is clearly observable that more energy is released in the finer resolution meshes, due to the higher densities at equal temperatures, in part explaining the trend seen in Figure 4.7.

Figure 4.9 again shows the nova models in the ρ–T space, focusing on the core-envelope transition. To observe their evolution in time, we track the position of the two most important layers: the layer of maximum temperature –sometimes called the *maximum shell source temperature* and the layer of maximum nuclear energy release

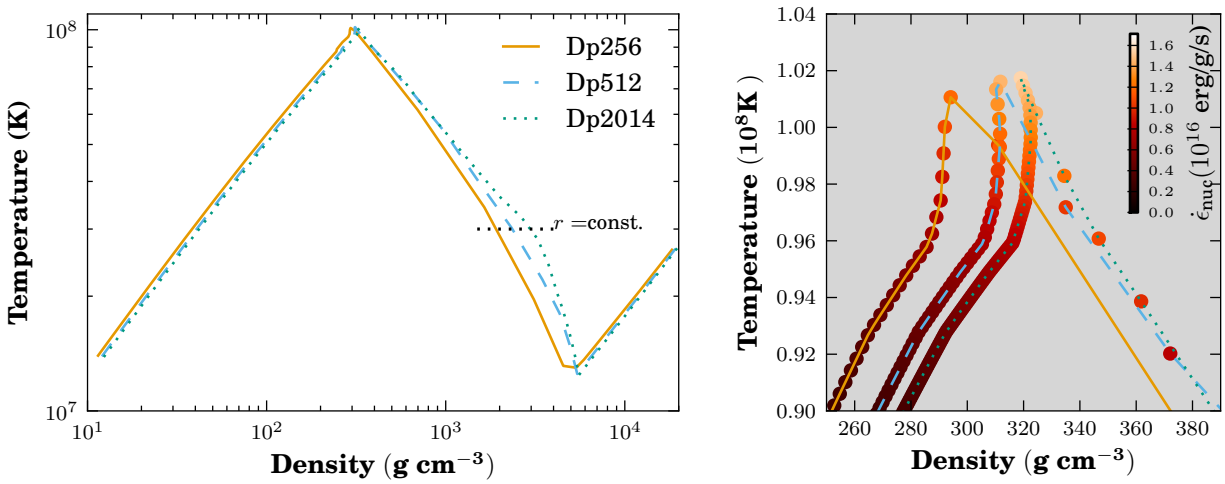

Figure 4.8.
Initial thermal state of the atmospheres in the `delta` runs. (*Left*) For each radial row in the grid, the mean density is plotted against mean temperature, Equation (4.9). In this ρ–T space, the stratification shows a characteristic Z-shape. The lines with positive slope correspond to the envelope and white dwarfs respectively, while the section with $\partial T/\partial\rho < 0$ corresponds to the transition region. There, the differences between the initial conditions of the three runs is more evident. The (*right panel*) figure shows a detail around the bottom of the envelope. The rate of nuclear energy generation is superposed as a scatter plot; the color scale indicates the magnitude.

(*burning shell*):

$$T_{\rm ss} = \max\left(T_{\rm avg}(r,t)\right) \tag{4.10}$$

$$\dot{\epsilon}_{\rm bs} = \max\left(\dot{\epsilon}_{\rm nuc,avg}(r,t)\right). \tag{4.11}$$

These layers are shown with *orange* and *blue* markers, respectively. The opacity visualizes the change in time, darker meaning later time steps. The first and last states of the atmosphere are drawn for reference as dashed and full black curves, respectively. The five-pointed stars pinpoint the first and last ρ-T coordinates of the burning zone. In the simulations `Dp256` and `Dp512`, we recognize a similar general trend: the interface and envelope drop in density; for `Dp1024`, density rises at the interface. Most important is the observation that the burning shell $\dot{\epsilon}_{\rm bs}$ generally does not coincide with the point of $T_{\rm ss}$. They are only identical for the initial conditions (*golden star*), yet generally the burning zone lies at lower temperatures and higher densities, a few layers deeper into the white dwarf. Instants after the start of the simulations, the burning zone shifts to significantly lower layers with $T = 0.8 \times 10^8$ K and progressively moves to higher T and lower ρ. We will see that this drop is not owed to a shift in pressure equilibrium, but due to the swift consumption of particular nuclei as fusion fuel. From the atmospheric profiles it is evident that the area in ρ-T space between the initial and final states drops as resolution rises. Also, the path that the burning shell $\dot{\epsilon}_{\rm bs}$ traverses through this space is simpler in the higher resolution cases. In Dp256, it moves along a jagged curve up until almost merging with the point

of maximum temperature, explaining the overall increase in $\dot{\epsilon}_{\rm nuc}$ for this run. Dp512 displays an oscillating burning zone that almost reaches $T_{\rm ss}$, but seems to converge at slightly lower temperatures. Dp1024 shows much quieter behavior. The burning zone drops instantly to $(\rho, T) = (500\,{\rm g\ cm^{-3}}, 0.8 \times 10^8\,{\rm K})$ and steadily moves upward again, never reaching such high temperatures as Dp256 in roughly the same simulated time.

The upper boundary of the computational domain in the `delta` and `echo` runs allows for outflow. An initial guess for the reason behind the quiet burning was pressure loss due to mass loss through the upper boundary, seen in Figure 4.7. However, the mass loss and drop in pressure are stronger for the coarsest mesh. Therefore, the outflow through the boundary cannot explain the lower convective efficiency. So far we have considered density, pressure and temperature. The remaining two factors which play a role in the CNO-burning cycle are the amounts of fuel $X(^1{\rm H})$ and of the catalyzing nuclei $Z_{\rm CNO}$ (Section 2.2.3). Indeed, the reason behind the sudden drop of $\dot{\epsilon}_{\rm nuc}$ in the first seconds of our simulations is due to the fast consumption of $^{15}{\rm N}$ in just fractions of a second. The reaction $^{15}{\rm N}(p,\alpha)^{12}{\rm C}$ was responsible for most of the energy release in the initial conditions. We defer the discussion of nuclear reactions to the Results chapter (Chapter 5).

The power of the nova flash depends strongly on the amount of $^{12}{\rm C}$ available in the burning zone. As the CNO elements are being consumed, a continuous supply of $^{12}{\rm C}$ must come from the white dwarf to sustain the TNR. Some sort of 'dredge-up efficiency' must be responsible for the flow of $^{12}{\rm C}$ into the envelope and therefore for the success of the nova flash. We are interested in the factors that influence this efficiency.

Consider Figure 4.10, which shows the various contributions to the Brunt–Väisälä frequency N^2. In Section 4.2.2 and Figure 4.1, we explained that in the second integration of hydrostatic equilibrium, we constrained $N^2 < 0$ to the bottom of the envelope. Figure 4.10 shows that N^2 is indeed negative around that region, even if not exactly at the same position across the three simulations. More importantly, the value of N^2 is much lower for the coarser resolutions. This is due to the integration errors explained in Figures 4.2 and 4.8. Specifically, the adiabatic gradient $\nabla_{\rm ad}$ is consistently higher for higher resolutions, $\nabla_{\rm ad,Dp256} < \nabla_{\rm ad,Dp512} < \nabla_{\rm ad,Dp1024}$. Consequently, the ratio between the real and adiabatic gradients $\nabla/\nabla_{\rm ad}$ decreases, as does the power of convection. This could be the physical reason behind the lower overall values in Mach number, metallicity enrichment and nuclear energy rate, instead of a resolution effect.

Another factor affecting the dredge-up efficiency is the stiffness of the convective boundary. By 'stiffness', the permeability of the stable layer to overshooting streams from the unstable region is meant. A smooth boundary allows streams to trespass the formal convective boundary, deep into the stable region, unlike a stiff boundary, which behaves more like an impenetrable wall. Freytag et al. [1996] analyzed shallow surface convection zones in models of A-type stars, solar-like stars and cool DA-type white dwarfs. They found that in all of those cases, the convective motions breach the convective boundary. The radial velocities of the downdrafts decay exponentially as they penetrate into the stable region. Meakin & Arnett [2006] studied simultaneous carbon- and oxygen shell burning in a late $23\,M_\odot$ star. In this case, there are abrupt

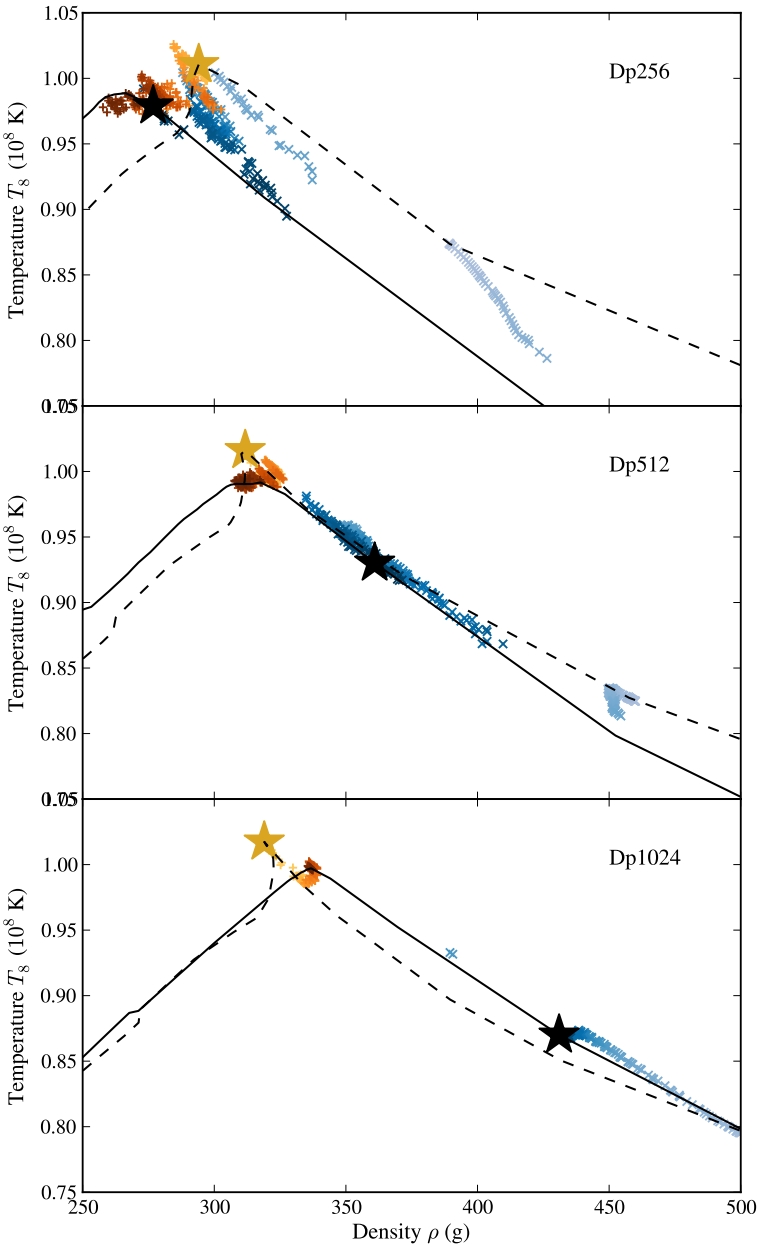

Figure 4.9.
Tracks in ρ-T space of two critical layers of the novae: the hottest zone (*orange*) and the burning layer (*blue*). The initial and final points of the red track are signaled by the golden and black stars respectively. For reference, the initial (*dashed*) and final (*full*) states of the atmosphere are drawn as black lines. The opacity of the colored tracks serves to visualize time – darker means later.

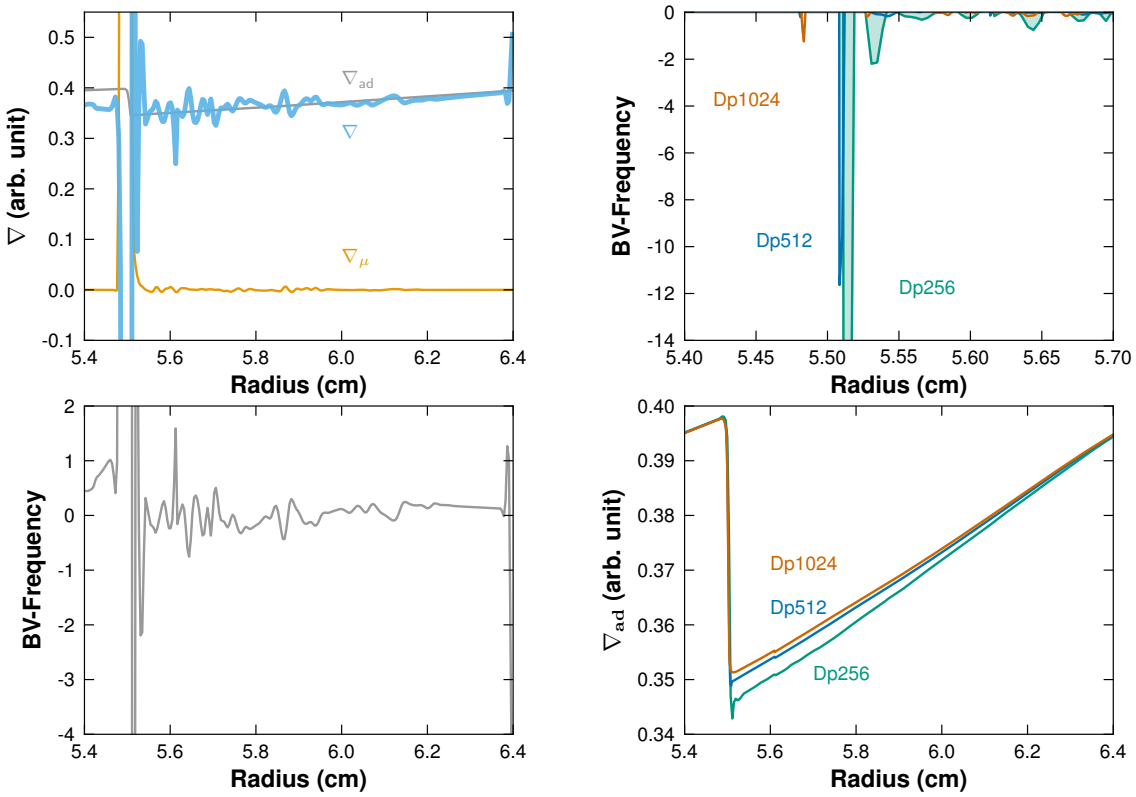

Figure 4.10.
The different components of the Ledoux criterion, $\nabla < \nabla_{\rm ad} + \frac{\phi}{\delta}\nabla_\mu$. The composition gradient everywhere is smaller than the actual gradient ∇, and near zero, except at the transition region ($r \approx 5.5 \times 10^8$ cm). The gradient $\nabla_{\rm ad}$ has around the same magnitude as ∇. Where $\nabla > \nabla_{\rm ad}$, the envelope is super-adiabatic, and the Brunt–Väisälä frequency becomes $N^2 < 0$. The last panel shows N^2 for the initial conditions of the three `delta` simulations. The value of N^2 is lower for lower resolutions. Specifically, the adiabatic gradient $\nabla_{\rm ad}$ is consistently higher for higher resolutions and therefore, the superadiabaticity is lower.

composition gradients at the convective boundaries, which result in equally steep density gradients and large spikes of the buoyancy frequency. N^2 is regarded as a measure of stiffness of the boundary. In the regions where it spikes, the adjacent convective motions give rise to density perturbations, but the overshoot of convective plumes is minimal. Similarly, in simulations of He-shell flash convection [Herwig et al. 2006], the convective region is bounded by very stiff gradients. The velocities decay exponentially into the stable layer, but the decay already starts in the convective region. The overshoot is even smaller than in O-shell convection. In the stable regions, the velocity amplitudes are dominated by g-modes, excited at the boundary by the convective motions. The velocity field in the stable zone, and with it the mixing, is a superposition of exponentially decaying overshooting streams and g-mode oscillations. In the shallow surface regions of Freytag et al. [1996], no g-mode excitation was found, probably due to the smoothness of the convective boundary. In another set of simulations of O-shell burning [Meakin & Arnett 2007], the position of the boundary

is measured by the gradient of the oxygen mass fraction. The convective region is bounded in its floor and ceiling by stable regions. Each boundary has vastly different values of N^2: the bottom has a very sharp spikes in N^2; the top displays only a small bump. In Figure 4 of Meakin & Arnett [2007], the decidedly distinct behavior of both boundaries becomes evident. While the bottom boundary remains practically static, the upper boundary is seen to migrate into the stable layers.

Stable strata with an adjacent convective or turbulent layer are common on geo- and astrophysical flows. The process by which the turbulent layer 'diffuses' into the stable layer and the boundary recedes, expanding the extent of the turbulent region, is called *entrainment*. Its rate is a function of the *bulk Richardson number*, defined as [Meakin & Arnett 2007]:

$$\mathrm{Ri_B} = \frac{\Delta b L}{{v_{\mathrm{rms}}}^2} \tag{4.12}$$

Here, Δb is the buoyancy jump across the boundary, v_{rms} the rms turbulent velocity along the interface and L the length scale of the turbulent motions. The relative buoyancy is defined by the integral of the buoyancy frequency across the boundary

$$b(r) = \int_{r_i}^{r} N^2 dr. \tag{4.13}$$

Meakin & Arnett [2007] find values of $20 \leq \mathrm{Ri_B} \leq 420$ in their O-shell convection boundaries.

If the stiffness of a boundary and with it the impenetrability of overshooting plumes depends on the buoyancy jump Δb, then this argument lends credence to the discussion regarding the shape of the Brunt–Väisälä frequency in Figure 4.10. The integral N^2 will clearly be the largest in Dp256.

4.5. A model from a stellar evolution code

In the overwhelming part of our studies, a modified version of the Kercek model (Section 4.2) was used as initial conditions for the multi-D simulations, the "Würzburg model'. Of course, a comprehensive study of novae explosions should examine a variety of models: different progenitor white dwarfs masses, envelope compositions, etc. In order to build our own models we employed the freely available stellar evolution code *MESA* (Modules for Experiments in Stellar Astrophysics, Paxton et al. [2011, 2013]). *MESA* is written in a modular fashion, where one module is responsible for the nuclear network, another for the EoS, etc. The main module, `star`, combines the necessarily modules to run a full stellar evolution calculation. *MESA* comes with an array of test problems ready to use and experiment with. We used the test problem `WD`, which simulates the ignition of a hydrogen shell burning in a $1_{\odot}$ WD, and modified it to be similar to our Würzburg model. The solar-composition accretion rate was changed to $5 \times 10^{-9} M_{\odot} \mathrm{yr}^{-}1$ and we used the same criterion for choosing the moment when to stop the 1D simulation and map to 2d. Specifically, the peak temperature in the envelope should be $T_{\mathrm{ss}} = 1 \times 10^8\,\mathrm{K}$.

A handful of multi-D simulations based on these initial conditions were tested. However, there were many uncertainties about the quality of the model in regard to

the smoothing and interpolation of the data. Here we will only point out Figure 4.6. It shows how small deviations in T and ρ lead to large fluctuation in the nuclear energy rate.

Further numerical experiments with *MESA* initial conditions were abandoned. These were later carried out by Florian Lach [Lach 2016].

4.6. Validation tests

4.6.1. `alpha`: proof of concept

In the early stages of the present work, before engaging in all the detailed model-building steps (Sections 4.2 and 4.3), a quick approach was taken to test the feasibility of nova simulations in our code. Taking figures in Kercek et al. [1998, 1999] as an example, the radial profile of the temperature was mimicked with a combination of analytic functions: a hyperbolic tangent for the star–envelope transition, and a linear function for the envelope. The peak temperature is fixed at 1×10^8 K, as in the paper. The white dwarf consists of carbon and oxygen in equal parts, the envelope is mostly hydrogen, although at this stage the exact mass fractions of the individual species was not taken into account. The hydrostatic equilibrium is integrated. The result, model `alpha`, is shown in Figure 4.11.

In this set of simulations, the grid geometry is always Cartesian and the lateral boundary conditions are periodic. The bottom boundary of the box towards the center of the star is reflective. We vary two parameters in order to study the impact of the choice of the upper boundary condition on the results: the kind of boundary and the height of the box. The types of boundary tested were *wall*, *hystat-wall* and *constghost* (see Section 3.1.4). To limit the effects of the upper boundary on the burning region, the height of the box can be made larger. In one case, the height of is $\Delta y = 1000$ km, the second $\Delta y = 1500$ km. The height is increased by 50%, and keeping the cell sizes intact, the number of cells increase from $n_x = 128$ in the *short* box to $n_x = 192$ in the *tall* box. Table 4.4 lists the characteristics of the `alpha` models.

In the original Kercek model, convective movements start just seconds after the start of the simulation, as the stratification in the 1D data is already unstable to convection. In the `alpha` model, although we have the same $T_b = 1 \times 10^8$ K, the temperature gradient from the analytical functions is smaller than in the original and the stratification is initially stable against convection. The constant heating from nuclear reactions raises the peak temperature at the base and makes the temperature gradient steeper, until the stratification becomes super-adiabatic. This happens after approximately $t \approx 80$ s. Figure 4.12 shows the evolution in time of some key quantities of the simulations: the critical pressure P_b and source shell temperature T_{ss}, both horizontally averaged, and the mean Mach numbers. Observe the steady rise in pressure and temperature until $t \approx 80$ s. When convection ensues, cold CO matter rises to the envelope and lowers the temperature, after which the temperature rises again due to nuclear energy release.

The base pressure P_{b} in the simulations with the fixed upper boundary 'wall' is substantially higher than with the constant ghost cells. The end of the curves at $t \approx 200$ s are due to the code crashing. Typically this results from values outside of

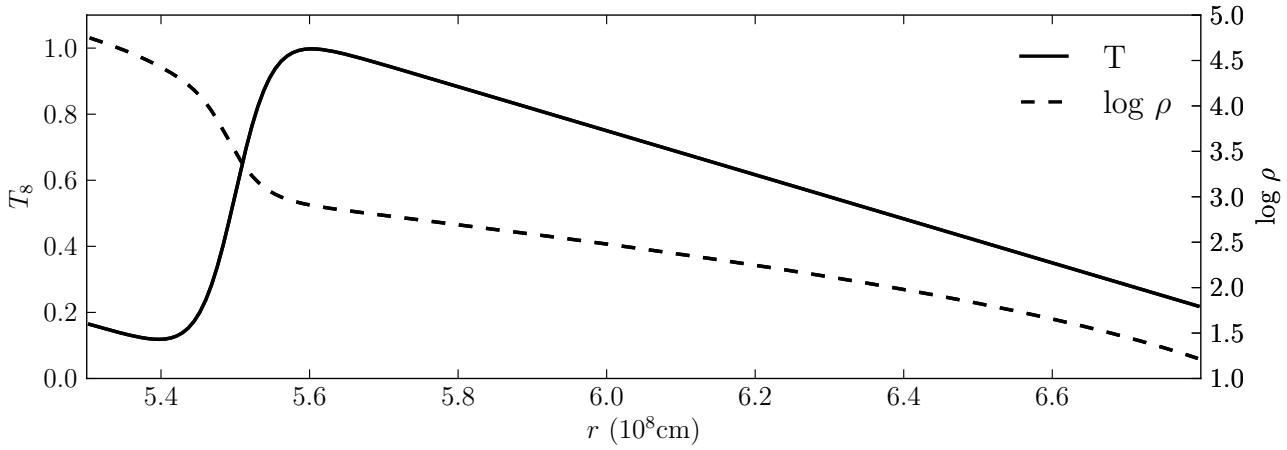

Figure 4.11.
Initial temperature and density in the `alpha` model. The curves mimic the values from the Kercek et al. [1998] with analytic functions. The transition from white dwarf to envelope is much smoother than in the original model.

the tabulated Helmholtz EoS. Both simulations with the constant ghost cells boundary continue for several hundred seconds. However, they do not achieve such high energy generation rates, temperatures or velocities.Glasner et al. [1997], Kercek et al. [1998] and Kercek et al. [1999] all find that the peak temperature during runaway lies at about $T \sim 2.0 \times 10^8$ K. Recall that Kercek et al. use a boundary with outflow, while the simulations in the Glasner group have an ALE grid. It is natural that in our simulations with closed upper boundary, the temperature rises above this, reaching even $T \gtrsim 2.5 \times 10^8$ K in individual cells. The runs with constant ghost cells do not quite reach this threshold, because the pressure at the bottom of the envelope is decreases after reaching maxima before $t = 200$ s. They eventually go into a state of steady burning at a temperature $T_b \sim 1.3 \times 10^8$ K. In all simulations the, flow remains subsonic. Again, with fixed upper boundaries, the values are greater, nearing M ~ 0.8 in individual cells (the mean value does not surpass M ~ 0.25), while constant ghost cells yield and average Ma ~ 0.1.

In summary, a fixed upper boundary yields curves comparable to the ones found in past works: steady growing $\dot{\epsilon}_{\mathrm{nuc}}$ in a time scale of 2×10^2 s. In our case, even higher temperature values than in the literature are reached. Nevertheless, these boundaries do not represent the conditions in the stellar atmosphere realistically, and it will not be used in the future cases. We will perform all of our simulations with the constant ghost cells, despite some drawbacks that will be discussed in Chapter 5. In addition, the pressure in the simulation with the taller box decreases to a fraction of its initial value.

4.6.2. `bravo`: test of perturbations

Starting from the second generation of our models, `bravo`, we used the Würzburg model described in Section 4.2. Because our models are at $t = 0$ already convectively

Parameters of the `alpha` models

Model name	Cells		Box height	Boundary conditions		
	n_x	n_y	(km)	lateral	lower	upper
Ac192.wl	320	192	1500	periodic	wall	wall
Ac192.cg	"	192	1500	"	"	constghost
Ac128.wl	"	128	1000	"	"	wall
Ac128.cg	"	128	1000	"	"	constghost

Table 4.4.
Overview of the `alpha` models. The number of cells in the vertical direction was varied, as well as the upper boundary condition.

unstable, convection plumes should arise after only a few seconds. To break the symmetry of 1D atmosphere simply extended to 2D, a tiny momentum in each spatial dimension is added to each cell in the grid, with randomly generated amplitudes. The simulations of the Glasner group do not add any perturbation, as the intrinsic machine rounding errors suffice them. We found in early tests, that in our simulations errors on the machine-level precision are not enough, and the flow develops plumes that are perfectly symmetric if the simulation box has lateral periodic boundary conditions. [Kercek et al. 1999] choose some cells in one layer directly at the interface and enhance their temperature by 1%. In the 3D case [Kercek et al. 1999], to save computation time, they perturb 10 cells to have a larger ignition surface. All publications from the Kercek, Glasner and Casanova groups claim that any information about the initial perturbation is lost after a couple of seconds of the simulations, and that the result is independent of it. Nevertheless, we conducted a series of tests to assess the dependence of our solution to initial perturbations. In `bravo`, as in `alpha`, all simulations were performed in the plane-parallel approximation, using periodic boundary conditions at the lateral borders.

In an initial test, a small area in the horizontal center is perturbed with 10% higher pressure. Although 10% may be a rather strong amplitude, this was done to have the largest effect in the shortest time possible. In a resolution of 512×256, a quadratic area comprising four cells at the core-envelope interface were perturbed, while in a second run with twice the resolution, 16 cells occupying the same physical area were perturbed.

Figure 4.14 shows a detail of the simulations around the interface at three different times. Plotted is the Mach number in a logarithmic scale. The left column shows the coarse resolution snapshots (a), the right one the fine resolution run (b). The first panels, at $t \sim 2\,\mathrm{s}$, show the location of the perturbation at the horizontal middle of the interface plane. The other time steps were chosen as follows. The second row shows the moment in which the smallest plumes arise even at the farthest point away from the perturbation. In the last row the whole burning region above the interface is convective. With finer resolution, convection plumes start much faster ($\sim 10\,\mathrm{s}$ compared to $\sim 45\,\mathrm{s}$). Also, the point where the whole bottom of the envelope is convective is reached sooner, after only 30 s. The convective eddies become also

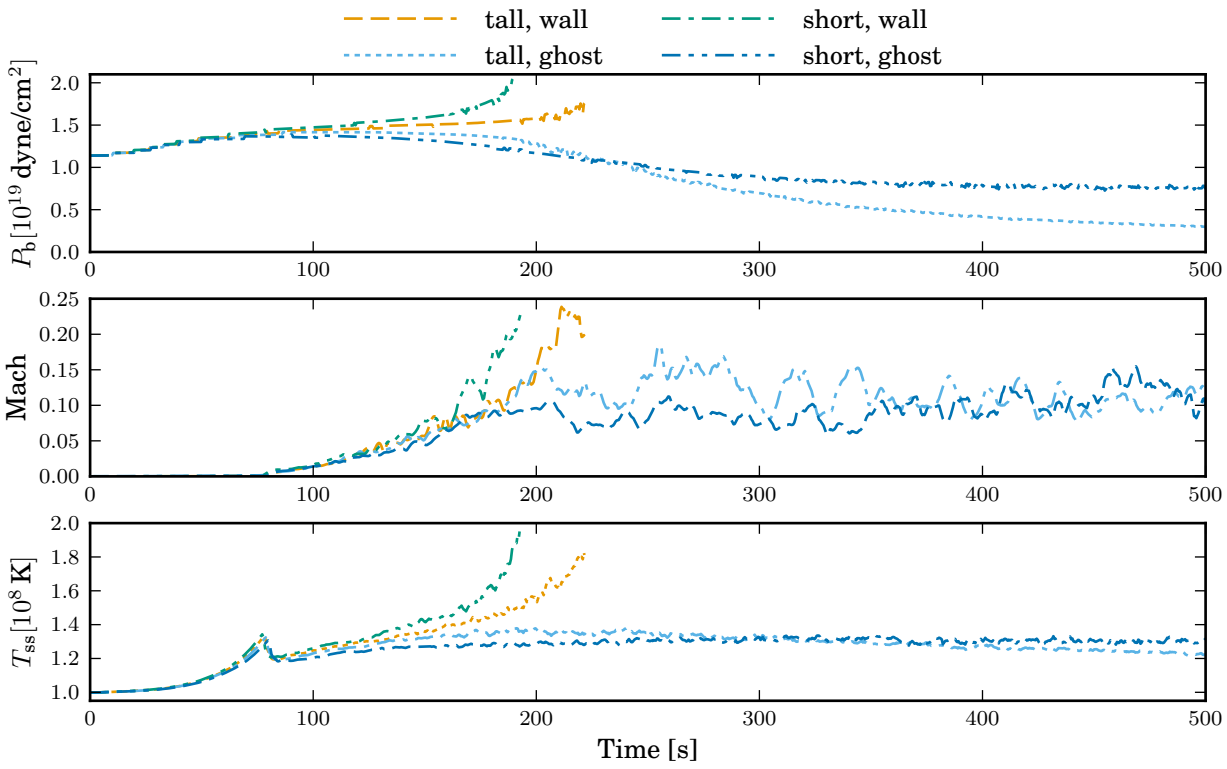

Figure 4.12.
Time evolution of the `alpha` simulations, listed in Table 4.4. The simulations with the closed boundary condition 'wall' barely reach 200 s. They reach very high pressures and temperatures, and eventually values outside of the tabulated EoS, which terminates the simulation. The simulations with constant ghost cells ran for up to 700 s, but in neither case can they sustain the base pressure P_b.

smaller with finer resolution.

A perturbation with sinusoidal amplitude in the lateral direction and a Gaussian form in the vertical one was also tried out. As in the previous case, the information about the perturbation does not survive a couple of convective turnover times. For the rest of the production runs, only the simplest form of the perturbation – tiny random momentum in each cell – was employed.

4.6.3. Box width

In our multi-D simulations with 2D polar (and subsequently in 3D spherical) coordinates, a fairly narrow arc of the star's surface is modeled, usually an angle of around $\phi \approx 0.06\pi$ with an arc length of $W \approx 1000$ km. Expanding the horizontal extension of the domain pushes the lateral boundaries apart. This reduces possible boundary effects on the solution, but slows down the computation due to the increased number of cells. In the following test, the `delta` profile is used to set up the nova, in a box with $W = 2000$ km (a) and a box with twice this width (b), see Figure 4.15. [4] This

[4] In Kercek et al. [1998, 1999] the width of their plane-parallel box was $W = 1800$ km, in Glasner et al. [2007] they used slices in polar coordinates with a base of $W \approx 1680$ km and $W \approx 840$ km,

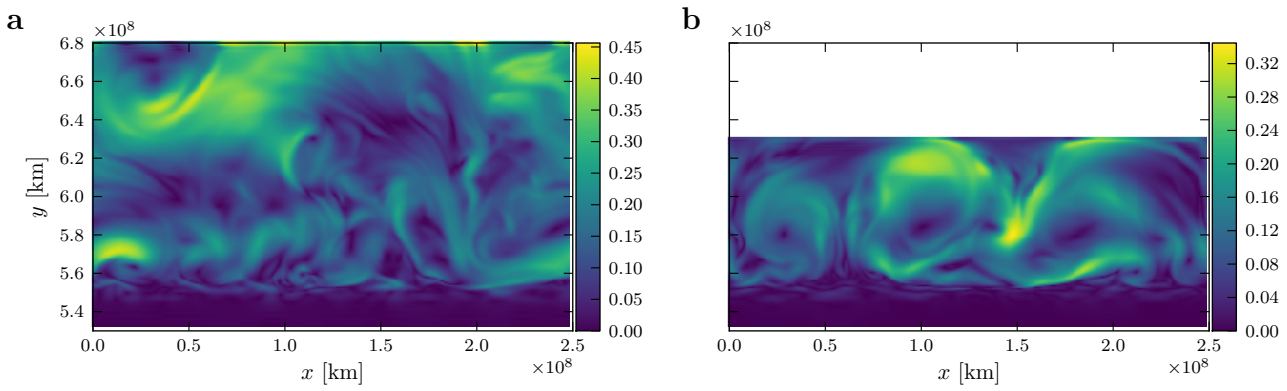

Figure 4.13.
Snapshots of two `alpha` simulations – (*a*) Ac192.cg and (*b*) Ac128.cg – comparing the effects of the effects of the box size. The cell sizes in both setups is equal, but (*b*) has a smaller vertical extension, see Table 4.4. Shown is the Mach number.

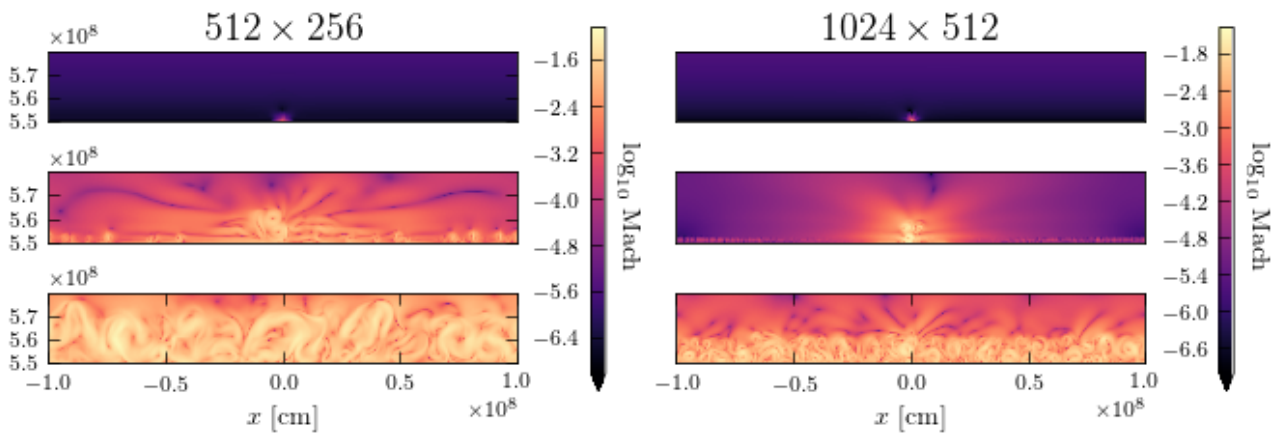

Figure 4.14.
Two `bravo` simulations with a strong perturbation in the initial conditions at the interface's center. Any sign of the initial perturbation is lost after a few seconds. Shown is only a detail just above the envelopes base (r =5.5×10^8 cm – 5.8×10^8 cm). The left column corresponds to a resolution of 512×256, the right to 1024×512. Shown is the log of the Mach number, note that the color bars have different scales, as the mean Mach numbers in the higher-resolution case are smaller. Also, the convective eddies decay into smaller scales, and the enrichment from CO matter into to the envelope is slower.

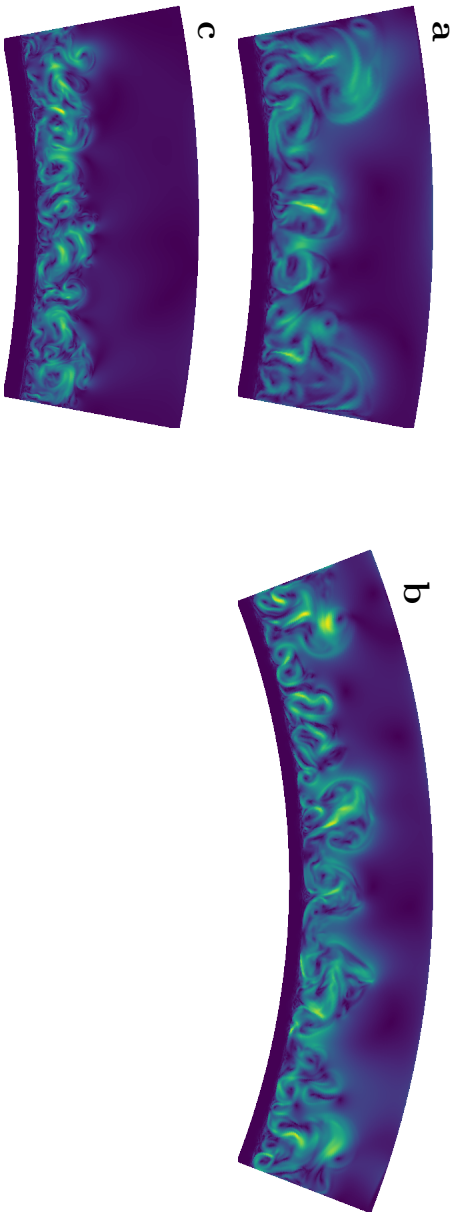

Figure 4.15.
Mach number in simulations testing the effect of the lateral extension of the box. These belong to the `delta` generation of our models (see Table 4.3). (*a*) $W = 2000\,\mathrm{km}$ with resolution 512×256, (*b*) $W = 2000\,\mathrm{km}$ with resolution 512×256, (*c*) $W = 4000\,\mathrm{km}$ with resolution 1024×512.

is done in two resolutions 512×256 and 1024×512. Figure A.2 shows the global maximum of the temperature T_8 in the simulations as a function of time. In the roughly 90 s of simulation time, basically there is no difference in the mean values. This indicates that $W = 2000$ km is an appropriate width, and that extending it does not purvey more accuracy to the result. At this width, a handful of large eddies fill the envelope. $W = 2000$ km is the width of the `Dp256` simulation discussed in length in Chapter 5.

An example of a simulation with a higher resolution, 1024×512 and $W = 2000$ km, is also shown in Figure 4.15 panel (c). As in the `bravo` simulations, the increased resolution allows to resolve finer structures, and even more eddies fill the box. However, a simulation with a corresponding wider box of 2048×512 and $W = 4000$ km was not carried out for comparison.

For the set of simulations `echo`, a shorter width of $W = 800$ km was chosen, in order to have a simulation box in 3D with similar dimensions to that of Casanova et al. [2011]. Convective eddies generally appear in pairs, and the box size should be at least as wide as the diameter of two eddies [Hillebrandt, private communication]. The width in the `echo` simulations is enough to fulfill this condition.

and Casanova et al. [2011] had a box with $W = 800$ km.

5. Results

The previous chapter dealt with the details of the simulation setup: the region of interest, the discrete mesh and interpolation methods, and the sensitivity of the numerical solution on several parameters. We now turn our attention to the physical interpretation of the results of selected simulations. We are interested in the interplay of convection, mixing, the energy release from the nuclear reactions of the CNO cycle and the resulting modification of the envelope's atomic composition. In Section 5.1, we describe the general properties of the convective flow. Section 5.2 presents a detailed analysis of the individual nuclear reactions contributing to the total thermonuclear energy rate.

5.1. Morphology of the convective flow

In this section, we discuss the results from the simulation Dp256 (polar coordinates, 256 cells of vertical resolution), which we ran for 240 s.

Around $t = 10\,\mathrm{s}$ after the start of the simulation, buoyant plumes rise from the base of the envelope all along the interface. The gas at the bottom of the envelope becomes hotter and lighter than the layers above, becoming Rayleigh-Taylor unstable. Minuscule random fluctuations in momentum at the grid level serve only to break the lateral symmetry. In less than 30 s, the 'mushroom caps' of these plumes reach a height of about one pressure scale height and farther. At this height of the envelope, the gas temperature is down to $T = 65\,\mathrm{MK}$ from the 100 MK at the base, and the plumes start to fragment from cool streams flowing down their sides. Figure 5.1 shows the morphology of the flow with contours of the mass fraction $X(^{12}\mathrm{C})$. The plumes carry carbon-rich material to the envelope. Most of the $^{12}\mathrm{C}$ is concentrated along inner, denser filaments of the plumes with mass fractions $X(^{12}\mathrm{C}) \sim 7 \times 10^{-3}$, ten times higher than the mean mass fraction $\sim 7 \times 10^{-4}$ of the surroundings. At $t = 30\,\mathrm{s}$, some of it has reached heights of over $2\,H_P$, yet in very small concentrations: the last contour line in Figure 5.1 has a value of 1×10^{-4}.

The plumes first reach the upper boundary of the box shortly after the 30 s mark; convective eddies fill the envelope in its entirety from around $t \sim 40\,\mathrm{s}$ onwards. The structures in our simulation are markedly distinct from those of Kercek et al. The flow is highly irregular. It does not display the multiple, stable and isolated vortices of Kercek et al. [1998, Fig. 1]. Instead, the dozen initial plumes merge into circular vortices, the largest having a diameter of about a pressure scale height. Only about two of these large vortices exist simultaneously at any given time. A handful of smaller vortices circulate between them in erratic trajectories, intermittently merging into larger eddies, creating new ones and destroying previous ones. The mean convective velocities are on the order of $\sim 11 \times 10^6\,\mathrm{cm\,s^{-1}}$. With eddies of half the size of the envelope, this translates into a convective time of about $\tau_{\mathrm{conv}} \sim 4\,\mathrm{s}$. Higher peak values are reached when the fluid streams downwards and collides with other eddies or against the interface. These values are in agreement with those in Glasner et al. [1997], who

find velocities of a few $\sim 10^6\,\mathrm{cm\,s^{-1}}$ in the slow phase (and up to $\sim 5 \times 10^7\,\mathrm{cm\,s^{-1}}$ in the fast phase).

The mean Mach number grows almost monotonically for the first 41 s, when it reaches a local maximum of Ma = 0.4. For the rest of the simulation, the mean Mach number varies between $0.09 < \mathrm{Ma} < 0.15$, with an overall temporal mean of $\overline{\mathrm{Ma}} \approx 0.12$. The instantaneous maximum Mach numbers are much higher; at the same $t = 41\,\mathrm{s}$, the value is $\max(\mathrm{Ma}) = 0.39$. With a much larger scatter than the mean numbers, the maximum values grow from 50 s to the end of the simulation from Ma = 0.3 to 0.5. The flow remains subsonic throughout the length of the simulation, in agreement with the other simulations of 2D nova envelopes.

Panel (*b*) in Figure 5.1 shows a snapshot of the ^{12}C mass fraction at a later time. The contours in this diagram go from $X(^{12}\mathrm{C}) = [0.01, 0.1]$ in 50 steps. At this point, the envelope is fully convective. We find individual bubbles and filaments of high carbon content in the eyes of the vortices that survive for several tens of seconds, until they eventually merge into the background as the vortices are deformed through collisions with the neighboring vortices. At the base of the envelope, no clear trace of symmetric, easily identifiable plumes or 'mushrooms' is left. The convective eddies, extending in diameter from the base of the envelope to over $1\,H_p$, warp the upcoming streams of WD matter as soon as they reach the surface. By shoveling the dense filaments of WD matter up to higher layers away from the burning zone, the carbon bubbles are saved from destruction by proton capture. Panel (*b*) also reveals a fault in our numerical setup. The upper boundary of the simulation box is set with 'constant ghost cells', such that the values of nuclear composition are fixed on those cells. Inflow from the boundary is allowed, so that when the largest eddies induce currents that reach up to the highest row of cells, material from the ghost cells streams downwards with fresh, unprocessed, solar composition. This is seen as the void area at the upper boundary in panel (*b*), where the contours accumulate until the lowest value is reached. In the uppermost layers of the envelope, the bulk of energy generation stems from beta decays. This intermittent inflow of solar matter leaves a trace in time-profile of energy generation rate in Figure 5.7. The drop in metallicity in the upper envelope is seen as dark patches, a behavior that is mirrored in the heatmap of nuclear energy rate.

Figure 5.2 shows the radial structure of our WD-envelope simulation. The *solid lines* are the laterally averaged quantities, also averaged in time over two convective turnover times: ($\tau_{\mathrm{conv}} \sim 8\,\mathrm{s}$)

$$q_{\tau_{\mathrm{conv}}}(r) = \overline{\langle q(\phi, r, t)\rangle}. \tag{5.1}$$

To give a sense of the fluctuations, the maximum and minimum values per layer, averaged over the same period are shown:

$$q_{\tau_{\mathrm{conv}}}(r) = \overline{\max\langle q(\phi, r, t)\rangle} \tag{5.2}$$

The shear flow at the WD-envelope transition induces strong fluctuations in temperature. While the mean value for the period $150\,\mathrm{s} < t < 180\,\mathrm{s}$ has not risen from the initial $T_{\mathrm{ss}} = 1 \times 10^8\,\mathrm{K}$, individual cells at the base of the envelope reach peak values of over $1.4 \times 10^8\,\mathrm{K}$. These fluctuations lead to even stronger fluctuations in the energy generation rate. All over the extent of the atmosphere, we find fluctuations in

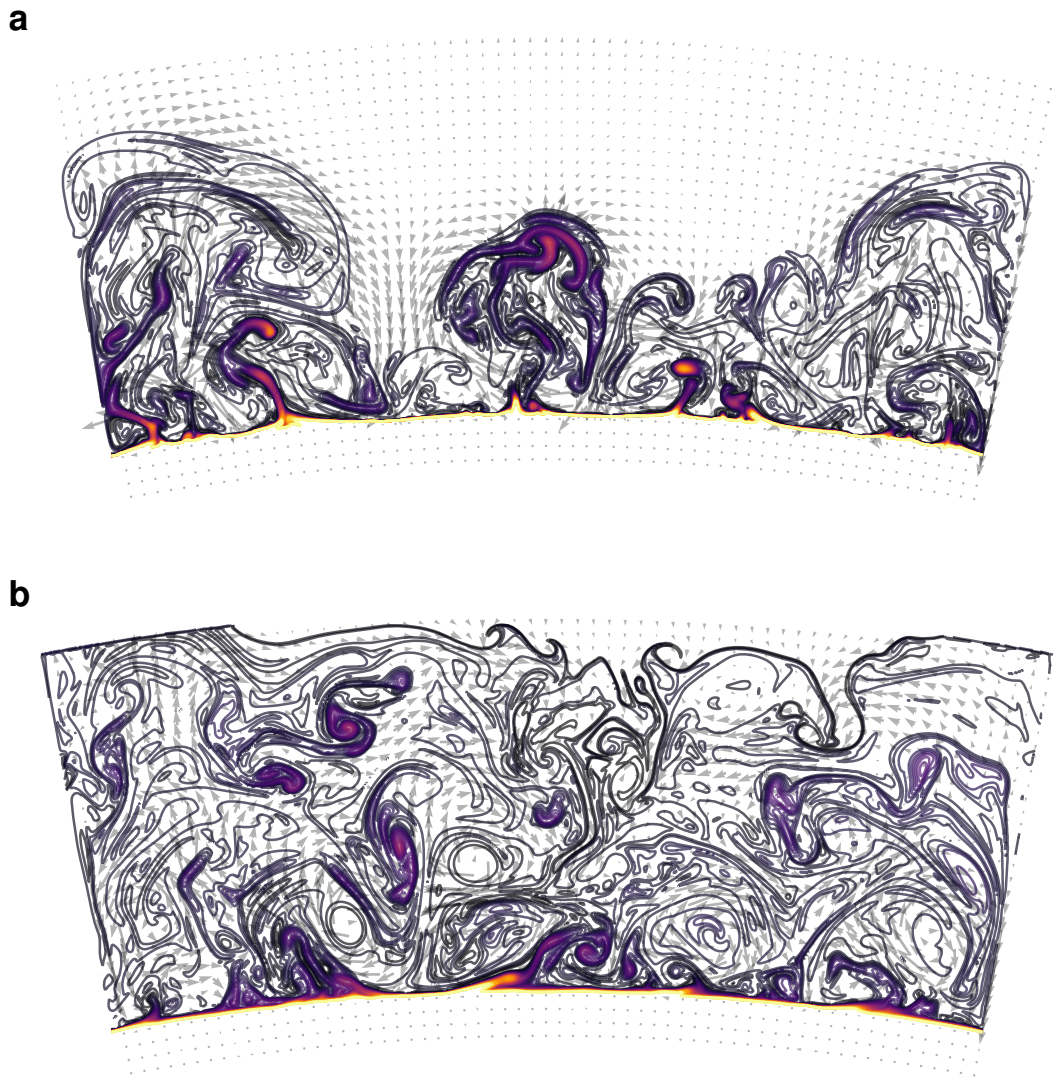

Figure 5.1.
Two snapshots of the simulation Dp256. (*a*) Fifty contour lines show the mass fraction of ^{12}C from 10^{-4} to 10^{-2} in equal steps. The vector field shows the fluid velocities. At $t = 30$s the first convective bubbles bring carbon rich-material from the interface to heights comparable to one pressure scale height. Some material reaches almost the box height, but in very small concentrations. (*b*) At $t \sim 130$s ^{12}C is present in all the envelope. The highest concentration of ^{12}C remains in small bubbles and filaments. The contours sample 50 values between 10^{-2} and 10^{-1}.

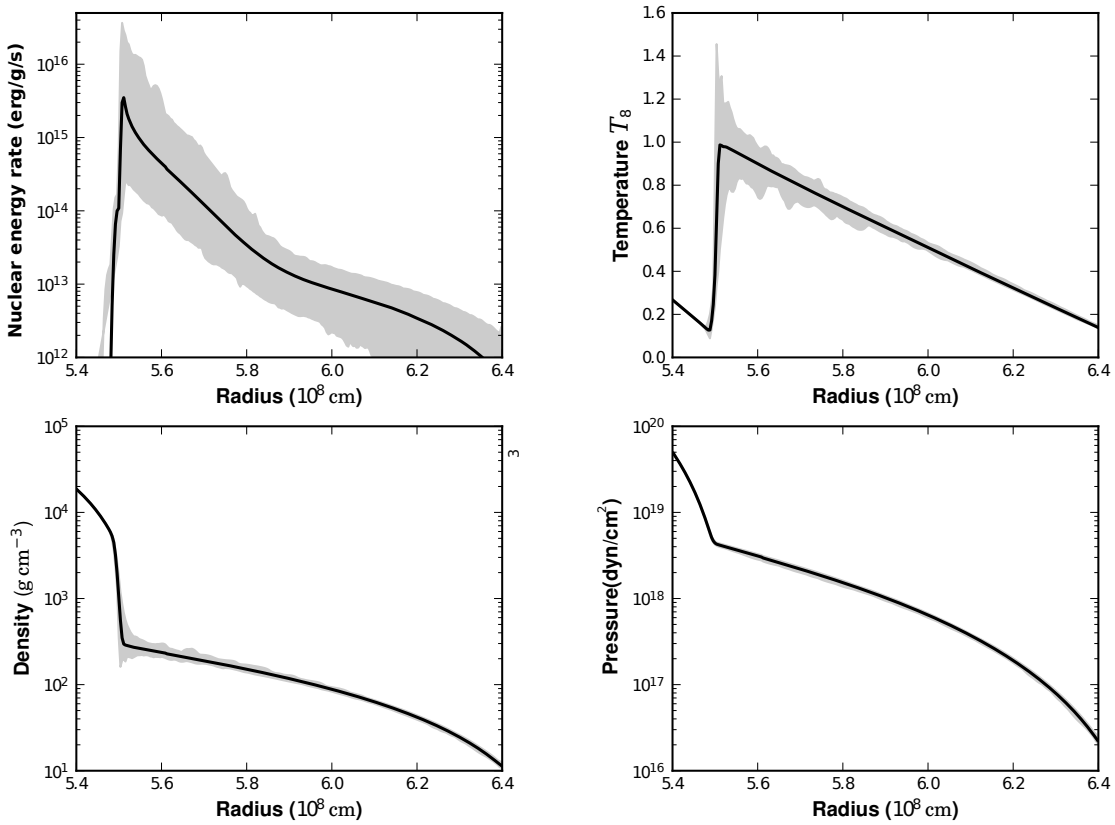

Figure 5.2.
Profiles of $\dot{\epsilon}_{\rm nuc}$, T, ρ and P, averaged over two convective turnover times. The shaded regions encompass the maximum and minimum values averaged over the same period.

$\dot{\epsilon}_{\rm nuc}$. At the base of the envelope, the mean value is $5.6 \times 10^{15}\,{\rm erg\,g^{-1}\,s^{-1}}$, but peak values of $2.4 \times 10^{16}\,{\rm erg\,g^{-1}\,s^{-1}}$ are reached. Thus, fluctuations in T of $\approx 40\%$ lead to fluctuations in the nuclear energy rate of $\approx 420\%$.

The nuclear energy generation rate grows steadily from $6 \times 10^{14}\,{\rm erg\,g^{-1}\,cm^{-1}}$ to $1 \times 10^{15}\,{\rm erg\,g^{-1}\,cm^{-1}}$, as ^{12}C is dredged up from the WD and powers the CNO cycle. The peak values are a little over one order of magnitude above the mean rates, due to the temperature fluctuations seen in Figure 5.2. Despite the steady growth of nuclear energy release, our numbers are not as high as those reported by the Glasner group, whose simulations yield rates that grow over *several orders of magnitude* in about the same simulated time.

Glasner et al. [2005] propose the definition for the 'success' of simulated nova outburst as "a TNR for which the amount of thermonuclear energy pumped into the envelope on a dynamic timescale is comparable to the binding energy of the envelope". In their paper, the gravitational binding energy of the envelope is $\sim 10^{46}$ erg. Glasner et al. decide that for their runs to be successful, a thermonuclear rate larger than $10^{44}\,{\rm erg\,s^{-1}}$ must be sustained for a dynamical time of $\sim 50\,{\rm s}$, which their simulations with the "correct" upper boundary conditions achieve [Glasner et al. 2005, Fig. 1].

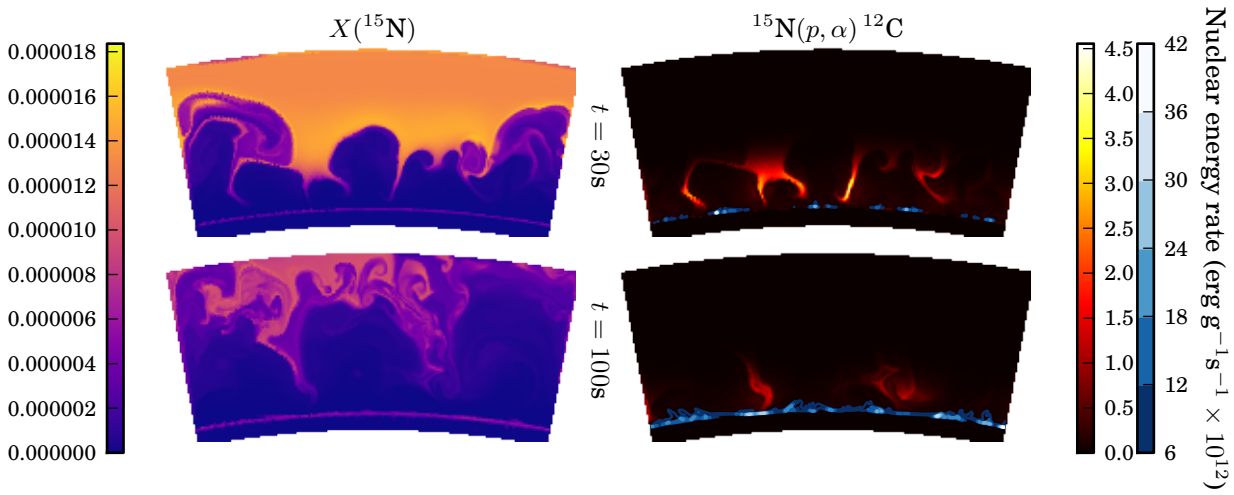

Figure 5.3.
Energy production from two key reactions. The heatmaps are ordered as follows: the **left column** shows the mass fraction of ^{15}N; the **right column** shows the energy generation rate from two reactions $^{15}\mathrm{N}(p,\alpha)^{12}\mathrm{C}$, and $^{12}\mathrm{C}(p,\gamma)^{13}\mathrm{C}$; the **top row** corresponds to $t = 30s$, the **bottom row** to $t = 100s$. (a) ^{15}N gets depleted in the first seconds of the simulations. At $t = 30$, when convection plumes rise to the higher layers of the envelope, the 'ashes' of this reaction are visible as dark swatches. Unburnt ^{15}N remains only in the uppermost strata. The energy rate is shown in (b). Observe the correlation of the morphology of the flames and the abundance of ^{15}N. In the same diagram, the energy release from $^{12}\mathrm{C}(p,\gamma)^{13}\mathrm{N}$ is also shown. While the energy from $^{15}\mathrm{N}(p,\alpha)$ is released up to about half the envelope height, the energy deposition from ^{12}C is very strongly localized at the base of the envelope. Panels (c) and (d) show the situation at much later times, when there is barely any ^{15}N in the envelope. Any remaining quantity that gets advected by descending convective plumes is instantly burnt.

Our envelope has a significantly lower binding energy. Due to the smaller mass of the white dwarf, $M_{\mathrm{WD}} = 1M_{\odot}$, the accreted mass is smaller. The energy GM_{env}^2/R is $\sim 4.5 \times 10^{18}$ erg. This energy is pumped into our envelope after about $t \sim 170\,\mathrm{s}$, see Figure 5.4. To the author it is unclear what Glasner et al. [2005] mean by a dynamical time, which they specify as 50 s. Employing the common definition of the ratio of typical length scale ΔR to sound speed, we have $\tau_{\mathrm{dyn}}^{(1)} \sim \Delta R/c_{\mathrm{s}} \approx 0.6\,\mathrm{s}$. The convective timescale is $\tau_{\mathrm{conv}} \sim \Delta R/v_{\mathrm{conv}} \approx 8\,\mathrm{s}$, which is still significantly smaller than the purported 50 s. However, we expect that the timescales in our envelope will be *longer*, because of the smaller pressure at the bottom of the envelope. Without a clear definition for the so-called dynamical time, it is difficult to assess the criterion of TNR success by Glasner et al. Nevertheless, at the end of the simulation, nuclear reactions in the envelope have produced just over 2.5 times its binding energy.

Let us inspect the individual reactions taking place in the CNO cycle.

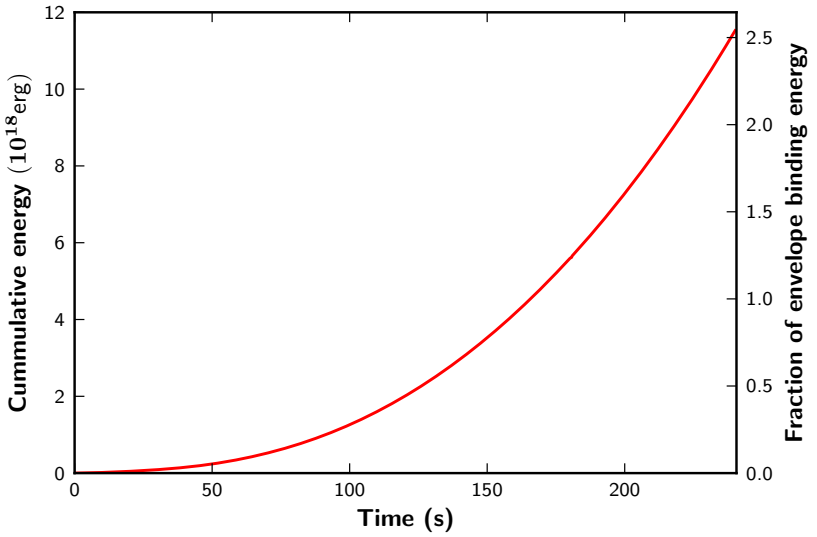

Figure 5.4.
Nuclear energy rate summed over the simulation time. At the end of the simulated time, over 2.5 times the envelope binding energy has been produced from nuclear reactions.

5.2. Nuclear reactions

The reaction network *YANN* calculates the total thermonuclear energy release by the change in abundance $\dot{Y}_i$ of all species i

$$\dot{\epsilon}_{\text{nuc}} = -\sum_i N_A M_i c^2 \dot{Y}_i. \tag{5.3}$$

Here, we are interested in the contribution of the *individual* reactions, and need a different expression. Let's first look at charged particle reactions. The energy release of a reaction between two partners i and j with Q-value $Q_{ij\to kl}$ is given by [Iliadis 2007]:

$$\epsilon_{ij\to kl} = \frac{Q_{ij\to kl}\, r_{ij\to kl}}{\rho} \tag{5.4}$$

$$= \frac{Q_{ij\to kl}}{\rho} \frac{N_i N_j \langle \sigma v \rangle_{ij\to kl}}{1+\delta_{ij}}, \tag{5.5}$$

where r, $< \sigma v >$ and N_i are defined by Equation (2.33). In the second step, the reaction rate r was inserted from Equations (2.33) and (2.34). The factor $1/(1+\delta_{ij})$, where δ_{ij} is the Kronecker delta, stands to take account for the interaction between identical partners. The numbers N_i are linked to the *nuclear abundance* and the *mass fraction* X_i by the relations

$$Y_i = \frac{N_i}{\rho N_A}, \qquad X_i = A_i Y_i, \qquad N_i = \rho N_A \frac{X_i}{A_i} \tag{5.6}$$

We rewrite the equation in terms of the mass fractions, because this is the quantity obtained from our hydro code, and drop the $ij \to kl$. The expression for the energy

release becomes

$$\epsilon = \frac{Q}{\rho}\,\rho^2 N_A^2\,\frac{X_0 X_1}{A_0 A_1}\,\frac{\langle\sigma\nu\rangle}{1+\delta_{ij}}. \tag{5.7}$$

For three interacting particles 012 in the input channel, Equation (5.5) gets an extra factor $\rho N_A X_2/A_2$. The expression for the energy generation rate then results in

$$\epsilon = Q\,\rho^{n-1} N_A\,\lambda\mathcal{N}\prod_{i=0}^{n-1}\frac{X_i}{A_i} \tag{5.8}$$

where n is the number of particles in the input channel. Here, λ is the *reduced reaction rate*:

$$\lambda = \begin{cases} N_A\langle\sigma v\rangle & \text{if } n=2 \\ N_A^2\langle\sigma v\rangle & \text{if } n=3. \end{cases} \tag{5.9}$$

This is the quantity tabulated in the *REACLIB* database [Cyburt et al. 2010]. Lastly, the multiplicity factor $\mathcal{N}$ accounts for identical particles [Fowler et al. 1967]:

$$\mathcal{N} = \begin{cases} (1+\delta_{01})^{-1} & \text{if } n=2 \\ (1+\Delta_{012})^{-1} = (1+\delta_{01}+\delta_{12}+\delta_{20}+2\,\delta_{012})^{-1} & \text{if } n=3. \end{cases} \tag{5.10}$$

In practice, the only trinary reaction included in our network is the triple-alpha reaction. All radiative proton captures and (α, p) reactions are binary reactions.

Figure 5.5 shows the radial profile of the nuclear energy release rate from all reactions in our network (rates above $10^4\,\mathrm{erg\,g^{-1}\,s^{-1}}$). Panel (a) shows the situation at the start of the simulation. Proton capture reactions are identifiable as the sloped curves; β^+-decays have approximately flat distributions. The reaction $^{15}\mathrm{N}(p,\alpha)^{12}\mathrm{C}$ is the primary source of energy at t_0. There are almost two orders of magnitude difference between its energy rate and that of the secondary reactions – the radiative proton captures on $^{12,13}\mathrm{C}$. This great difference explains the drop in energy already discussed in Figure 4.7 and visualized in Figure 5.3.

At the start, $^{13}\mathrm{C}(p,\gamma)$ produces more energy than $^{12}\mathrm{C}(p,\gamma)$ throughout the envelope, except at the very base, where the energy rate from the proton capture on $^{12}\mathrm{C}$ exhibits a peak. Three more proton capture reactions contribute significantly to the total energy rate: $^{14}\mathrm{N}(p,\gamma)$, $^{15}\mathrm{N}(p,\gamma)$ and $^{16}\mathrm{O}(p,\gamma)$. Their rates at the base of the envelope range between 3×10^{10} and $3\times10^{11}\,\mathrm{erg\,g^{-1}\,s^{-1}}$. There is a difference of two orders of magnitude between the rates from $^{12}\mathrm{C}(p,\gamma)$ and $^{16}\mathrm{O}(p,\gamma)$. The only trace of the HCNO cycle is from $^{13}\mathrm{N}(p,\gamma)$, which in this scale is visible only at the base of the envelope. Above $r_8 = 6.3$, the rates of all proton capture reactions has dropped below $10^4\,\mathrm{erg\,g^{-1}\,s^{-1}}$ and nuclear energy stems mainly from the positron decays.

The profiles at the last timestep of the simulation ($t = 240\,\mathrm{s}$) is shown in panel (b). $^{12}\mathrm{C}(p,\gamma)$ is the primary reaction, as expected, before $^{13}\mathrm{C}(p,\gamma)$. At this point, the energy rate from the 'hot' reaction $^{13}\mathrm{N}(p,\gamma)$ at the base of the envelope surpasses $2\times10^{11}\,\mathrm{erg\,g^{-1}\,s^{-1}}$ and has about the same profile as $^{14}\mathrm{N}(p,\gamma)$. In the simulated time, it has climbed almost 7 orders of magnitude. The profiles of both reactions on $^{15}\mathrm{N}$, (p,γ) and (p,α) show a very similar shape: they reach a maximum at $r_8 = 5.7$

and have a dip in below that radius as it nears the burning region, where ^{15}N is quickly burned, and a peak again at the burning layer. This particular shape of the profile must be due to a detailed balance between the rates at which ^{15}N is produced through $^{15}\mathrm{O}(\beta^+\nu)$ and destroyed by proton captures. All other profiles have rather smooth curves.

Figure 5.5 shows the evolution of the energy rates over time, averaged over the burning region (the lower third of the envelope). The rates from $^{15}\mathrm{N}(p,\alpha)$ show a very ragged curve due to the its strong fluctuations (see Figure 5.3). The rise of the rates from $^{13}\mathrm{N}(\beta^+,\nu)^{13}\mathrm{C}$ is interesting. While in the upper envelope, the β^+decays are always dominant, even in the burning region, the decay of ^{13}N becomes the third most important source of energy, owed to its extreme production by $^{12}\mathrm{C},(p,\gamma)$. Also, the proton capture on ^{13}N from the hot CNO cycle is seen to rise over several orders of magnitude. Despite the overall increasing rates, the principal reaction is more powerful than any other by two orders of magnitude.

Isotopic abundances

In our simulation box, the envelope takes up 90% of the height, the lower 10% corresponding to the white dwarf's surface layers. For the nucleosynthesis analysis, the envelope is divided in the radial direction into three equal parts. The bottom third includes some layers of the WD-envelope transition and the layers of peak energy generation. The next third is the middle of the envelope. The last third is excluded from the analysis due to its proximity to the upper boundary. When convective eddies already enriched in CNO isotopes reach the upper boundary, material with the initial solar composition is dredged down. This is due to the nature of our boundary conditions. The hydrogen-rich down-flow continuously sinks the metallic content in the upper envelope, leading to spurious fluctuations in the mass fractions.

In the two analyzed regions - labeled 'burning region' and 'envelope' - the mean mass fractions of all species were calculated for the entire length of the simulation. These values between species differ by many orders of magnitude, owed to the large difference in reactivity λ between the participating reactions. To better visualize their evolution in time, the abundances relative to the initial value at $t = 0$ are calculated, $\langle X_i/X_{i,0}\rangle$. The results are shown in Figure 5.6. The upper panels show the evolution of the mass fractions; the lower panels the relative quantities of temperature T, Mach number M, energy generation rate $\dot{\epsilon}_{\mathrm{nuc}}$ and metallicity Z are plotted, so that their correlations is made evident.

Consider Figure 5.6. Two abundances change dramatically right from the start of the simulation. The curve corresponding to ^{13}N rises so rapidly that it exits the frame. The radiative capture on ^{12}C is the most active reaction by many orders of magnitude, because of its high cross section at temperatures above $1\times10^8\,\mathrm{K}$. The sudden drop in $\dot{\epsilon}_{\mathrm{nuc}}$ already mentioned in Section 4.4 is also reflected in the curve of ^{15}N.

Recall from Section 2.2.3 that in matter burning via the CNO cycles, the total abundance of CNO elements does not change, only the relative mass fractions of their isotopes do. Therefore, any observed change of their abundances is due to external processes, in this case the convective dredge up. Small convective eddies develop from $t = 5\,\mathrm{s}$, but only around $t = 20\,\mathrm{s}$ do large structures of about half the envelope

height arise (Figure 5.1). This is echoed in the curve of the Mach number. Around this time, the curves of metallicity and $\dot{\epsilon}_{\rm nuc}$ follow suit. The parallel trend of these quantities and the sharp rise of $X(^{12}\mathrm{C})$ demonstrate the close relationship between convection and energy generation: after the consumption of $^{15}\mathrm{N}$, energy rates rise only because of new fuel coming from the white dwarf due to convection. During the first 120 s of the run, the mean temperature gradually falls. This is because the peak temperature at the burning region is decreasing, as shown in Figure 4.9. However, the temperature gradient in the envelope rises as heat is transferred to the upper layers. This is reflected in the T curve in panel (b). Consider again panel (a). The curves of $X(^{17}\mathrm{O})$ and $X(^{17}\mathrm{F})$ reveal a key process. The production of $^{17}\mathrm{F}$ in the cold CNO cycles is strongly suppressed due to the low cross section of the radiative captures $^{15}\mathrm{N}(p,\gamma)^{16}\mathrm{O}$ and $^{16}\mathrm{O}(p,\gamma)^{17}\mathrm{F}$ (Section 2.2.3). Therefore, its over-abundance in the burning region must be a signature of the reaction $^{14}\mathrm{O}(\alpha,p)^{17}\mathrm{F}$, that is, some amount of the burning is proceeding through the hot CNO cycle. This is also observed in the stark depletion of $^{14}\mathrm{O}$: the negative slope until $t \approx 20\,\mathrm{s}$ is due to its radioactive decay, with a half life of $\tau_{1/2} = 71\,\mathrm{s}$. After the initial 20 s, the negative gradient increases, a sign of its transmutation into $^{17}\mathrm{F}$. The decay slows down and its 'abundance rate' reverses due to $^{13}\mathrm{N}(p,\gamma)^{14}\mathrm{O}$, another sign of the hot CNO cycle's activity. The one element that is depleted almost monotonically is $^{15}\mathrm{O}$. It decays to $^{15}\mathrm{N}$ with a half life of $\tau_{1/2}$ (also evident from the figure, $X(^{15}\mathrm{O})/X_0(^{15}\mathrm{O}) \approx 0.5$ after 120 s) and its production is limited by the slowest reaction in the CN cycle. After its half life, almost exactly half its initial abundance is present, therefore the radiative capture on $^{14}\mathrm{N}$ would seem to be practically inactive at the present conditions. We will see in the next section that it contributes significantly to the energy generation. The under-production of $^{15}\mathrm{O}$ limits the abundance of $^{15}\mathrm{N}$, which in turn is easily consumed to $^{12}\mathrm{C}$, therefore limiting the energy rate of the entire cycle.

The same analysis was applied to some layers above the burning region, shown in panel (b) of Figure 5.6. This way, the delayed action of the convective eddies is more evident and helps discern the important reactions. Before $t_2 = 20\,\mathrm{s}$, only the decay of the radioactive nuclei is evident. The sharp curve of $^{13}\mathrm{N}$ is also visible, therefore even at the lower temperatures of the upper envelope, $^{12}\mathrm{C}$ captures protons efficiently. The sudden change in nuclear activity is more clearly appreciated. Also in the envelope, $^{15}\mathrm{N}$ is almost used up in a matter of $\approx 20\,\mathrm{s}$, after the heat of convection reaches $r =$. The hot CNO cycle is also more easily recognized in the curve of $^{14}\mathrm{O}$, where the sharp increase is due to $^{12}\mathrm{C}(p,\gamma)^{13}\mathrm{N}(p,\gamma)^{14}\mathrm{O}$. The energy release rate doubles from $t \approx 50\,\mathrm{s}$ in 70 s.

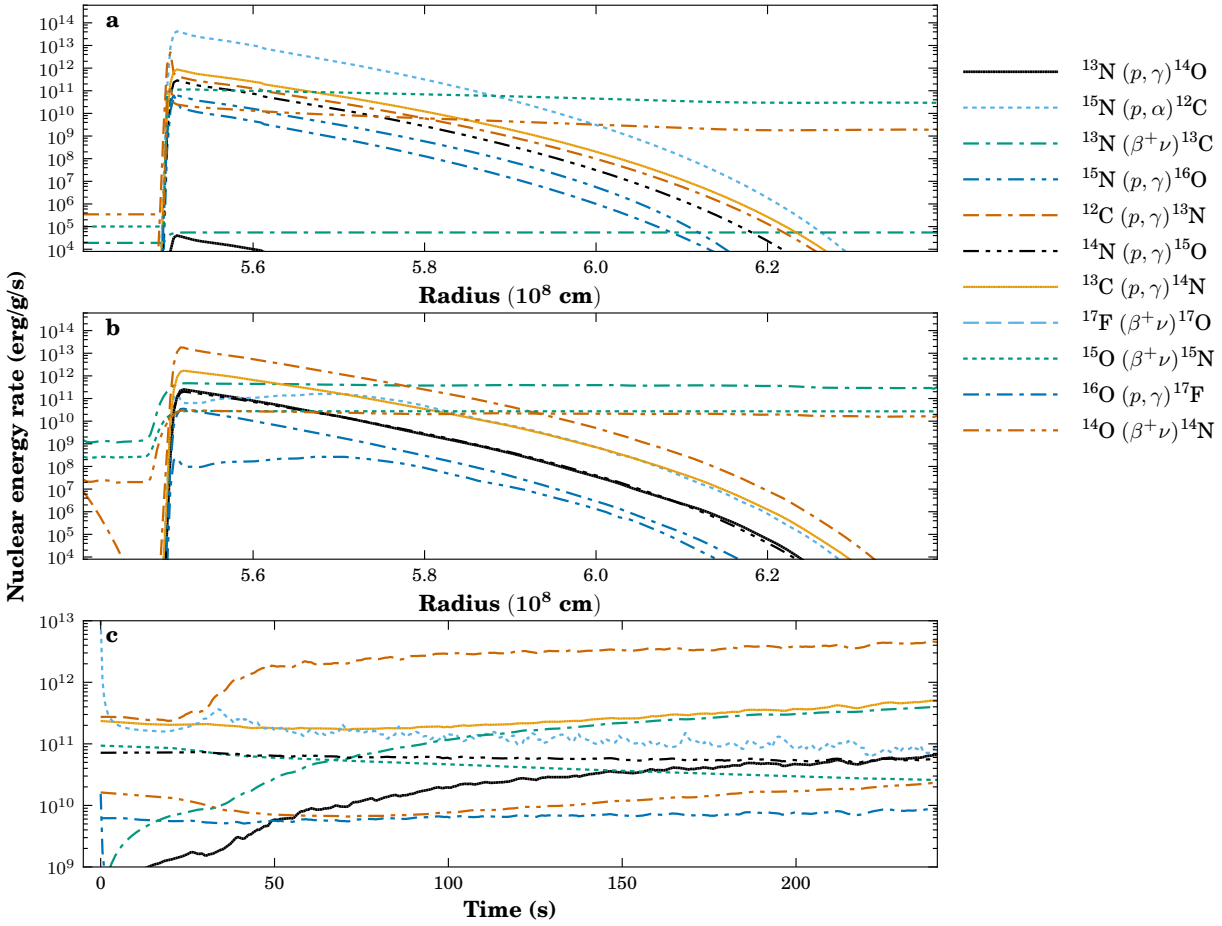

Figure 5.5.
Profiles of the nuclear energy rate at two times of the simulations, showing the contribution from each reaction. (*a*) At t_0, ^{15}N(p,α) yields the highest energy rate, larger by almost two orders of magnitude than all other proton capture reactions for most of the envelope's height. (*b*) In the envelope, the beta decay of ^{13}N becomes the most important source of energy. Except for the bottom region, where fusion takes places, most of the nuclear energy in the envelope stems from the beta decays. Due to the mixing from envelope matter into the core (which takes place substantially only after $t \approx 100$ s), proton captures on ^{12}C do happen. (*c*) Nuclear energy rates for each reaction in the nuclear network. At the start of the run (`Dp256`), the proton captures on ^{15}N generate most of the energy. In the envelope, most of the energy comes from the beta decay of ^{13}N.

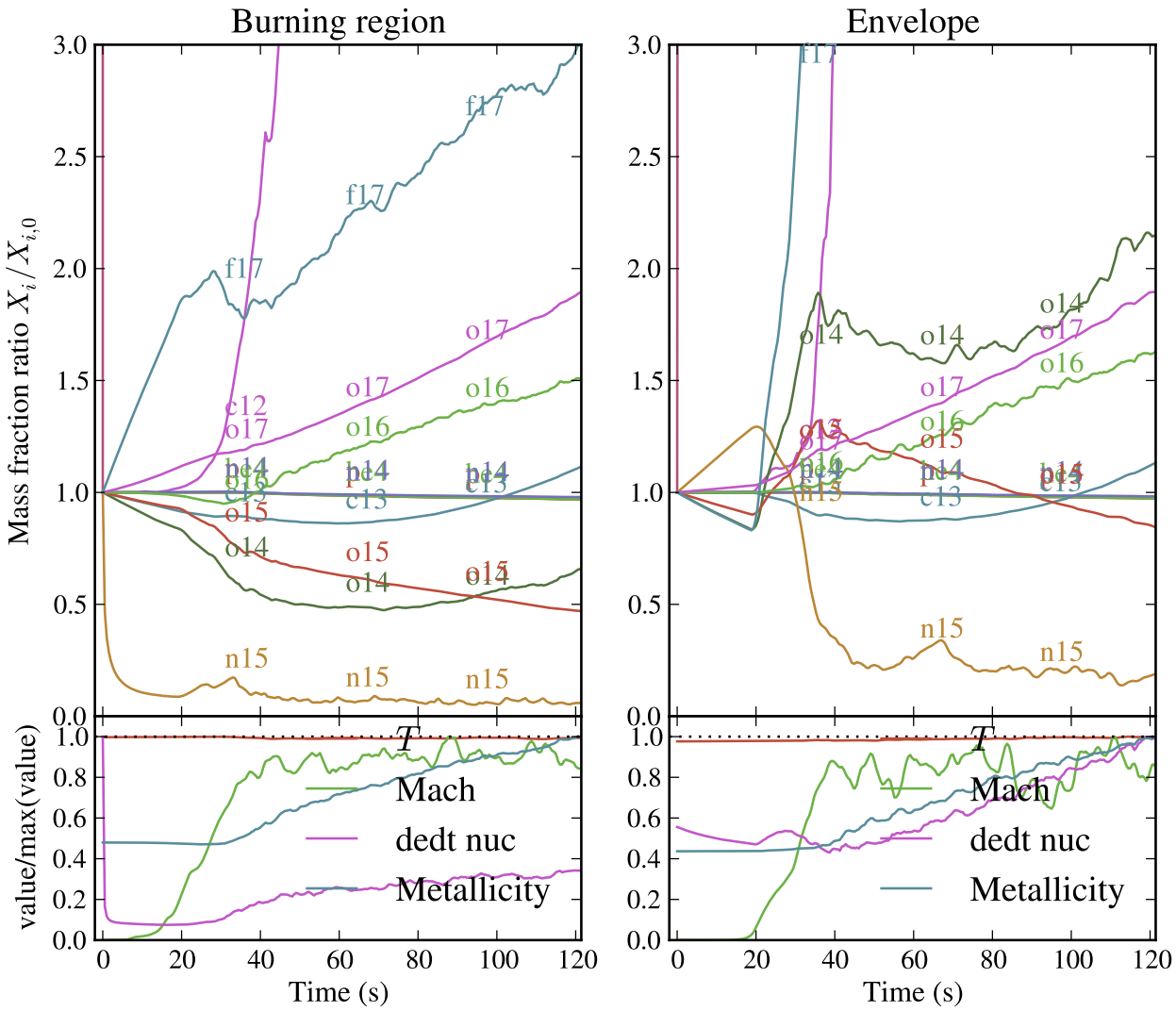

Figure 5.6.
Evolution of the mass fractions of the nuclear species in the run `Dp256`. The 'burning region' and 'envelope' (defined in the text) are analyzed separately. The effect of convection is more clearly appreciated in the envelope, because of its retardation by $\sim 20\,\mathrm{s}$.

To further demonstrate the role of convection, a comparison run with exactly the same initial conditions as Dp256 was performed, yet without the action of convection. This was achieved by switching off the hydro fluxes (Section 3.1.2). This way, any changes in the physical quantities originate from the nuclear reaction network - no fluid motions take place. The envelope evolves solely by burning the material available from the initial time step. This is clearly an unphysical setting, but it is interesting to contemplate, as it corresponds in a way to the situation in spherically symmetric solutions. There, the Ledoux criterion is fulfilled in a slab of the star's atmosphere, but no prescription for mixing with contiguous stable layers is accounted for. We ran the simulation only long enough to compare to the action of convection, which is more clearly appreciated after 30 s in the envelope of `Dp256`. Without hydro fluxes, the abundances progress almost linearly. Temperature rises due to the exothermic reactions, albeit at a very slow rate. Moreover, metallicity falls, as no fresh carbon or oxygen is dredged up from the WD and hydrogen get continuously transmuted into helium. The *number* fraction of CNO elements does not change, but the doubly larger mass of helium with respect to hydrogen increases their combined *mass* fraction. Lastly, the decline of Mach number is due not to hydrodynamical velocities, but to the changing sound speed. Most importantly, the rate of energy generation drops, because no additional fuel is supplied. *After only* 30 s*, it has lost 20% of its power.* Therefore, a TNR in classical nova envelopes can only arise from the continuous flux of CNO material. This simple test run shows the need for the proper treatment of mixing.

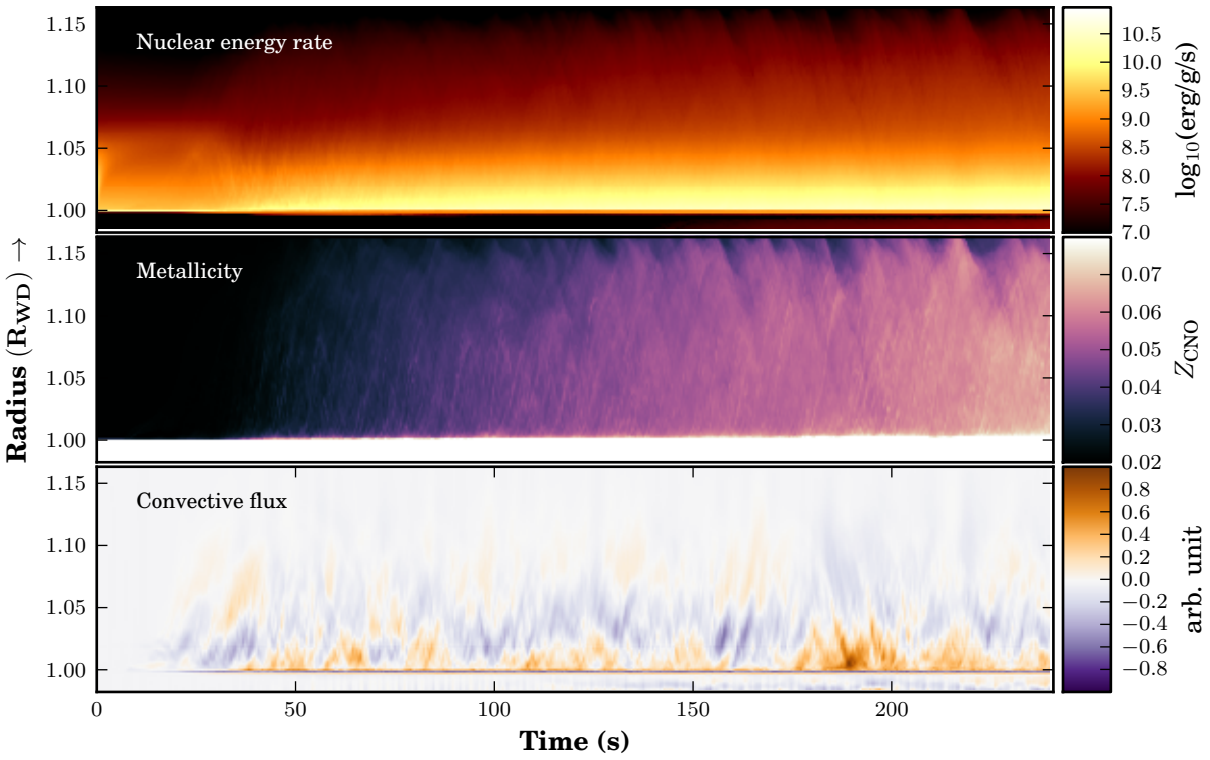

Figure 5.7.
A visual summary of the Dp256 run. The panels show the horizontal averages over time (the ordinate is the vertical coordinate in units of the WD radius), of the nuclear energy generation rate $\dot{\epsilon}_{\mathrm{nuc}}$, the metallicity Z_{CNO} and the convective flux F_{conv}. In the top panel, the sudden rise of plumes and subsequent 'vacuum' from the quick consumption of ^{15}N is seen as an arc in the first 30 s of the run. Afterward, the nuclear energy generation rate rises. The rise in metallicity is also clearly visible from $t = 50$ s onwards. The effect of the ghost cells with constant solar composition is visible also as inflows with darker values. The last panel shows the convective flux. Upward flux (*orange*) is strongest at the base of the envelope. A parallel fringe of downward flux (*purple*) hints at the size of the convective eddies. There is a clear separation between WD and envelope.

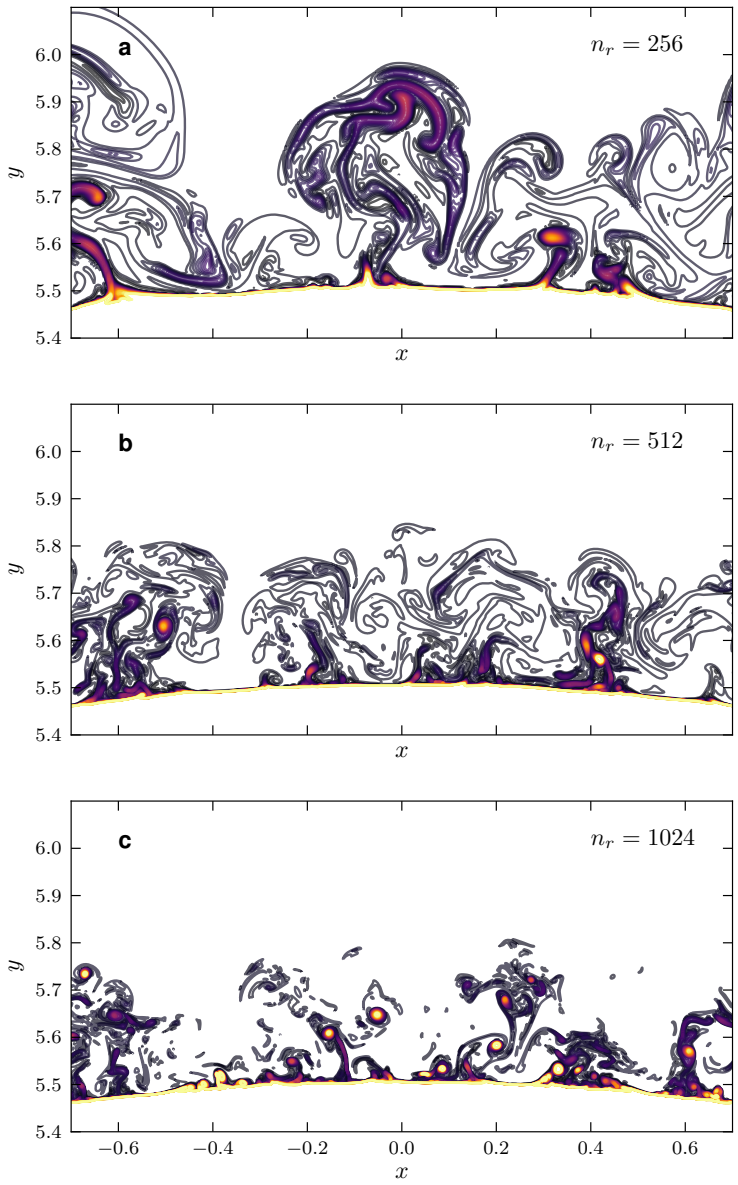

Figure 5.8.
Comparison of the simulations Dp256, Dp512 and Dp1024 at the time $t = 30\,\mathrm{s}$. The $^{12}\mathrm{C}$ mass fraction is shown with 50 contour lines in the range $[10^{-4}, 10^{-2}]$. In the simulations with finer resolution, the white dwarf material has reached lower layers. The high carbon concentrations are found mostly in fine filaments and dilute fast away from them. In Dp512 and most clearly in Dp2014 we observe the presence of high-concentration bubbles, forming already at the deepest layers of the envelope.

6. Conclusions & Outlook

> *The time will come when diligent research over long periods will bring to light things which now lie hidden. A single lifetime, even though entirely devoted to the sky, would not be enough for the investigation of so vast a subject... And so this knowledge will be unfolded only through long successive ages. There will come a time when our descendants will be amazed that we did not know things that are so plain to them... Many discoveries are reserved for ages still to come, when memory of us will have been effaced.*
> — Seneca, Natural Questions

A note on the interpretation of the simulations

The study of classical novae by means of direct numerical simulations (DNS) centers on the multi-dimensional simulation of the processes leading to the thermonuclear flash. One of the main aspects, pronounced several times in this work, is the mixing of CO matter into the envelope. However, there is a tacit assumption – and in a way, inconsistency – about the initial models commonly shared in the literature, and that is the solar-like composition of the accreted envelope. All published multi-D calculations start a few hundred seconds from the time of expected outburst, with a clear, unmixed envelope of pure solar composition at a temperature of $T_{\rm ss} \geq 10^8\,\mathrm{K}$. However, we know from 1D stellar evolution calculations, that convection starts, for WD masses of $\approx 1 M_\odot$, at about $T_{\rm ss} = 2 \times 10^7\,\mathrm{K}$. In the time elapsed between start of convection and outburst, the abundance of carbon and oxygen in the envelope should be rather higher than solar. The underlying assumption is that, if the enrichment achieved in the few $\times\, 10^2\,\mathrm{s}$ of simulated time is enough to fuel the TNR, then surely the convection acting for many years prior to the TNR ignition will also be sufficient.

Most of the published multi-D simulations are based on the model by Glasner et al. [1997] (see Section 1.2.2 and Section 4.1) . *All* models start from 1D stellar evolution simulations *without a prescription for mixing*. The core-envelope transition in such calculations is then rather sharp, as in our own models. In reality, the transition should be smooth, especially in view of the long period of cross-boundary mixing prior to the outburst. A stellar model built thusly would have super-solar abundances in the envelope at the TNR threshold, before the map to multi-D, consequently enabling a faster nova. Indeed, Denissenkov et al. [2013b] show that allowing for mixing in their *MESA* simulations allows for a much earlier outburst.

A second possible flaw in current models is the assumption of a bare CO white dwarf. When formed, white dwarfs retain on their surface a thin helium layer, a residue of the AGB phase. This layer, if stable against convection, represents a barrier between the CO fuel and the burning H-rich layer, inhibiting combustion via the CNO cycle. The search for new initial models that take into account mixing, a He-layer and the 'fluff' cells suggested by Zingale et al. [2002] was performed in a parallel work by Lach [2016].

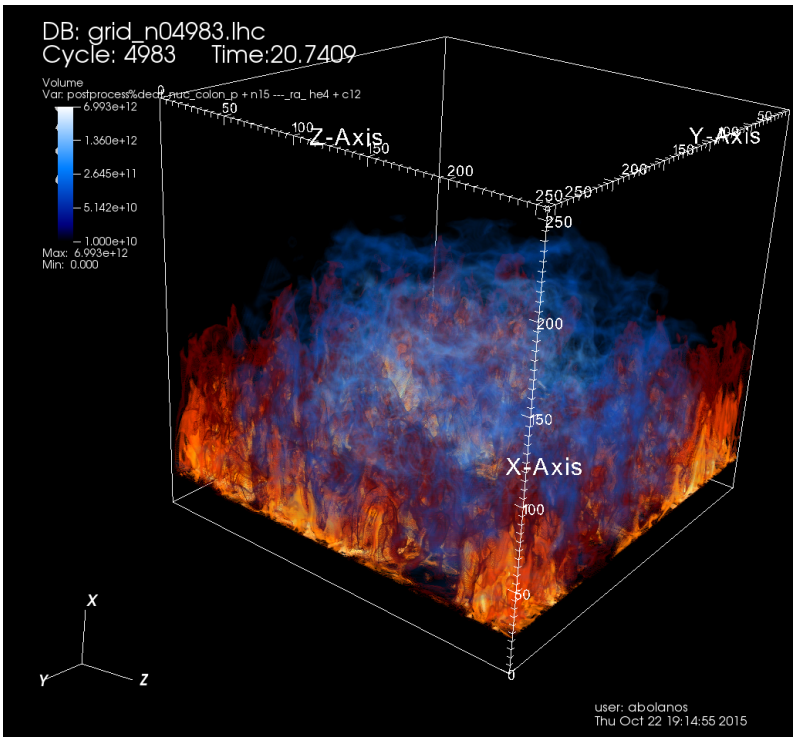

Figure 6.1.
Snapshot of a three-dimensional simulation with the `echo` setup. Color-coded in warm hues is the energy generation rate from the $^{12}\mathrm{C}(p,\gamma)$ reaction, and in cold hues the rate from $^{15}\mathrm{N}(p,\alpha)$. In this representation, the carbon burning flames resemble those of earthly fire, bound to the bottom of the envelope. The combustion of $^{15}\mathrm{N}$ takes place in an expanded cloud above.

Summary & Future work

Despite the mentioned caveats, we have shown that our code is capable of simulating the convective burning in classical nova envelopes. We have found that the stiffness of the convective boundary is very high, and consequently the permeability of the WD surface to impinging convective eddies very low. Extrapolating to longer time scales than those we simulated, the metallicity in the envelope reaches eventually the commonly cited value of $Z = 0.1$ (see Figure A.3 in the Appendix). However, the dredge-up efficiency depends very strongly on the resolution.

To understand the rate at which nuclear energy is released, we analyzed in detail the evolution of the physical values at the core-envelope interface. We found that generally the layer of peak nuclear energy generation rate does not coincide with that of the peak temperature, but lies a few layers deeper, where the density is higher. This has also consequences when building the initial numerical mesh for the simulation. Furthermore, we found that at the temperatures attained in our calculations, the energy is mostly generated by nuclear reactions in the cold CN cycle, specifically by proton captures on $^{12}\mathrm{C}$ and $^{13}\mathrm{C}$. There is almost no contribution form the hot CNO cycle, possibly because the envelope in the simulation is in fact not degenerate, in contrast to what is commonly described in the literature.

We performed some 3D simulations as well, in a 'box' of $800 \times 800 \times 1000$ km^3 in

spherical coordinates (see Figure 6.1). These lasted only around 30 s, due to unresolved issues at the boundaries. Here, all four lateral faces have the *wall* boundary condition (Section 3.1.4). The convective plumes, seen in 2D in Figure 5.1, reach the upper boundary very fast. In our 3D simulations, the plumes arise prominently at the four corners of the box, where the bottom of the envelope touches the box walls. They then flow fast, simultaneously, upward along the four vertical edges until reaching the top face and converging in its center. In the cells where of the four 'columns' collide, the Mach numbers can reach supersonic values. This behavior is clearly an artifact, and the simulations break down shortly afterward. This is a glitch that still needs to be resolved. Ultimately, the goal of future simulations will be to simulate the convective burning with the full effects of turbulence in three dimensions.

A. Additional figures

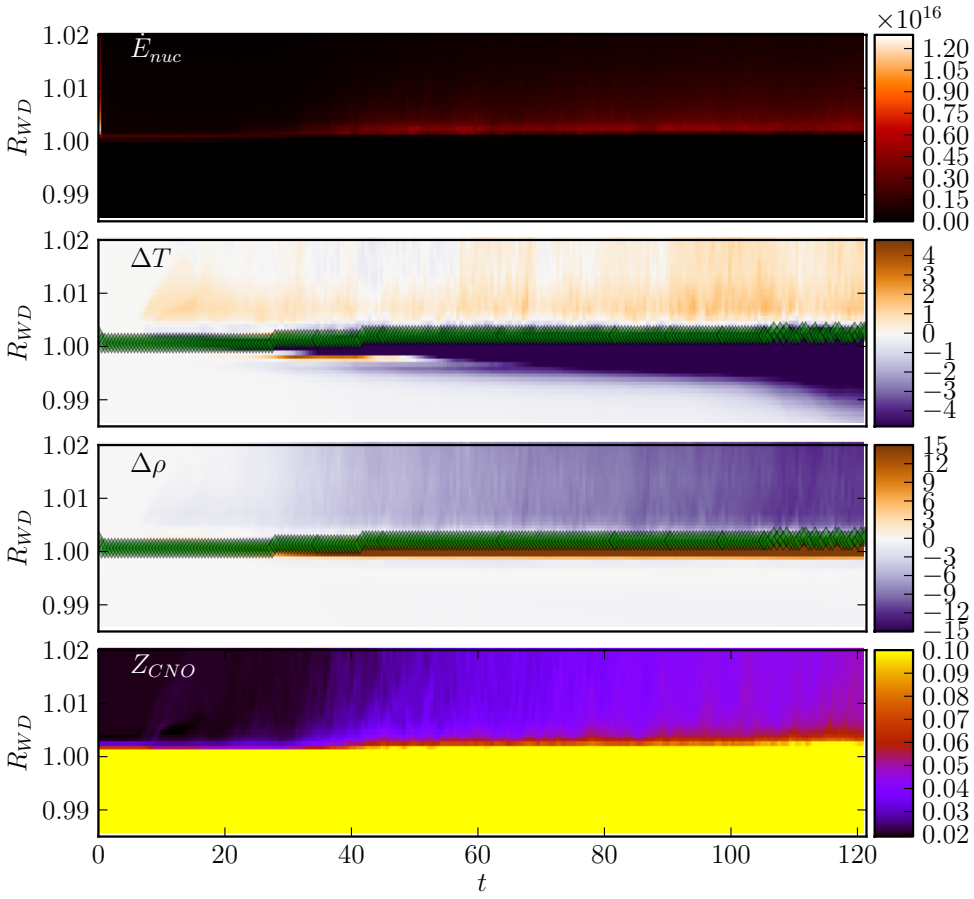

Figure A.1.
The evolution of four key quantities at the core-envelope interface for a nova simulation with $n_r = 256$. For the temperature and density, the difference from the initial condition is plotted: $\Delta T = T(t)/(T_0) - 1$ and $\Delta\rho = \rho(t)/(\rho_0) - 1$. peak of nuclear energy generation lies at lower temperatures throughout the length simulation.

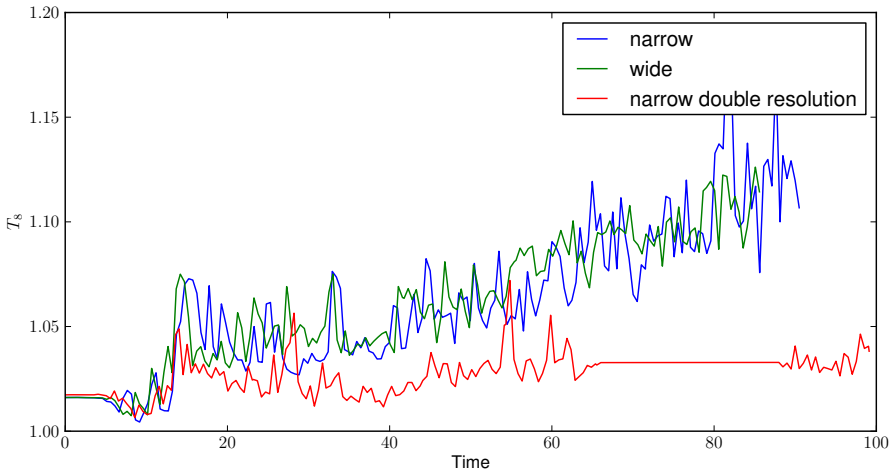

Figure A.2.
The time evolution of temperature in a simulation with twice as wide extension doesn't reveal any significant difference. The straight line of the red curve is due only to lost data.

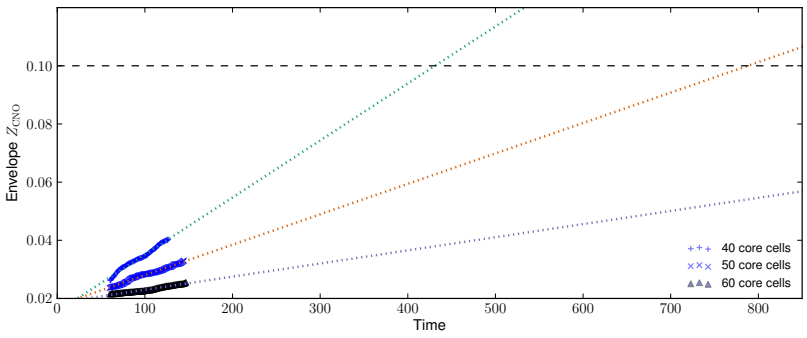

Figure A.3.
Fits to the metallicity curves in the `echo` simulations, assuming their evolution continues approximately linearly.

Bibliography

Anders, E. & Grevesse, N. 1989, Geochim. Cosmochim. Acta, 53, 197 59

Anupama, G. C. 2008, in Astronomical Society of the Pacific Conference Series, Vol. 401, RS Ophiuchi (2006) and the Recurrent Nova Phenomenon, ed. A. Evans, M. F. Bode, T. J. O'Brien, & M. J. Darnley, 31 4

Bader, G. & Deuflhard, P. 1983, Numerische Mathematik, 41, 373 33

Bethe, H. A. 1939, Physical Review, 55, 434 26

Bethe, H. A. & Critchfield, C. L. 1938, Physical Review, 54, 248 25

Bode, M. F. 2011, ArXiv e-prints, [1111.4941] 4, 5

Böhm-Vitense, E. 1958, ZAp, 46, 108 23

Cargo, P. & Le Roux, A. 1994, Comptes rendus de l'Académie des sciences. Série 1, Mathématique, 318, 73 53

Carroll, B. W. & Ostlie, D. A. 2007, An Introduction to Modern Astrophysics (Reading, MA: Addison-Wesley) 29

Casanova, J., José, J., García-Berro, E., Shore, S. N., & Calder, A. C. 2011, Nature, 478, 490 14, 15, 16, 68, 85

Chandrasekhar, S. 1961, Hydrodynamic and Hydromagnetic Stability (Oxford: Clarendon Press) 11, 64

Clayton, D. D. & Hoyle, F. 1974, ApJ, 187, L101 5

Coc, A., Hernanz, M., José, J., & Thibaud, J.-P. 2000, A&A, 357, 561, [astro-ph/0003166] 5

Courant, R., Friedrichs, K. O., & Lewy, H. 1928, Math. Ann., 100, 32 42

Cyburt, R. H., Amthor, A. M., Ferguson, R., et al. 2010, ApJS, 189, 240 93

della Valle, M. & Livio, M. 1995, ApJ, 452, 704 2

Denissenkov, P., Herwig, F., Pignatari, M., & Truran, J. 2013a, ArXiv e-prints, [1304.0414] 16

Denissenkov, P. A., Herwig, F., Bildsten, L., & Paxton, B. 2013b, ApJ, 762, 8, [1210.5209] 14, 16, 25, 101

Duerbeck, H. W. 2008, Cambridge Astrophysics Series, Vol. 43, Classical Novae, 2nd edn. (Cambridge: Cambridge University Press) 9

Edelmann, P. 2014, Dissertation, Technische Universität München 15, 33, 35, 36, 52, 55

Fields, B. D. 2011, Annual Review of Nuclear and Particle Science, 61, 47, [1203.3551] 5

Fowler, W. A., Caughlan, G. R., & Zimmerman, B. A. 1967, ARA&A, 5, 525 93

Freytag, B., Ludwig, H.-G., & Steffen, M. 1996, A&A, 313, 497 25, 75, 77

Fryxell, B. A., Müller, E., & Arnett, W. D. 1989, Hydrodynamics and nuclear burning, MPA Green Report 449, Max-Planck-Institut für Astrophysik, Garching 12, 58

Fryxell, B. A. & Woosley, S. E. 1982, ApJ, 261, 332 9, 12

Fujimoto, M. Y. 1982, ApJ, 257, 752 10

Gehrz, R. D. 2008, Cambridge Astrophysics Series, Vol. 43, Classical Novae, 2nd edn. (Cambridge: Cambridge University Press) 5

Gehrz, R. D., Truran, J. W., Williams, R. E., & Starrfield, S. 1998, PASP, 110, 3 2, 7

Gil-Pons, P., García-Berro, E., José, J., Hernanz, M., & Truran, J. W. 2003, A&A, 407, 1021, [astro-ph/0306197] 5

Glasner, S. A. & Livne, E. 1995, ApJ, 445, L149 10, 14, 16

Glasner, S. A., Livne, E., & Truran, J. W. 1997, ApJ, 475, 754 11, 12, 13, 16, 58, 59, 65, 80, 87, 101

Glasner, S. A., Livne, E., & Truran, J. W. 2005, ApJ, 625, 347, [astro-ph/0504054] 13, 16, 58, 70, 90, 91

Glasner, S. A., Livne, E., & Truran, J. W. 2007, ApJ, 665, 1321 11, 16, 70, 82

Glasner, S. A., Livne, E., & Truran, J. W. 2012, MNRAS, 427, 2411 16, 70

Glasner, S. A. & Truran, J. W. 2009, ApJ, 692, L58, [0812.3984] 16

Glasner, S. A. & Truran, J. W. 2012, Journal of Physics Conference Series, 337, 012071, [1107.1567] 4

Guillard, H. & Viozat, C. 1999, Computers & Fluids, 28, 63 47, 48

Hernanz, M., José, J., Coc, A., Gómez-Gomar, J., & Isern, J. 1999, ApJ, 526, L97, [astro-ph/9910111] 5

Herwig, F. 2000, A&A, 360, 952, [astro-ph/0007139] 25

Herwig, F., Bloecker, T., Schoenberner, D., & El Eid, M. 1997, A&A, 324, L81, [astro-ph/9706122] 25

Herwig, F., Freytag, B., Hueckstaedt, R. M., & Timmes, F. X. 2006, ApJ, 642, 1057, [astro-ph/0601164] 25, 77

Hix, W. R. & Meyer, B. S. 2006, Nuclear Physics A, 777, 188, [arXiv:astro-ph/0509698] 27

Hosea, M. & Shampine, L. 1996, Applied Numerical Mathematics, 20, 21 , method of Lines for Time-Dependent Problems 44

Iliadis, C. 2007, Nuclear Physics of Stars, 1st edn. (Weinheim: WILEY-VCH Verlag GmbH) 92

Iliadis, C. 2010, in American Institute of Physics Conference Series, Vol. 1213, American Institute of Physics Conference Series, ed. C. Spitaleri, C. Rolfs, & R. G. Pizzone, 3–22, [0911.3965] 25, 26

Izzo, L., Valle, M. D., Mason, E., et al. 2015, The Astrophysical Journal Letters, 808, L14 5

José, J. & Hernanz, M. 1998, ApJ, 494, 680, [astro-ph/9709153] 2, 5, 6, 7, 14

José, J., Hernanz, M., & Iliadis, C. 2006, Nuclear Physics A, 777, 550 4, 5, 16

José, J. & Iliadis, C. 2011, Reports on Progress in Physics, 74, 096901, [1107.2234] 2, 4

José, J. & Shore, S. N. 2008, Cambridge Astrophysics Series, Vol. 43, Classical Novae, 2nd edn. (Cambridge: Cambridge University Press) 4

Kahabka, P., Hartmann, H. W., Parmar, A. N., & Negueruela, I. 1999, A&A, 347, L43 2

Kato, M. & Hachisu, I. 1994, ApJ, 437, 802 7

Kennedy, C. A. & Carpenter, M. H. 2001, Additive Runge-Kutta Schemes for Convection-Diffusion-Reaction Equations, Tech. rep., NASA Technical Memorandum 44

Kercek, A., Hillebrandt, W., & Truran, J. W. 1998, A&A, 337, 379, [astro-ph/9801054] 12, 13, 16, 57, 58, 59, 65, 72, 79, 80, 82, 87

Kercek, A., Hillebrandt, W., & Truran, J. W. 1999, A&A, 345, 831, [astro-ph/9811259] 13, 15, 16, 17, 58, 79, 80, 81, 82

Kippenhahn, R., Weigert, A., & Hofmeister, E. 1967, Methods in Computational Physics, 7, 129 19

Kippenhahn, R., Weigert, A., & Weiss, A. 2013, Stellar Structure and Evolution (Springer) 5, 19, 21, 23, 36, 52

Kirchhoff, G. 1860, Annalen der Physik, 185, 275 25

Krauss, L. M. & Chaboyer, B. 2003, Science, 299, 65 20

Krueger, B. K. 2012, PhD thesis, Stony Brook University 15, 63, 68, 71

Lach, F. 2016, Master's thesis, Universität Würzburg, Germany 79, 101

LeVeque, R. J. 2002, Finite volume methods for hyperbolic problems, Vol. 31 (Cambridge university press) 46

Liou, M.-S. 1996, Journal of Computational Physics, 129, 364 51

Liou, M.-S. 2006, Journal of Computational Physics, 214, 137 51

Liou, M.-S. & Steffen, C. J. J. 1993, Journal of Computational Physics, 107, 23 51

Liska, R. & Wendroff, B. 2003, SIAM Journal on Scientific Computing, 25, 995 50

Livio, M., Shankar, A., Burkert, A., & Truran, J. W. 1990, ApJ, 356, 250 7

Livio, M. & Truran, J. W. 1994, ApJ, 425, 797 5, 7

Livne, E. 1993, ApJ, 412, 634 10

Lodders, K. 2003, ApJ, 591, 1220 59

Meakin, C. A. & Arnett, D. 2006, ApJ, 637, L53, [astro-ph/0601348] 75

Meakin, C. A. & Arnett, D. 2007, ApJ, 667, 448, [arXiv:astro-ph/0611315] 77, 78

Miczek, F. 2013, Dissertation, Technische Universität München 15, 35, 44, 46, 49, 50, 52

Miczek, F., Röpke, F. K., & Edelmann, P. V. F. 2015, A&A, 576, A50, [1409.8289] 15, 35, 48, 50

Montesinos, B., Thomas, J. H., Ventura, P., & Mazzitelli, I. 2001, MNRAS, 326, 877 8

Moore, K. & Bildsten, L. 2012, ApJ, 761, 182, [1210.7546] 5

Newton, I. 1726, Philosophiae Naturalis Principia Mathematica, ed. A. Koyrè & J. B. Cohen (Cambridge: Harvard University Press) 1

Newton, I. 1729, The Mathematical Principles of Natural Philosophy, ed. A. Motte (London: B. Motte) 1

Osborne, J. P., Page, K. L., Beardmore, A. P., et al. 2011, ApJ, 727, 124, [1011.5327] 2, 5

Pakmor, R., Kromer, M., Taubenberger, S., et al. 2012, ApJ, 747, L10, [1201.5123] 33

Paxton, B., Bildsten, L., Dotter, A., et al. 2011, ApJS, 192, 3, [1009.1622] 17, 78

Paxton, B., Cantiello, M., Arras, P., et al. 2013, ArXiv e-prints, [1301.0319] 17, 25, 78

Plinius, C. 1855, The Natural History of Pliny, ed. J. Bostock & H. T. Riley (London: H.G. Bohn) 1

Prandtl, L. 1925, Z. angew. Math. Mech., 5, 136–139 23

Riccioli, G. B. 1652, Almagestum novum astronomiam veterem novamque complectens observationibus aliorum et propriis novisque theorematibus, problematibus ac tabulis promotam, Bd. I-III, Bologna 1651; (Bologna: ex typographia haeredis Victorii Benatii) 1

Roe, P. 1981, Journal of Computational Physics, 43, 357 41

Schaefer, B. E. 2010, ApJS, 187, 275, [0912.4426] 4

Shafter, A. W. 1997, ApJ, 487, 226 4

Shankar, A. & Arnett, D. 1994, ApJ, 433, 216 10

Shankar, A., Arnett, D., & Fryxell, B. A. 1992, ApJ, 394, L13 10

Shara, M. M. 1982, ApJ, 261, 649 9

Shara, M. M., Zurek, D. R., Williams, R. E., et al. 1997, AJ, 114, 258 3

Shen, K. J. & Bildsten, L. 2009, ApJ, 692, 324, [0805.2160] 5, 10

Shu, C.-W. & Osher, S. 1988, Journal of Computational Physics, 77, 439 42

Starrfield, S. 2001, in Astronomical Society of the Pacific Conference Series, Vol. 231, Tetons 4: Galactic Structure, Stars and the Interstellar Medium, ed. C. E. Woodward, M. D. Bicay, & J. M. Shull, 466 7

Starrfield, S., Iliadis, C., & Hix, W. R. 2008, Cambridge Astrophysics Series, Vol. 43, Classical Novae, 2nd edn. (Cambridge: Cambridge University Press) 7

Starrfield, S., Iliadis, C., Hix, W. R., Timmes, F. X., & Sparks, W. M. 2007, in American Institute of Physics Conference Series, Vol. 891, Tours Symposium on Nuclear Physics VI, ed. M. Arnould, M. Lewitowicz, H. Emling, H. Akimune, M. Ohta, H. Utsunomiya, T. Wada, & T. Yamagata, 364–372, [0706.0558] 29

Starrfield, S., Iliadis, C., Hix, W. R., Timmes, F. X., & Sparks, W. M. 2009, ApJ, 692, 1532, [0811.0197] 2, 4, 29

Starrfield, S., Sparks, W. M., & Truran, J. W. 1985, ApJ, 291, 136 11

Starrfield, S., Truran, J. W., Sparks, W. M., & Arnould, M. 1978, ApJ, 222, 600 5

Starrfield, S., Truran, J. W., Sparks, W. M., & Kutter, G. S. 1972, ApJ, 176, 169 7, 9

Starrfield, S., Truran, J. W., Wiescher, M. C., & Sparks, W. M. 1998, MNRAS, 296, 502 15

Timmes, F. X. & Arnett, D. 1999, ApJS, 125, 277 38

Timmes, F. X. & Swesty, F. D. 2000, ApJS, 126, 501 39

Toro, E. F. 2009, Riemann Solvers and Numerical Methods for Fluid Dynamics: A Practical Introduction (Springer) 36, 40, 41

Townsley, D. M. & Bildsten, L. 2004, ApJ, 600, 390, [arXiv:astro-ph/0306080] 15

Turkel, E. 1999, Annual Review of Fluid Mechanics, 31, 385 49

Von Weizsäcker, C. F. 1938, Physikalische Zeitschrift, 39, 633 26

Warner, B. 2008, Cambridge Astrophysics Series, Vol. 43, Classical Novae, 2nd edn. (Cambridge: Cambridge University Press) 4

Weaver, T. A., Zimmerman, G. B., & Woosley, S. E. 1978, ApJ, 225, 1021 70

Werner, K. & Herwig, F. 2006, PASP, 118, 183, [astro-ph/0512320] 25

Wiescher, M., Gorres, J., Thielemann, F.-K., & Ritter, H. 1986, A&A, 160, 56 7

Wiescher, M., Görres, J., Uberseder, E., Imbriani, G., & Pignatari, M. 2010, Annual Review of Nuclear and Particle Science, 60, 381 5, 6, 19, 28, 29, 30

Wolf, W. M., Bildsten, L., Brooks, J., & Paxton, B. 2013, ApJ, 777, 136, [1309.3375] 6, 12, 14, 16

Xu, Z., Pankenier, W., & Jiang, Y. 2000, East-Asian Archaeoastronomy: Historical Records of Astronomical Observations of China, Japan, and Korea (CRC Press) 1

Zingale, M., Dursi, L. J., ZuHone, J., et al. 2002, ApJS, 143, 539, [astro-ph/0208031] 68, 70, 71, 72, 101